



Norwegian University of
Science and Technology

Assessment of an existing bridge suffering from Alkali-Silica reaction

Eirik Olov Myklebust

Civil and Environmental Engineering

Submission date: June 2018

Supervisor: Daniel Cantero, KT

Co-supervisor: Håvard Johansen, Vegdirektoratet/ bruseksjon
Hans Stemland, SINTEF/ NTNU

Norwegian University of Science and Technology
Department of Structural Engineering



MASTER THESIS 2018

SUBJECT AREA: Concrete Structures	DATE: June 11 th 2018	NO. OF PAGES: 184
--------------------------------------	-------------------------------------	----------------------

TITLE:

Assessment of an existing bridge suffering from Alkali-Silica reaction

Vurdering av en eksisterende bro skadelidende av Alkali-Silikareaksjoner

BY:

Eirik Myklebust



SUMMARY:

The first parts of the thesis contain a general literature review about damage mechanisms in concrete and how they affect the structural behavior of concrete structures. The survey is extended with a more in-depth review of damage due to alkali-silica reactions. One of the effects of alkali-silica reactions is the formation of a swelling gel, which in contact with water expands. In statically undetermined bridges, elongation and curvature changes from alkali- expansion could result in additional moments in which these type of bridges not were designed for. Elgeseter bridge in Trondheim is one of those bridges.

Structural assessment of Elgeseter bridge was conducted in the longitudinal direction. The capacity control of the different sections was conducted, not taking into account structural damages or concrete degradation. When including loads due to alkali-silica expansion, the moment capacities were exceeded in the field section between axis 1-2 (15%), the internal field sections (27%) and in the original zero moment sections, 4.5m from the columns (92%).

A more in-depth study was conducted regarding alkali-silica expansion on Elgeseter bridge, making a 2D model (longitudinal direction) and a 3D model of the bridge in the finite element program DIANA. Both models revealed large tensile stresses in the original zero moment sections due to additional moment from the alkali reaction. The crack development on the bridge found by the 2D model seemed to be in good correlation with the field investigations on the bridge which has revealed large cracks occurring at the zero moment spots. With the 3D model, it was also possible to detect shear stresses appearing on the plate due to different strain over the width of the cross-section at the end span.

RESPONSIBLE TEACHER: Associate Professor Daniel Cantero

SUPERVISOR(S): Daniel Carrero, NTNU, Håvard Johansen, Statens Vegvesen, and Hans Stemland, Sintef

CARRIED OUT AT: Department of Structural Engineering, NTNU Trondheim

Preface

This master's thesis is the final part of a 5-year master's degree in Civil and Environmental Engineering at The Norwegian University of Science and Technology. The thesis is produced over 20 weeks during the spring of 2018.

Daniel Cantero has been my supervisor at NTNU. Håvard Johansen in Satens vegvesen and Hans Stemland in Sintef have been my co-supervisors.

Through the work I have put into this thesis, I have gained valuable insight in the process of establishing design loads and performing capacity calculations on existing concrete bridges. Valuable insight have also been gained regarding different damage mechanisms and how they affect the structural behaviour of concrete structures.

I would like to thank my supervisor and co-supervisors for valuable guidance throughout this semester. Furthermore, I am grateful for valuable discussions and advice from my fellow students at NTNU.

Trondheim, June 11th 2018

Eirik Myklebust

Abstract

The first parts of the thesis contain a general literature review about damage mechanisms in concrete and how they affect the structural behavior, extended with a more in-depth review of damage due to alkali-silica reactions (ASR). One of the effects of alkali-silica reactions is the formation of a swelling gel, which in contact with water expands. This could lead to severe elongation of a bridge. As the reaction increase on increasing water saturation, some part of the cross-section could achieve more expansion load from the chemical reaction. This could result in curvature changes over a bridge cross-section. In statically undetermined bridges, elongation and curvature changes from alkali-expansion could result in additional moments in which these type of bridges not were designed for.

Elgeseter bridge in Trondheim is one of the bridges suffering from this degradation mechanism. Field investigations on the bridge have revealed large vertical cracks occurring at many of the original zero moment sections, 4.5m from the columns at the inner beams. A number of small cracks occurring in the field sections are also reported. These cracks are assumed to appear due to additional moments on the bridge from alkali-silica expansion, and the assumption that the outer beams are expanding more than the inner beams, straining the inner beams. A limited amount of reinforcement in the original zero moment sections is assumed to be the reason why the most significant cracks appear in these sections.

As part of the thesis, structural assessment in the longitudinal direction of Elgeseter bridge was conducted, using the original bridge drawings and NS3473 2003, which forms the basis of assessing existing concrete structures. The capacity control of the different sections was conducted, not taking into account structural damages or concrete degradation. Shear and moment capacities were on the safe side when neglecting additional loads due to alkali-expansion. When taking additional ASR loads into account, the moment capacities were exceeded in the field section between axis 1-2 (15%), the internal field sections (27%) and in the original zero moment sections, 4.5m from the columns (92%).

A more in-depth study was conducted regarding alkali-silica expansion on Elgeseter bridge, making a 2D model (longitudinal direction) and a 3D model of the bridge in the finite element program DIANA. Adding thermal load was used as the solution strategy to simulate ASR expansion on the bridge models (coefficient of thermal expansion in the reinforcement was set to zero). Both models revealed large tensile stresses in the original zero moment sections. The crack development on the bridge found by the 2D model seemed to be in good correlation with the field investigations on the bridge. With the 3D model, it was also possible to detect shear stresses appearing on the plate due to different strain over the width of the cross-section at the end span.

Sammendrag

Denne masteroppgaven omhandler skader på betongkonstruksjoner, utvidet med en dypere studie av skader på grunn av alkali-silika reaksjoner (ASR). En av virkningene av alkalireaksjoner er dannelse av en svellende gel, som i kontakt med vann kan utvide seg og ekspandere betongen. Dette kan gi store lengdeutvidelser på en bro. Siden reaksjonen er avhengig av vann for å ekspandere, kan ekspansjonen i betongen være ulik over et brotvernsnitt. Ulik ekspansjon over tverrsnittet kan føre til endret krumningstilstand for et brotvernsnitt. I statisk ubestemte broer kan forlengelse og endret krumningstilstand over et tverrsnitt gi tilleggskrefter denne typen broer ikke var designet for.

Elgeseter bro i Trondheim er en av broene som er skadelidende av alkalireaksjoner. Feltundersøkelser har påvist store vertikale sprekker ved de originale nullmoment- seksjonene i de innerste bjelkene på broa, 4.5m fra opplagersøylene. En mengde mindre riss er også observert i feltene i de innerste bjelkene. Disse sprekkeene er antatt å skyldes tilleggskrefter fra alkali-silika reaksjoner på bruoen og antakelsen om at de ytre bjelkene utvider seg mer enn de innerste, noe som gir en strekktøyning på de innerste bjelkene. Grunnen til at de mest signifikante sprekkeene oppstår ved de original nullmomentpunktene kan forklares med at disse områdene er designet med en begrenset mengde med armering.

Som en del av denne oppgaven har bæreevnen til Elgeseter bro blitt vurdert i lengderetningen. Siden Elgeseter bro ble bygd i 1951 legges NS3473 2003 til grunn ved kapasitetkontroll. Kapasitetkontrollene ble gjennomført uten å ta hensyn til skader på broen eller nedbrytingsparametre som kan ha redusert betongkvaliteten. Moment- og skjærkraftkapasitetene var på den sikre siden når tilleggslaster fra alkalireaksjon ble neglisjert. Ved inkludering av tilleggslaster fra alkalireaksjonen ble momentkapasiteten oversteget i feltet mellom akse 1-2 (15 %), i de indre feltsnittene mellom søylene (27%) og i de originale nullmomentsnittene, 4.5m fra søylene (92%).

Effekter av alkali-silika-laster på Elgeseter bro ble undersøkt nærmere ved å ta i bruk elementprogrammet DIANA til å lage en 2D modell (lengderetningen) og en 3D modell av broa. Bruk av temperaturlaster ble valgt som løsningsstrategi for simulere alkali-ekspansjon på broen (termisk utvidelseskoeffisient i armering ble satt til null). Begge modellene påviste store strekkspenninger i områdene rundt nullmomentpunktene. Utviklingen av sprekker i betongen funnet ved 2D modellen virket å stemme bra med de som er dokumentert på broen. Med 3D modellen var det også mulig å detektere skjærspenninger som oppstår i plata på grunn av forskjellig tynning over bredden av bruva ved endespenning.

Table of Contents

Preface	i
Abstract	iii
Sammendrag	v
Table of Contents	xi
List of Tables	xiv
List of Figures	xviii
1 Introduction	1
1.1 Background	1
1.2 Purpose and scope	2
1.3 Method	2
2 Damage to concrete structures	3
2.1 Introduction	3
2.2 Service life	3
2.3 Degradation of concrete	4
2.3.1 Freeze-thaw cycle	5
2.3.2 Sulfate attack	7
2.3.3 Alkali Silica Reaction (ASR)	8
2.4 Reinforcement corrosion	9
2.4.1 Carbonation induced corrosion	9
2.4.2 Chloride- induced corrosion	9
3 Structural effect of damage to concrete structures	11
3.1 Combination of cracks and spalling	11
3.2 Reinforcement corrosion	12

3.2.1	Reduction in cross section of reinforcement bars	12
3.2.2	Cracking or spalling of concrete cover due to reinforcement corrosion	13
3.2.3	Hydrogen embrittlement	13
3.2.4	Service life of reinforced structures	14
3.3	Alkali Silica reaction (ASR)	15
3.3.1	Expansion and crack formation	15
3.3.2	Concrete degradation	15
3.3.3	Additional loads from alkaline- reactions	16
3.3.4	Calculation methods for reinforced concrete beams/ plates	21
4	Elgeseter bridge	27
4.1	Introduction	27
4.2	Structural design of the bridge	27
4.3	Statically system, longitudinal direction	28
4.4	Elongation of the bridge	29
4.5	The state of the superstructure	30
4.5.1	Degree of expansion over the width of the cross- section	32
4.5.2	Conclusion from special investigation	33
4.6	Preventive actions on Elgeseter bridge	34
5	Materials	35
5.1	Concrete	35
5.2	Reinforcement	36
6	Loads	39
6.1	Permanent loads	39
6.1.1	Minimum wearing course load	39
6.2	Variable loads	40
6.2.1	Traffic load	40
6.2.2	Wind load	43
6.2.3	Temperature load	45
6.3	Deformation load - Alkali-Silika reaction (ASR)	49
6.4	Ultimate limit state	49
6.5	Vertical line load on internal T-beams	50
6.5.1	Dead load	51
6.5.2	Traffic load	52
6.5.3	Wind load	53
6.5.4	Temperature load	54
6.5.5	ASR load	54
7	Analysis of loads in Robot - Longitudinal direction	59
7.1	Building the model	59
7.1.1	Dead load, traffic load, and wind load model	59
7.1.2	ASR and temperature model	59
7.2	Moment	61

7.2.1	Dead load	61
7.2.2	Traffic load	61
7.2.3	Wind load	63
7.2.4	Temperature	64
7.2.5	ASR expansion	65
7.3	Shear forces	66
7.3.1	Dead load	66
7.3.2	Traffic load	66
8	Ultimate limit state - longitudinal direction	67
8.1	Section forces	68
8.1.1	Moment	68
8.1.2	Shear forces	70
8.2	Section capacity	71
8.2.1	Moment capacity	71
8.2.2	Shear capacity	79
8.3	Degree of utilization: Comparing design forces and capacity	82
8.3.1	Moment	82
8.3.2	Shear	82
9	2D model Elgeseter bridge: Nonlinear analysis	83
9.1	Solution strategy to model the ASR expansion in the superstructure	84
9.2	Creating the model	84
9.2.1	Defining shapes	84
9.2.2	Defining material properties of shapes	85
9.2.3	Defining heat flow properties of the shapes	87
9.2.4	Interface elements	87
9.2.5	Structural boundary conditions	87
9.2.6	Dead load	88
9.2.7	Temperature loading	88
9.2.8	Meshing	89
9.3	Defining the analysis	90
9.3.1	Time steps	90
9.3.2	Time dependent heat flow analysis	91
9.3.3	Structural nonlinear time dependent analysis	91
9.3.4	Results: Transient heat flow analysis	92
9.4	Results: Non- linear structural analysis	93
10	Inspection of strain state of the T- beam in the longitudinal direction due to internal and external loading	105
10.1	Introduction	106
10.2	Control of result from TNO Diana model, Internal span (axis 6-7), field section C-C, time step 42	107
11	3D model Elgeseter bridge: Linear static analysis	109
11.1	Creating the model	110

11.1.1	Defining parts	110
11.1.2	Structural boundary conditions	111
11.1.3	Loading	111
11.1.4	Meshing	112
11.2	Defining linear static analysis	112
11.3	Results, load combination 2 (Only ASR loading)	113
11.3.1	Displacement Dtx	113
11.3.2	Strain, EXX	114
11.3.3	Shear stresses, SZX, end axis	115
11.3.4	Normal stresses, SXX, internal span	115
11.3.5	Reinforcement stress, SXX, internal span	116
11.4	Effective flange width considerations	117
11.4.1	Normal stresses, SXX	117
11.4.2	Reinforcement stress, SXX	118
12	Discussion	121
12.1	ULS Elgeseter internal T-beams, longitudinal direction	121
12.2	Finite element modeling of Alkali-Silica reactions	122
12.2.1	Simple T-beam model (2D) vs. 3D model of the bridge	122
12.2.2	Capacity of original zero moment spots	125
12.3	Consequences of forming plastic hinges	126
12.4	Recommendations of preventive actions on Elgeseter bridge	126
13	Conclusion	129
13.1	Literature review about damage to concrete structures	129
13.1.1	Alkali- silica reactions	130
13.2	Structural safety assessment of inner T- beams (ULS), longitudinal direction	130
13.2.1	Loads	130
13.2.2	Capacity control	130
13.3	Investigation of alkali- reactions on Elgeseter bridge using FEM- models .	131
	Bibliography	131
	Appendix	135
A	Calculation of wind load	136
B	Calculation of second moment of area, Stadium I	140
C	Moment capacity calculations	141
C.1	Section A-A	142
C.2	Section B-B	144
C.3	Section C-C	146
C.4	Section D-D	148
C.5	Section E-E	151
D	Verification of moments and shear forces from Robot with hand calculations	154
D.1	Dead load	155
D.2	Thermal load	156
D.3	Alkali- Silica expansion load	158

E	Control of strain state in field section C-C at time step 42 from DIANA 2D model with hand calculations	160
---	--	-----

List of Tables

5.1	Concrete strength. (Norwegian Public Roads Administration, 2014)	35
5.2	Concrete properties	36
5.3	Reinforcement properties	37
6.1	Wind load without simultaneously acting traffic load	45
6.2	Wind load acting simultaneously with traffic load	45
6.3	Combinations of uniform and vertical temperature components	48
6.4	Final temperature combinations	49
6.5	Ultimate limit state load combination according to Handbook R412	50
6.6	Lorry model applied to T-beam	53
8.1	Load combinations section A-A [kNm]	68
8.2	Load combinations section B-B [kNm]	68
8.3	Load combinations section C-C [kNm]	68
8.4	Load combinations section D-D [kNm]	69
8.5	Load combinations section E-E [kNm]	69
8.6	R412 load combination a, including ASR moment, field sections A-A, B-B, C-C [kNm]	70
8.7	Section F-F	70
8.8	Properties field sections (A-A, B-B, C-C)	74
8.9	Moment capacities field sections (A-A, B-B, C-C)	74
8.10	Key properties zero moment section (F-F)	76
8.11	Properties support sections (D-D, E-E)	77
8.12	Moment capacity and controls section (D-D and E-E)	78
8.13	Moment capacity of the different sections	78
8.14	Degree of utilization, moment capacity: not including external ASR expansion moment	82
8.15	Degree of utilization, moment capacity: including external ASR expansion moment, section A-A, B-B, C-C	82
8.16	Degree of utilization shear capacity	82

9.1	DIANA 2D analysis: Selection of time steps	90
-----	--	----

List of Figures

2.1	Causes of deterioration of reinforced concrete structures (Bertolini et al., 2013)	4
2.2	Surface scaling	6
2.3	External sulfate attack	7
2.4	ASR - map cracking at railway bridge in Trondheim	8
3.1	Structural consequences of corrosion in reinforced concrete structures . . .	12
3.2	Spalling due to voluminous corrosion products	13
3.3	Brittle failure of prestressing tendons due to hydrogen embrittlement (Bertolini et al., 2013)	13
3.4	Service life of reinforced structures	14
3.5	Different models of force development in a fixed beam (at both ends) dependent on the state of the cross- section (stadium I or II) and the degree of expansion (Norwegian Public Roads Administration, 2016).)	18
3.6	Statically determined system: Curving of the T-beam due to more expansion in the upper plate	18
3.7	Statically undetermined T-beam, with more expansion in the upper plate. .	19
3.8	Change of the moment diagram due to more expansion in the plate	19
3.9	Example: External moment from curvature of beam limited by the zero moment capacities	20
3.10	Beam with columns fixed to the beam	20
3.11	Load model 1 and 2 (modified figure) (Norwegian Public Roads Administration, 2016)	21
3.12	Load model 1	22
3.13	Load model 2	23
3.14	Step 3: Finding internal forces in reinforcement and concrete	25
3.15	Step 4: Adding forces from step 2 with opposite sign to achieve equilibrium with external forces	26
4.1	Overview of Elgeseter bridge	28

4.2	Cross- section of bridge- deck (original drawings)	28
4.3	Statically system of Elgeseter bridge, longitudinal direction	28
4.4	Elongation of the bridge, based on measurments at expansion joint (modified) (Aas Jacobsen, 2013).	29
4.5	Localization of cracks (Aas Jacobsen, 2013).	30
4.6	Cracks appearing at the original zero moment section between axis 8-9, 4,5m after axis 8. (Aas Jacobsen, 2013)	30
4.7	Cracks appearing at the original zero moment section (eastern inner beam) between axis 6-7, 4,5m before axis 7. (Aas Jacobsen, 2013)	31
4.8	Typical cracks occurring in the field sections. Closed in bottom and top. (Picutre taken between axis 5-6) (Aas Jacobsen, 2013)	31
4.9	Picture taken at axis 1 showing the western side of the bridge deck (Aas Jacobsen, 2013).	32
4.10	Cross- section of the bridge marked with the areas where the degree of Alkali- Silica reactions is assumed to be high (Aas Jacobsen, 2013).	32
4.11	Reinforcement at inner beams supports, axis 2-8	33
4.12	Column top cut off and replaced	34
4.13	Test project using carbon fiber strengthening at inner beams. Glued to the beams with epoxy. Mechanical anchor at ends (Aas Jacobsen, 2015)	34
6.1	Load models in relation to bridge class.Norwegian Public Roads Administration (2014)	41
6.2	Lorry load model	42
6.3	Width of the loads	42
6.4	Axis system for wind loads - m ha kilde her	44
6.5	Uniform temperature components	46
6.6	Linear vertical temperature difference components	47
6.7	T- beam simplification	50
6.8	T-beam materials	51
6.9	Worst load case above internal T-beam.	52
6.10	Wind load on most loaded T-beam	53
6.11	Assumed strain state from the expansion in the calculations. Modified figure (Norwegian Public Roads Administration, 2016)	55
6.12	Calculation of curvature due to more expansion in the plate	56
6.13	Equivalent curvature strain	57
7.1	Traffic, dead load and wind load model in Robot structural analysis	59
7.2	T-section, Elgeseter, Robot Structural Analysis	60
7.3	Model of Elgeseter bridge with columns in Robot Structural Analysis	60
7.4	Dead load moment	61
7.5	Lorry load model: Max support moments	61
7.6	Lorry load model: Max moment support 9	62
7.7	Lorry load model: Max field moment axis 9-10	62
7.8	Lorry load model: Max field moments	62
7.9	Max support- moment axis 9 from wind	63
7.10	Max support- moment axis 7 from wind	63

7.11	Max field moment	63
7.12	Moment diagram uniform expansion, $\Delta T_{N,exp}$	64
7.13	Moment diagram vertical heat component, $\Delta T_{M,heat}$	64
7.14	Moment diagram vertical cool component, $\Delta T_{M,cool}$	64
7.15	Moment diagram uniform ASR component, $\Delta ASR_{N,exp}$	65
7.16	Moment diagram ASR difference component, $\Delta ASR_{M,plate}$	65
7.17	Total ASR expansion, $\Delta ASR_{N,exp} + \Delta ASR_{M,plate}$	65
7.18	Shear force diagram dead load [kN]	66
7.19	Lorry load model; Positioning of loads	66
7.20	Max shear force lorry load model [kN]	66
8.1	Illustration of sections	67
8.2	Internal T-beams	71
8.3	Flange in compression zone	72
8.4	Flange in compression zone	73
8.5	Moment capacity at zero moment spots	75
8.6	Flange on tensile side	76
9.1	Illustration of selected temperature expansion	83
9.2	DIANA 2D model of Elgeseter bridge	84
9.3	DIANA 2D model: Modeling of steel hinge axis 9	85
9.4	DIANA 2D model: Geometry of reinforcement, axis 3-8	85
9.5	DIANA 2D model: Concrete properties, beam and plate	86
9.6	DIANA 2D model: Relation between strain and stress, reinforcement	86
9.7	DIANA 2D model: Supports	87
9.8	DIANA 2D model: Dead load; time dependent factor	88
9.9	DIANA 2D model: Heat flux; time dependent factor	89
9.10	DIANA 2D model: CQ16M- elements to the left and CT12M- elements to the right (BV, 2012)	89
9.11	DIANA 2D model: CL12I interface element (BV, 2012)	89
9.12	DIANA 2D model: Meshing over internal support	90
9.13	DIANA 2D model: Illustration of temperature field for selected time steps	92
9.14	DIANA 2D model: Temperature in beam and plate, time steps 1-46	92
9.15	DIANA 2D model: Displacement x, illustration	93
9.16	DIANA 2D model: Displacement x, time steps 1-46	93
9.17	DIANA 2D model: Displacement y, illustration	94
9.18	DIANA 2D MODEL: Stresses in concrete, $\sigma_{c,xx}$, internal span (axis 6-7)	95
9.19	DIANA 2D model: Node plot, compression stress concrete, $\sigma_{c,xx}$	97
9.20	DIANA 2D model: Crack width, internal span (axis 6-7)	98
9.21	DIANA 2D model: reinforcement stress ($\sigma_{s,xx}$), internal span (axis 6-7)	99
9.22	DIANA 2D model: reinforcement strain ($\varepsilon_{s,xx}$), internal span (axis 6-7)	100
9.23	DIANA 2D model: Reinforcement strain, ($\varepsilon_{s,xx}$), 4.5m from the column in axis 6 at time step 46	101
9.24	DIANA 2D model: Plot reinforcement strain, ($\varepsilon_{s,xx}$), zero moment spot	101
9.25	DIANA 2D model: Crack width, EcwYY, internal span (axis 6 -7)	102
9.26	DIANA 2D model: Plot section strain, time step 42 (section C-C)	103

10.1	Strain field section	106
10.2	Elastic capacity of zero moment sections limiting the increase of field moment from ASR expansion	107
10.3	Strain state	108
11.1	DIANA 3D model: Selection of temperature load	109
11.2	DIANA 3D model. X-axis follows longitudinal direction of the bridge	110
11.3	DIANA 3D model: Geometry cross- sections	110
11.4	DIANA 3D model: Reinforcement in internal T-beams over supports	111
11.5	DIANA 3D model: Meshing	112
11.6	DIANA 3D model: Elements	112
11.7	DIANA 3D model. Load-combination 2: Displacement Dtx	113
11.8	DIANA 3D model. Load-combination 2: Strain plot, internal T-beam	114
11.9	DIANA 3D model. Load combination 2: Shear stresses at end span, Cauchy total stresses SZX	115
11.10	DIANA 3D model. Load combination 2: Span between axis 6-7, Cauchy total stresses SXX	115
11.11	DIANA 3D model. Load combination 2: Span between axis 6-7, underside, Cauchy total stresses SXX	116
11.12	DIANA 3D model. Load combination 2: Field between axis 6-7, Cauchy total stresses SXX	116
11.13	DIANA 3D model. Load combination 1: Cauchy total stresses SXX	117
11.14	DIANA 3D model. Load combination 2: Cauchy total stresses SXX	117
11.15	DIANA 3D model. Load combination 1-3: Cauchy total stresses SXX	118
11.16	DIANA 3D model. Load combination 3: Cauchy total stresses SXX	118
11.17	DIANA 3D model. Load combination 1-3: Cauchy total stresses SXX	119
12.1	Node integration scheme	125

Introduction

1.1 Background

A large percentage of the bridges in Norway are built in concrete. Many of these bridges are getting old, which means that serious assessment is needed to ensure that the structural capacity is on the safe side. Assessment of existing structures is necessary as many of these structures originally were designed for smaller traffic loads than today. During actions of time, it is also common that serious degradation mechanisms can damage concrete structures.

One of the damage types affecting Norwegian bridges is alkali-silica (ASR) reactions. The reaction forms a swelling gel which expands in contact with water. In addition to reduced material properties, expansion could result in severe elongation of a bridge. Elgeseter bridge is one of the bridges suffering from ASR. According to the special investigation carried out by Aas Jacobsen (2013), the bridge deck is believed to be elongated up to 200mm due to ASR- expansion. The investigation also revealed vertical cracks up to 6mm in many of the bridge beams, 4.5m from the columns. The cracks are believed to be caused by the ASR- expansion.

1.2 Purpose and scope

- Survey about different damage types and how they affect the structural behavior of concrete structures, extended with a more in-depth review of damage due to alkali-silica reactions.
- Structural safety assessment (ULS) of Elgeseter bridge in the longitudinal direction, not taking into account structural damages on the bridge.
- Dive further into the topic regarding alkali-silica reactions on Elgeseter bridge. The overall scope is to get an understanding of how Alkali- Silika expansion affects the superstructure of the bridge.

1.3 Method

- Literature review about different damage types and how they affect the structural behavior of concrete structures: The part of the review regarding structural consequences of alkali-silica expansion is mainly based on the *ASR- Guidance for constructive analysis* by the Norwegian Public Roads Administration (2016).
- Robot Structural Analysis is used to calculate shear and moment forces on Elgeseter bridge. The bridge was built in 1951, which means NS3473 2003: *Design of concrete structures* (Norges Standardiseringsforbund, 2003) will be used to calculate the capacity. Traffic loads and load combinations are calculated according to Norwegian Public Roads Administration handbook R412 (Norwegian Public Roads Administration, 2014). Wind and thermal loading are calculated according to the Eurocodes.
- A 2D and a 3D model are made using the finite element program DIANA. In both models, temperature loads are used to simulate the expansion from the alkali-silica reaction. The 2D model is used to run the nonlinear structural analysis, and the 3D model is used to run the linear static analysis. The results from the 2D analysis are controlled using *ASR- Guidance for constructive analysis* by the Norwegian Public Roads Administration (2016).

Damage to concrete structures

2.1 Introduction

Reinforced concrete is a relatively recent construction material as it was first introduced at the end of the 19th century. The application in buildings and structures started to grow after 1900, but became a mainstream construction material only after World War 2. For many years after the introduction of the material, it was considered that these structures were built to last without any further maintenance or repair. Since then, we have learned that serious degradation mechanisms can severely reduce the service life of the structures.

2.2 Service life

The service life of a construction can be studied from at least three different point of view: technical/ structural, functional and economical. This overview will only cover the technical/ structural point of view. When designing a structure, the main goal is to design it durable enough to last for its target service life.

No matter how good the design and construction is carried out, different degradation mechanisms will decrease the quality of the reinforcement concrete. This means that the initial quality of the construction has to be higher than the minimal required level. If the design and construction of the construction is done properly, the construction will reach its service life at the end of its service life under normal conditions. If the environment is more aggressive than predicted, the construction will most probably reach its service life before its target life. When a structure has come to the end of its service life it does not necessary mean that the construction will collapse or must be demolished. However, the safety of

the structure might not be at a very high level. Often economical and profit calculations will be used to decide whether to repair or demolish the construction (De Schutter, 2013).

2.3 Degradation of concrete

Degradation mechanisms of concrete can be classified as physical, mechanical, chemical, biological, and structural.

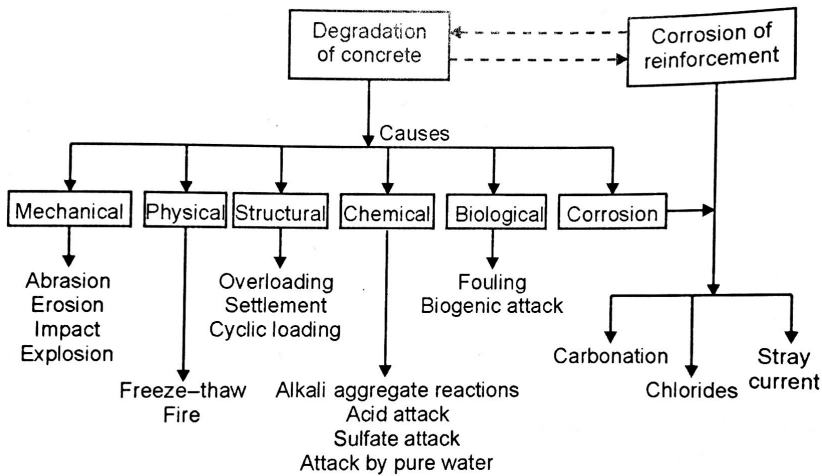


Figure 2.1: Causes of deterioration of reinforced concrete structures (Bertolini et al., 2013)

The processes of deterioration of concrete and corrosion of reinforcement are closely connected. The former provokes destruction of the concrete cover or cause micro-cracking that affect the protective characteristics of the reinforcement. On the other hand, corrosion attack can produce cracking or delimitation of the concrete if voluminous corrosion products are formed that exert expansive action (Bertolini et al., 2013).

2.3.1 Freeze-thaw cycle

The process of freezing water increases the volume by about 9%. If water contained in the pore system of the concrete freeze, the increased pore-pressure can introduce large tensile stresses to the concrete, causing cracking or scaling.

Mechanism

Different theories have been developed giving different views of the real mechanisms occurring during freezethaw cycles in concrete. The most important are the *theory of hydraulic pressure* and the theory of *ice-overpressure*.

According to the hydraulic pressure theory proposed by Powers (1945), the destruction of concrete by freezing is caused by the hydraulic pressure generated by the expansion due to freezing of water. Ice formation is initiated first in the larger pores within the capillary pore structure, and the expanding ice pressurizes the remaining liquid. The pressure can only be released if there are partially empty pores or air voids in the vicinity. If the pressure cannot be sufficiently reduced, the tensile stress could impose degrading cracks in the concrete. Numerous experiments have shown that water tends to travel to, and not from capillary pores where ice is forming. Even though the basic mechanism of the theory is considered to be wrong, authors like Pigeon and Pleau (2010) claims that the theory is well suited to describe the relationship between freezing rate and the maximum distance that water must travel to reach an air void in order to release pressure.

Powers working together with Helmeth later developed the theory of ice- overpressure as an attempt to describe the waterflow during freezing. The fact that the freezing point decrease on decreasing diameter supports this idea. In the gel pores, which is the smallest pores within the concrete, the freezing point has shown to be less than -30 degrees. As liquid water (from gelpores) contains higher levels of free energy than that of ice, the water will try to regain equilibrium by moving towards the capillary pores where the ice is forming. They later proposed a modified theory of the ice overpressure-theory called the osmotic pressure theory, where they also took into consideration the effect of chemicals in the water. As the water starts to freeze, the concentration of ions dissolved in the part of the pore water that is not yet frozen increases. This theory is useful as it show how long freezing periods can be very harmful in certain cases because they promote large ice-crystal growth. It can also help to explain the effect of de-icer salts, which at moderate concentrations, increase the phenomenon of osmotic pressure (Pigeon and Pleau, 2010).

Factors influencing frost resistance

Frost resistance is determined by the number of freeze- thaw cycles that a particular concrete can withstand before reaching a given level of degradation. In general, the mass loss or the decrease of dynamic elastic modulus are applied as indexes of degradation. The degree of saturation of the pores is important for the frost resistance of concrete. Sufficiently close air- filled pores exert a beneficial action because they can collect water to lower the pressure occurring in the capillaries. The water/ cement ratio is another important parameter, on which the porosity of the cement matrix depends. The v/c number should be low as porous concrete rapidly becomes saturated with water and thus sensitive to frost action. Frost resistance increases rapidly with a decrease of the w/c ratio, both for ordinary concrete and for air- entrained concrete (Bertolini et al., 2013).

Freeze- thaw cycle damages

The consequence of a freeze- thaw attack appear as *surface scaling* or *internal cracking*. Surface scaling is characterized by progressive loss of small cement paste or mortar particles. This process gradually exposes the coarse aggregate. Surface scaling normally appears on surfaces where water and snow may naturally deposit. The presence of deicing salts on the surface is also a detrimental factor increasing the damages due to scaling. Surface scaling therefore typically damages concrete structures along roads where they use deicing salts.



Figure 2.2: Surface scaling

Internal cracking leads to expansion and loss of mechanical properties. Internal cracking and disruption are of the type that are found in concrete subjected to rapid freezing and thawing cycles, such as in laboratory experiments. The phenomenon may be observed on parts of structures in direct contact with free water and subjected to capillary suction, such as the lower parts of supporting walls and dam structures above the water surface.

2.3.2 Sulfate attack

If water containing sulfate ions react with the cement matrix of the concrete, it could cause expansive chemical reactions that could have a degrading effect on the concrete.

If water containing sulfate penetrates the concrete through cracks or the pore system from outside, it is referred to as *external sulfate attack*. Swelling often starts at edges or corners of the concrete, giving rise to cracks and disintegration. It can also lead to loss of strength of the cement paste due to loss of cohesion between the hydration products (Bertolini et al., 2013). This kind of attack is not a significant threat towards Scandinavian constructions as the groundwater normally contains low values of sulfate ions (Ahlberg, 2012)



Figure 2.3: External sulfate attack

Internal sulfate attack is often referred to as delayed ettringite formation (DEF). Unlike external sulfate attack, the source of the sulfates is in the concrete itself. Even though contamination of the aggregates in the concrete mix would often promote the attack, DEF may also occur in concretes with sulfate content within ordinary limits. It is a relatively young type of deterioration, as it began to be observed and recognized in the 1980s. It has been argued that the increased amounts of gypsum has given a rise to this kind of deterioration (Bertolini et al., 2013).

2.3.3 Alkali Silica Reaction (ASR)

The ASR reaction forms a swelling gel, which can induce tensile stresses within the concrete and lead to the appearance of cracking. The crack pattern depends on the geometry of the structure, the layout of the reinforcement and the level of tensile stress). In floors or in foundations, elements that are usually only lightly reinforced and do not have significant tensile stress, the typical pattern of cracking is so-called "map cracking" with randomly distributed cracks. The expansion may also lead to so-called *pop-outs*, that can be seen by expulsion of small portions of concrete (Bertolini et al., 2013). Development of ASR may be very slow and its effect may show even after long periods (Page, 2002). ASR will only affect concrete which has alkali reactive aggregates in the concrete. When we design concrete structures today, we know which aggregates we must avoid. Unfortunately, that was not the case in the past. Since the reaction is so slow, it took a long time before this damage mechanism was recognized, which is the reason why so many concrete structures are affected today.



Figure 2.4: ASR - map cracking at railway bridge in Trondheim

Mechanism

The reaction mechanism between alkali and reactive siliceous aggregate is complex. It requires the presence of hydroxyl, alkali metal, calcium ions, and water. The hydroxyl ions provoke the destruction of atomic bonds of the siliceous compounds, the alkali ions react with $Si(OH)_4$ complexes to form a fluid (Na,K)-Si-OH gel, which then exchanges Na and K for Ca, upon which the gel solidifies. The solidified gel absorbs water and swells (Bertolini et al., 2013).

Environment

Alkali - Silica reactions can occur only in moist environment. It has been observed that in environments with a relative humidity below 80-90%, alkali content can coexist with the other reactants without developing deteriorating ASR- gel (Bertolini et al., 2013).

2.4 Reinforcement corrosion

Reinforcement corrosion is the most important damage-type affecting concrete structures. It is commonly known that hydrated concrete has a highly alkaline pore solution, with a pH between 13 and 13.8. In this environment, the reinforcement has a protective oxide film that protects the reinforcement against corrosion. The protective action of the passive film is immune to mechanical damage of the steel surface. It can, however be destroyed by carbonation or by the presence of chloride ions. Once this layer is destroyed, corrosion will occur only if water and oxygen are present on the surface of the reinforcement. Corrosion is often indicated by rust spots that appear on the external surface of the concrete, or by cracking of the concrete cover produced by the expansion of the corrosion products (Bertolini et al., 2013).

2.4.1 Carbonation induced corrosion

Corrosion induced by carbonation are often referred to as *general corrosion*. It takes place on the whole surface of the steel in contact with carbonated concrete.

Carbonation is the reactions of carbon dioxide from the atmosphere with alkaline constituents of concrete. This process starts at the outer layer of the concrete and moves gradually towards the inner zones. Carbonation neutralizes the alkalinity of the concrete to pH values where the passive film is no longer stable. If the concrete contains chlorides bound to hydrated phases in the concrete, the carbonation may liberate these bounds, making the pore solution even more aggressive to corrosion. When the carbonation front has reached the reinforcement, the passive film is no longer stable and corrosion can occur if oxygen and water are present (Bertolini et al., 2013).

2.4.2 Chloride- induced corrosion

Chloride ions can be introduced to the concrete through penetration or by contamination of the concrete mix. Modern design codes have restraints on the amount of chloride ions that may be introduced to the concrete mix.

Chloride- induced corrosion are often referred to as *pitting corrosion* since this type of corrosion normally are restraint to limited areas(pits). Pitting corrosion- attack is typical for wet, chloride- containing concrete and may typically appear on bridge decks where the defective membranes are defect. Nowadays, the risk of assessing corrosion through penetration of chloride ions from seawater or deicing salts are regarded as the most important degradation mechanism for reinforced concrete infrastructure (Bertolini et al., 2013).

When the concrete surface is exposed to chlorides, it can enter the system by diffusion, or by capillary suction of the surface which they are dissolved, or by a combination of the mechanisms. If the concentration of chloride ions at the surface of the reinforcement reach a critical level, the protective layer may be locally destroyed (Apostolopoulos et al., 2013).

The rate of the corrosion depends on the availability of both oxygen and water at the cathode. The unique phenomenon of pitting-corrosion is that severe corrosion can happen even though the cathode is exposed to low values of oxygen. It can be explained by the fact that the anodic sites may be localized to the pit and the rest of the surface of the rebar act as the cathode. As the corrosion product is discouraged from precipitation, and due to the existence of highly active and localized anodic sites, severe pitting corrosion may happen without earlier visible signs at the concrete surface. This can lead to rapid loss of cross-section and at the time when cracks develop and corrosion products becomes visible, the reinforcement may already be significantly damaged (Apostolopoulos et al., 2013).

Structural effect of damage to concrete structures

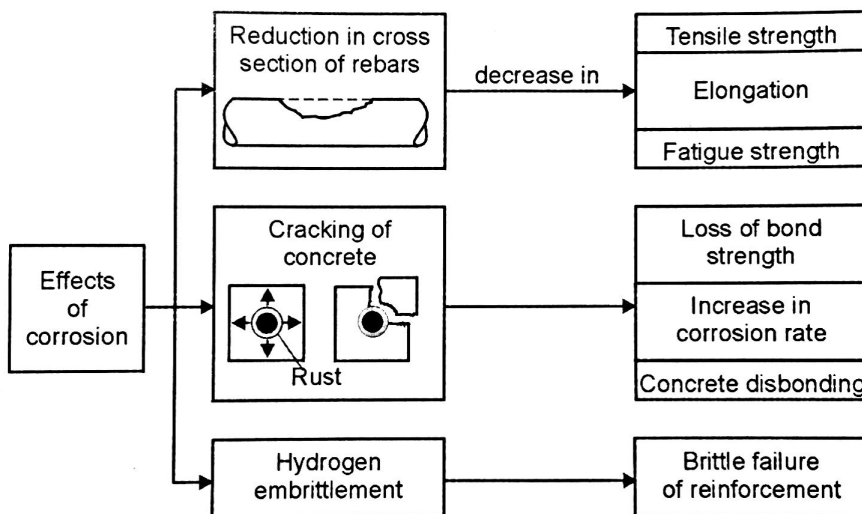
As revealed in section 2.3, the processes of deterioration of concrete and corrosion of reinforcement are closely connected. The different degradation- mechanisms mainly lead to *cracks* or *spalling*, which reduces the resistance towards penetration of aggressive substances to the reinforcement. As the concrete is dependent on the reinforcement to take up tensile stresses, this is the most crucial effect of the different degradation mechanisms. Cracks or spalling may however have other effects, reducing the structural capacity of the structure.

3.1 Combination of cracks and spalling

In some cases when cracks and spalling has destroyed the cross-section to a level where it has fallen apart or the properties of the concrete cover is severely reduced, the load-bearing capacity of the cross-section will be reduced. This is a natural effect as the destroyed parts of the concrete cover can no longer take up the same amount of stresses. The fact that reinforced concrete structures also is dependent on having intact concrete covering the bars to have interaction between the materials is also a crucial factor regarding the structural capacity. If the bond between the reinforcement and the concrete is reduced in the anchorage parts of the bars, the structure can no longer count on the reinforcement to take up the desired amount of stress- forces in the critical sections.

3.2 Reinforcement corrosion

The main structural effects of reinforcement corrosion is shown in figure 3.1. Depending on the conditions of the corrosion it can significantly *reduce the cross-section of the reinforcement bars*. In the process of corrosion voluminous corrosion products are formed which can introduce an expansion action on the concrete cover. If the expansive action surpasses the tensile capacity of the concrete, it can give rise to *cracks or spalling of the concrete cover*. Reinforcement corrosion can also introduce *hydrogen embrittlement* to the reinforcement.



(Bertolini et al., 2013)

Figure 3.1: Structural consequences of corrosion in reinforced concrete structures

3.2.1 Reduction in cross section of reinforcement bars

In cases of chloride-induced localized corrosion, the cross section of the reinforcement can be significantly reduced long before any signs of corrosion becomes visible at the concrete surface, as revealed in section 2.4.2. If the reduction of the cross-section appears at a critical section, it will reduce the load bearing capacity along with the fatigue strength of the reinforcement.

3.2.2 Cracking or spalling of concrete cover due to reinforcement corrosion

Cracking or spalling due to the expansion of concrete products will reduce the effective cross-section of the concrete. It can also reduce the bond of the reinforcement towards the concrete. As cracking or delamination of the concrete cover makes the reinforcement more exposed to aggressive substances, water and oxygen, the corrosion rate will increase.



Figure 3.2: Spalling due to voluminous corrosion products

3.2.3 Hydrogen embrittlement

Under very special conditions that lead to hydrogen embrittlement of high-strength steel, brittle failure of some types of prestressing steel can take place, as shown in figure 3.3.

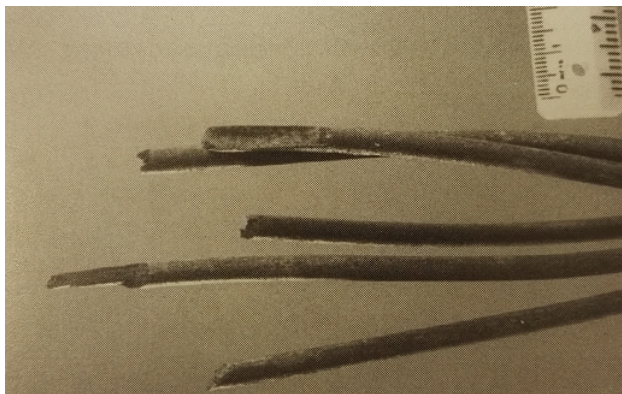
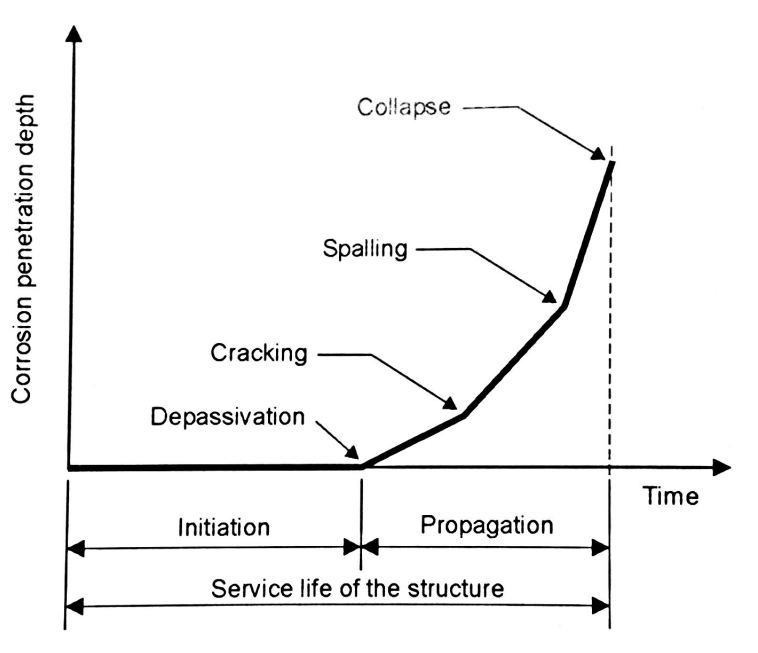


Figure 3.3: Brittle failure of prestressing tendons due to hydrogen embrittlement (Bertolini et al., 2013)

3.2.4 Service life of reinforced structures

The service life of reinforced concrete structures can be divided into two phases, the *initiation phase* and the *propagation phase*. The initiation phase is the phase where the passive film is destroyed by carbonation or chloride penetration, often in combination with other degrading mechanisms. The propagation phase begins when the steel is depassivated and ends when the consequences of corrosion cannot be further tolerated.



(Bertolini et al., 2013)

Figure 3.4: Service life of reinforced structures

3.3 Alkali Silica reaction (ASR)

To reveal the effect on the structural behavior due to alkali-silica reactions, *ASR- Guidance for constructive analysis* by the Norwegian Public Roads Administration (2016) have been used. The background for making this document is because many of the bridges in Norway is affected by alkali-silica reactions. The document aims to develop a guide for constructive analysis of the superstructure (everything above the substructure) of normal reinforced bridges with alkali reactions.

In this document, it is revealed that constructive assessments of alkali reactions in concrete bridges in the past mainly has been linked to the substructure. Many concrete bridges have vertical crack formations in the columns that have been considered in relation to capacity and durability, but the effect due to expansion and elongation of the bridge deck must also be taken into account, as elongation may introduce new moments to the columns that they were not originally designed for.

The guidance proposes some mathematical models that can be used to consider additional loads from alkali-reactions. The contents are limited to the effect of expansion in the longitudinal direction of the bridges.

3.3.1 Expansion and crack formation

Three factors are important when considering the reaction rate and the severity of the expansion:

- reactivity of the aggregate
- the content of alkaline in the concrete
- moisture level

Local variations in the composition and the various moisture levels are important for the degree of expansion on the different parts of the construction. So far, it has not been revealed cases in Norway where the alkali reactions have stopped. For an unrestrained construction, it is believed that the expansion will continue forever. According to Blight and Alexander (2011), the expansion for completely and partly restrained constructions is, however, believed to stop in one direction if the compression-stress in the same direction reach 3-5 Mpa.

3.3.2 Concrete degradation

The nature of the reaction (swelling gel and crack formation) implicates that the main reduction of material properties is related to the tensile strength of the concrete. The degree

of the reduction depends on the expansion and the crack formation. When the expansion is larger than 1 ‰, serious crack formations are considered to reduce the tensile stress to zero locally in some directions. When designing concrete structures, the reinforcement is considered to take all stress-forces. There are, however, some parts of the structure that demands some tensile strength from the concrete in order to have enough capacity. This is mainly related to the shear- and bond strength. For example, it is crucial that the reinforcement has enough bond- strength in the anchorage areas. Alkaline- reactions and crack formations in these areas could cause serious consequences regarding the load capacity of the structure.

According to the FIB model code 2010, the reduction of bond-strength due to alkali-silika depends on the design conditions: *"When laps and anchorages are restrained by links, expansion within the limits 0.45 (restrained) and 4.50 (unrestrained) induced by ASR has been shown to have no significant effect on bond strength. Where transverse reinforcement is not present then bond strength may be reduced by up to 50%. Care is necessary in the assessment of residual resistance of anchorage zones of prestressed elements, particularly of pretensioned members in which the tendons are not contained by links"* (Federation for Structural Concrete, 2013).

The E-modulus of the concrete is assumed to be dependent on how the concrete has expanded. In cases of free expansion, the E- modulus is considered to be low up to the point when the expansion or the gel in the pores are compressed together. When the compression stress in the concrete is larger than 3 Mpa, the reduction of the E- modulus in this direction is assumed to be negligible.

The compression strength is also dependent on the expansion. However, this reduction is only assumed to be present when the expansion is high ($\geq 2\text{-}3$ ‰) or in cases of delamination.

3.3.3 Additional loads from alkaline- reactions

Expansion of the concrete from alkaline- reactions are assumed to be a long time- effect. In reinforced concrete, this expansion will give additional loads on the structure that has to be considered along with dead load and other loads acting on the construction (environmental, live- loads etc). The additional loads from expansion can in some cases be large and proper models is needed in order to calculate these forces when assessing capacity controls of these structures.

When considering additional loads due to the expansion from the alkali-silica reactions, the guidance distinguishes between two load-effects: the inner load-effect and the external load-effects.

Inner load-effects

When a reinforced concrete structure suffers from alkali-silica, only the concrete will expand. The reinforcement will, however, be strained by following the concrete expansion. The stresses on the reinforcement will introduce additional moment and axial forces on the cross-section. The increased action in the reinforcement will be kept in equilibrium by the concrete, which means that it will be a change in the stress- state in both the reinforcement and the concrete due to the expansion. The inner load-effect due to ASR expansion will only give rise to increased stresses as long as the material-behavior is linear elastic. The ultimate moment capacity of a section is calculated when the reinforcement is yielding which means inner load effects will be of small importance. The inner load-effect from the expansion can instead be considered to be an inner pre-tensioning of the cross-section.

The strain state of the cross-section will, however, be of importance regarding the response of the cross-section. Which strain- state the cross- section is in will depend on external loads and the degree of the expansion. A load-bearing structure will however mostly be in stadium II (Only the reinforcement is considered to take up stresses) during the expansion due to simultaneously acting dead-load and varying environmental and live loads.

External load- effects

Expansion and axially restrained at end abutments

If the construction is fixed against elongation or rotation (in both ends), the expansion will also give outer load effects. If the cross-section is in stadium I, the expansion will introduce a constant pressure over the cross-section, as shown in figure 3.5.1. If the cross-section is in stadium II, most of the pressure will be introduced through the compression-zone over the supports, as shown in figure 3.5.2. Depending on the degree of the expansion in relation to the dead load, the beam might be lead back to stadium II, as shown if figure 3.5.3 and 3.5.4.

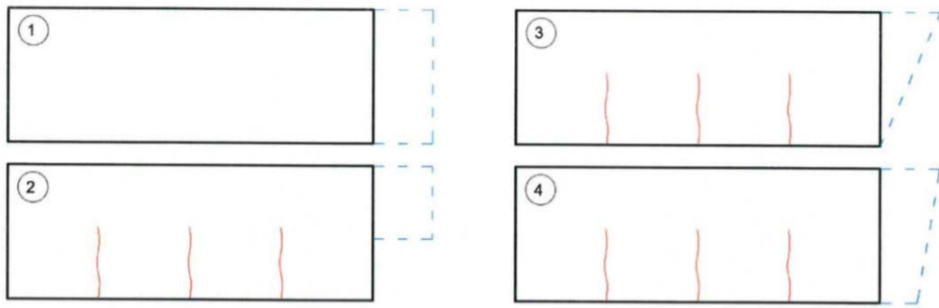


Figure 3.5: Different models of force development in a fixed beam (at both ends) dependent on the state of the cross- section (stadium I or II) and the degree of expansion (Norwegian Public Roads Administration, 2016).)

Vertical expansion difference component, $\Delta ASR_{M,plate}$

In a T-beam with more expansion in the top plate than in the beam, the T-beam will tend to curve upwards. As shown in figure 3.6 the T-beam is exposed to more expansion in the plate, which result in an upwards curving of the beam. As the beam is statically determinate, nothing will restrain the upwards curving, resulting in zero forces and moments due to the expansion along the beam.

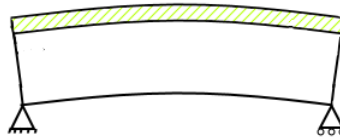


Figure 3.6: Statically determined system: Curving of the T-beam due to more expansion in the upper plate

If the same T-beam was exposed to the same expansion load along the beam, but in a system with more than two supports, like in figure 3.7, the expansion load would contribute to external moment and forces on the T-beam. This is because the inner beams are restraining the upwards curvature (displacement) of the beam. When the amount of supports increases, the moment diagram tends to have a more or less constant value in the internal spans.

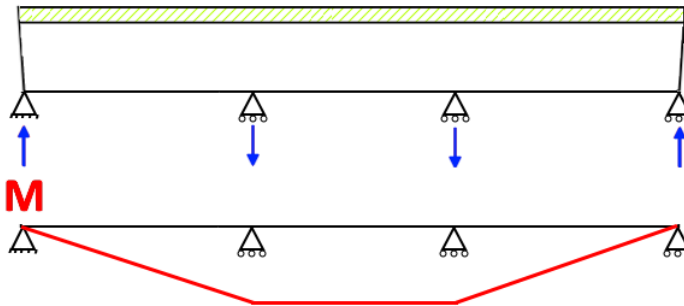


Figure 3.7: Statically undetermined T-beam, with more expansion in the upper plate.

Combining this additional moment with dead load moment, the field moments has increased and the support moments has decreased, as shown in figure 3.8. The shift in the moment diagram due to more ASR expansion in the plate can introduce significant moments at the original zero moment spots. As these sections usually have a minimum amount of tensile reinforcement, the elastic moment capacity may be exceeded, forming plastic hinges.

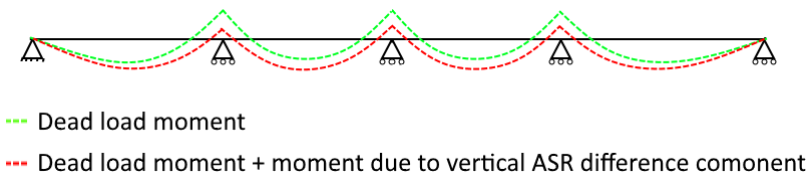


Figure 3.8: Change of the moment diagram due to more expansion in the plate

The state of the original zero - moment spots are of importance when evaluating the increased moment in the field sections. As the moment due to more expansion in the plate is more or less constant in the internal spans, the maximal increase of the field moment sections is limited by the ultimate (characteristic) moment capacity of the zero moment spots, M_i , as shown in figure 10.2.

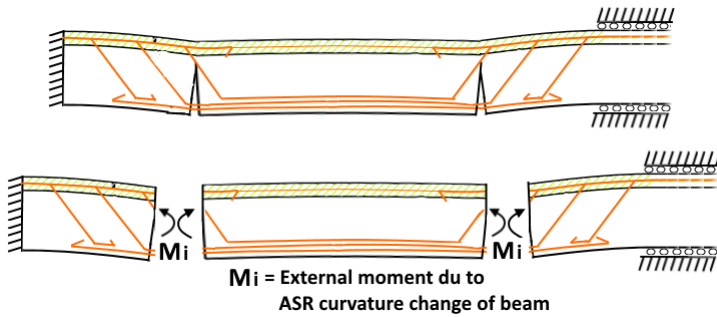


Figure 3.9: Example: External moment from curvature of beam limited by the zero moment capacities

Uniform ASR expansion component, $\Delta ASR_{N.exp}$

Moments induced at the supports due to even expansion over the cross-section is shown in figure 3.10.

Assuming the expansion joint at the end axis is intact, beam-plate bridges are almost free to elongate due to small resistance from the columns. Since the axial force in the bridge deck is so small, it can be neglected in these type of construction (Norwegian Public Roads Administration, 2016).

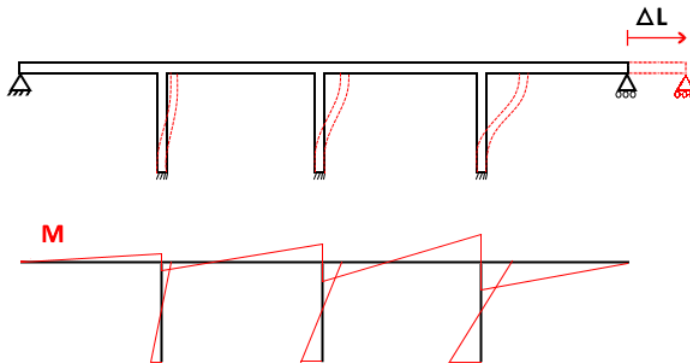


Figure 3.10: Beam with columns fixed to the beam

3.3.4 Calculation methods for reinforced concrete beams/ plates

The guidance suggest three load models to cover the expansion from Alkali-Silika expansion:

- Load model 1: Beam or plate with even (constant) or linear expansion over the cross- section
- Load model 2: beam or plate with more expansion in the upper part of the cross- section. (Example: T-beam with more expansion in the plate than in the web)
- Load model 3: Plate or T-beam with different expansion over the width of the cross- section. (Example: One of the bridge beam- plate T-beams has larger expansion than other T-beams)

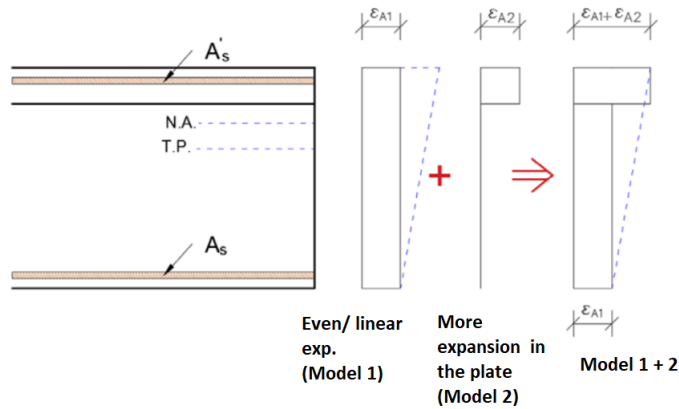


Figure 3.11: Load model 1 and 2 (modified figure) (Norwegian Public Roads Administration, 2016)

As ASR expansion is a long time load effect, the guidance recommends using the long-time E-module, having a creep number equal to 2 as a minimum value.

Internal load effects

Load model 1

Even expansion of a reinforcement beam or plate will introduce additional forces to the cross-section. The axial compression force appears as the concrete expansion strains the reinforcement. If there are different amounts of reinforcement over the height of the cross-section it will also introduce additional moments on the reinforcement, as shown in figure 3.12 for a T-beam cross-section.

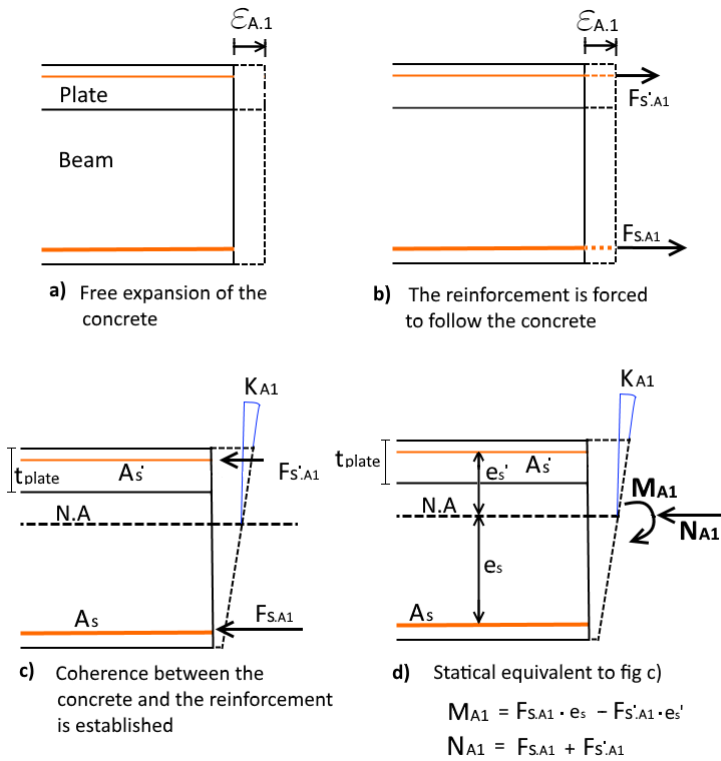


Figure 3.12: Load model 1

Load model 2

A beam or plate with more expansion in the top of the cross-section will introduce additional moments to the cross-section. Figure 3.13 shows how the additional axial force and moment can be considered for a T-beam with expansion in the top plate.

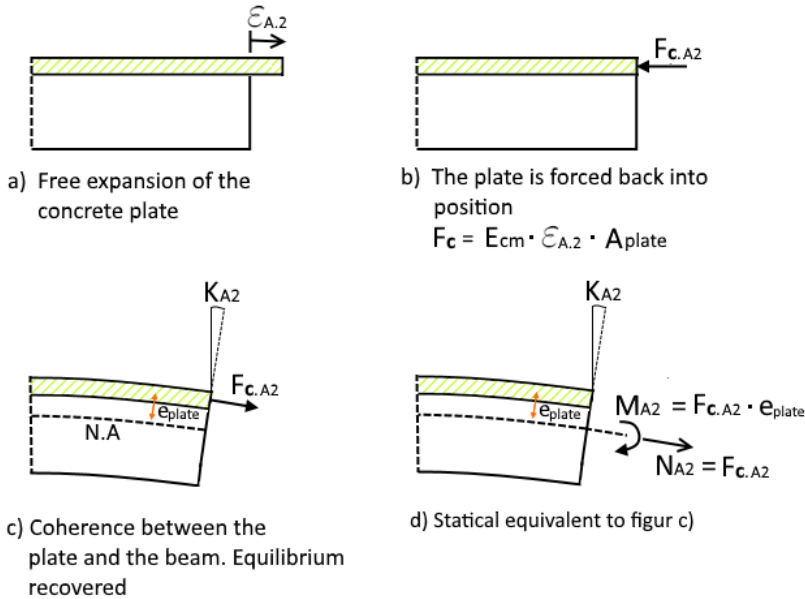


Figure 3.13: Load model 2

Load model 3

When calculating the internal load effects on the cross-section due to load model 3, the same principles as in load model 1 and 2 can be used. The only difference for load model 3 is that load model 1 and 2 are used over the width of the cross-section instead of the height (Norwegian Public Roads Administration, 2016).

External load effects

As revealed in section 3.3.3, uniform and different expansion over the cross-section will introduce external forces on structurally undetermined systems. The external forces on the structure from load model 1, 2 and 3 can be treated in frame structure programs by applying equivalent temperature expansion.

Combining internal and external loads

The additional load effect on the cross-section can from the internal load models can be calculated with step 1-5:

Step 1

- Determine if the section should be considered non-cracked (stadium I) or cracked (stadium II).
- Calculate neutral axis, $(NA)_I$ or $(NA)_{II}$.
- Calculate bending stiffness of section, $(EI)_I$ or $(EI)_{II}$

Step 2

Calculating axial force and moment from the internal load models on the section ($M_{internal}$ and $N_{internal}$). Select assumed expansion $\varepsilon_{A.1}$ and $\varepsilon_{A.2}$ from load model 1 and 2.

- $M_{internal} = M_{A.1} + M_{A.2}$
- $N_{internal} = N_{A.1} + N_{A.2}$

Step 3

Determine external loads on the section ($M_{external}$ and $N_{external}$) from dead load, external ASR load effects, traffic load etc.

Calculate total axial force and moment on the cross-section:

- $N = N_{external} + N_{internal}$
- $M = M_{external} + M_{internal}$

Step 4

Calculate internal forces in the cross-section (F_s , F_c and F'_s) due to moment (M) and axial force (N) from step 3. Internal forces in the reinforcement and concrete can be calculated by finding the axial strain- and curvature- strain component, as shown in figure 3.14.

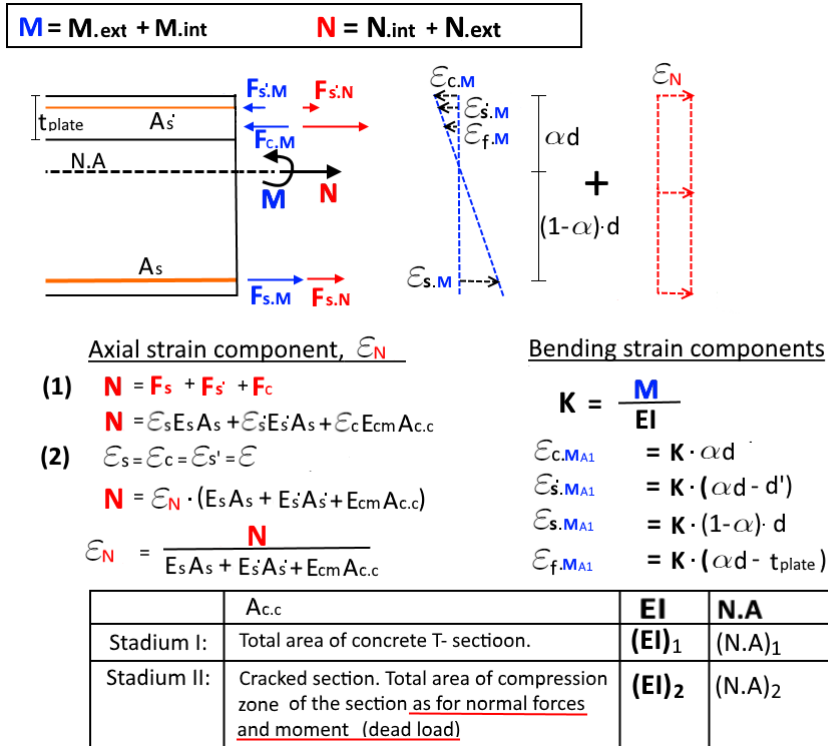


Figure 3.14: Step 3: Finding internal forces in reinforcement and concrete

Step 5

In the end step, the calculated forces from the internal load models (step 2) are added to the internal forces calculated in step 4, in the opposite direction. The internal forces in the reinforcement and concrete ($F_{s.final}$, $F_{c.final}$ and $F'_{s.final}$) are now in equilibrium with the external forces, ($M_{external}$ and $N_{external}$).

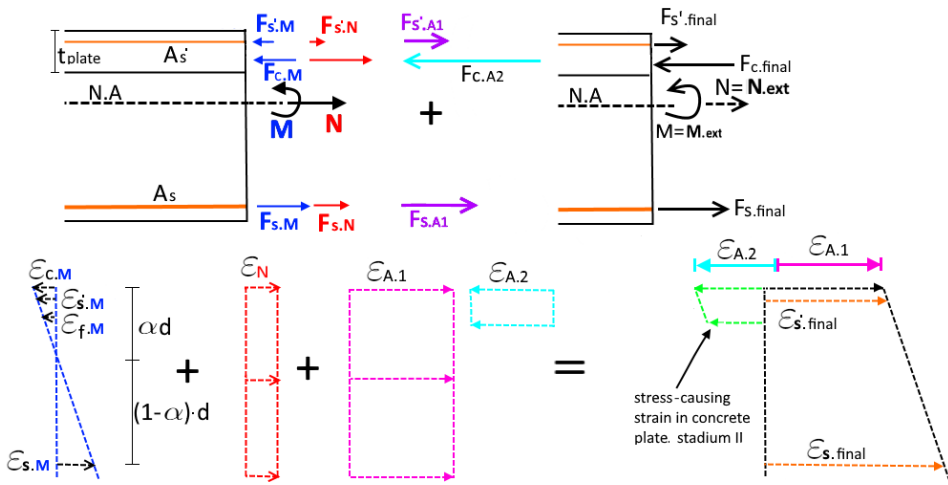


Figure 3.15: Step 4: Adding forces from step 2 with opposite sign to achieve equilibrium with external forces

Chapter 4

Elgeseter bridge

4.1 Introduction

Elgeseter bridge (1951) in Trondheim is one of the bridges that is affected by Alkali- Silika reactions.

- Finished in 1951
- Concrete slab- beam bridge with 9 spans
- 200m long with 10 rows of columns
- Cross-section with four beams in the longitudinal direction

4.2 Structural design of the bridge

The bridge consists of 9 spans. The first and last spans are 21.25m while the rest of the spans are 22.5m. The main load-bearing system consists of 4 continuous beams with c/c 5.5m carried by columns 800mm. The bridge is oriented in the north-south direction, with axis 1 at the southern side. At axis 1, the bridge is fixed into the 9m long abutment. At the northern end, in axis 10 the bridge deck is roller supported to the columns with an expansion joint. The columns at axis 10 are fixed to the abutments. The columns in axis 2-8 are monastically casted to the superstructure, while the columns in axis 9 are hinged to the superstructure.

According to the bridge drawings, the height of the columns in axis 2-8 is 15m, while the columns in axis 1 and 9 are 10m.

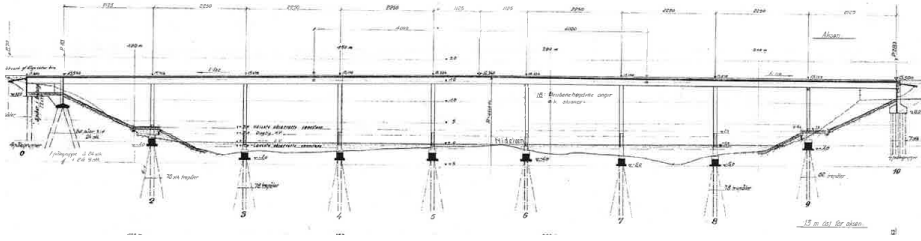


Figure 4.1: Overview of Elgeseter bridge

The total width of the bridge is 23.50 meters, where total road-width is 16.50 meters, and the remaining 7 meters are sidewalks, 3.50 meters on each side.

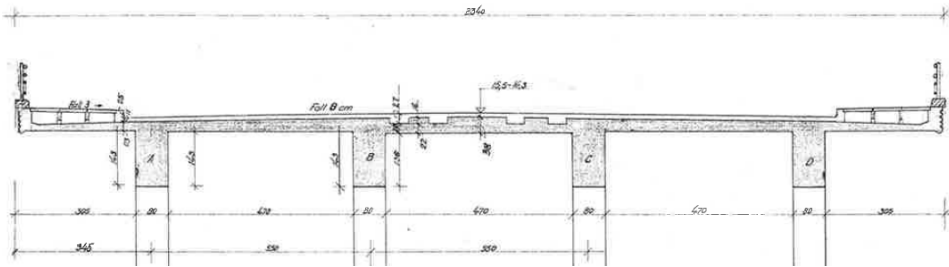


Figure 4.2: Cross-section of bridge-deck (original drawings)

4.3 Statically system, longitudinal direction

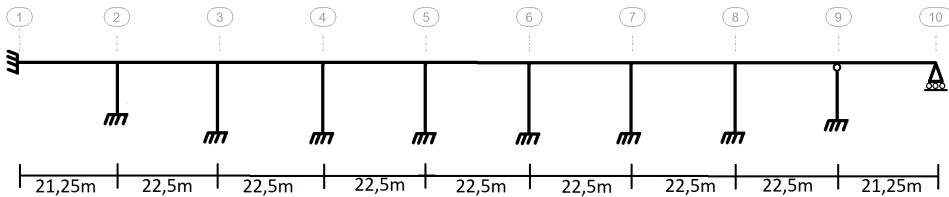


Figure 4.3: Statically system of Elgeseter bridge, longitudinal direction

4.4 Elongation of the bridge

The total elongation of the bridge is important in order to quantify the internal and external loads from the Alkali- reaction on the bridge.

Two types of measurements have been assessed to quantify the elongation of the bridge. Figure 4.4 shows the elongation based on the reduction of the expansion joint opening at the end axis. The elongation is based on measurements collected in the period 1962 to 2001, at four measurement points (Pkt 1- Pkt 4). Assuming a linear elongation in the period 1950 to 2000, the average elongation is estimated to be 3.2mm per year (Aas Jacobsen, 2013).

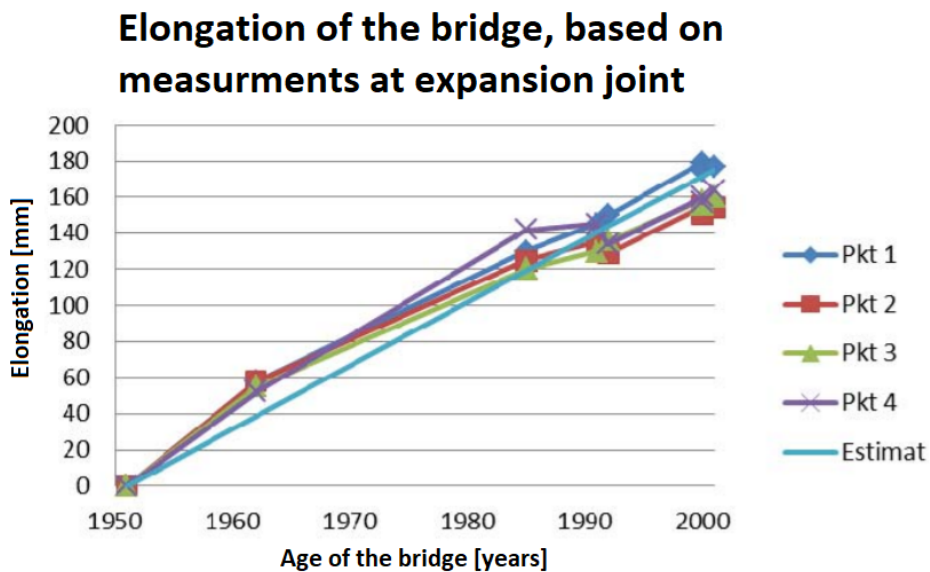


Figure 4.4: Elongation of the bridge, based on measurments at expansion joint (modified) (Aas Jacobsen, 2013).

As movements of the end abutment may influence the measurements, Aas Jacobsen (2013) questions the accuracy of the estimated elongation based on the former method. There are established measurement bolts underneath the outer beams at the first and last abutments (axis 1 and 10) to follow the continued elongation of the bridge (Aas Jacobsen, 2013).

The second method used to quantify the elongation is based on relative movements of the columns. By comparing the bottom and top position of the columns, an estimation of the

elongation was made in 1991. By this method, the elongation of the bridge was estimated to be 2.5mm/ year (Aas Jacobsen, 2013).

4.5 The state of the superstructure

During the main- inspection in 2011 it was revealed up to 6mm vertical cracks occurring 4.5m from the columns at the inner beams, as shown in figure 4.5, 4.6 and 4.7. It was also revealed smaller cracks occurring in the field sections of the inner beams. In contrast to the cracks occurring 4.5m from the columns, the cracks occurring in the field sections were closed in the bottom and top, and reached its maximal width in the middle of the beam, as shown in figure 4.8.

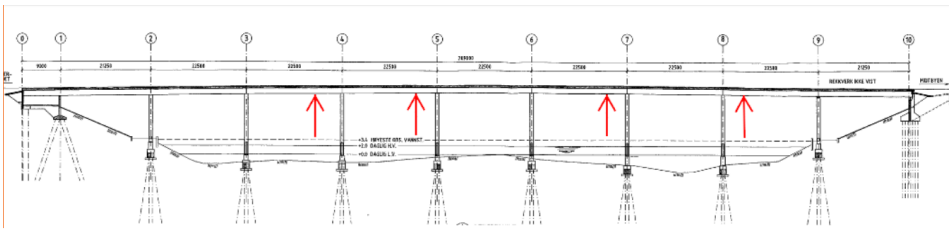


Figure 4.5: Localization of cracks (Aas Jacobsen, 2013).



Figure 4.6: Cracks appearing at the original zero moment section between axis 8-9, 4,5m after axis 8. (Aas Jacobsen, 2013)



Figure 4.7: Cracks appearing at the original zero moment section (eastern inner beam) between axis 6-7, 4,5m before axis 7. (Aas Jacobsen, 2013)



Figure 4.8: Typical cracks occurring in the field sections. Closed in bottom and top. (Picutre taken between axis 5-6) (Aas Jacobsen, 2013)

4.5.1 Degree of expansion over the width of the cross- section

Based on the degree of saturation and field observations, Aas Jacobsen (2013) assumes that the outer parts of the bridge deck are more exposed to alkali-silica reactions than the central parts, due to higher levels of moisture levels in these parts of the cross-section. This is shown in figure 4.9 and 4.10.



Figure 4.9: Picture taken at axis 1 showing the western side of the bridge deck (Aas Jacobsen, 2013).

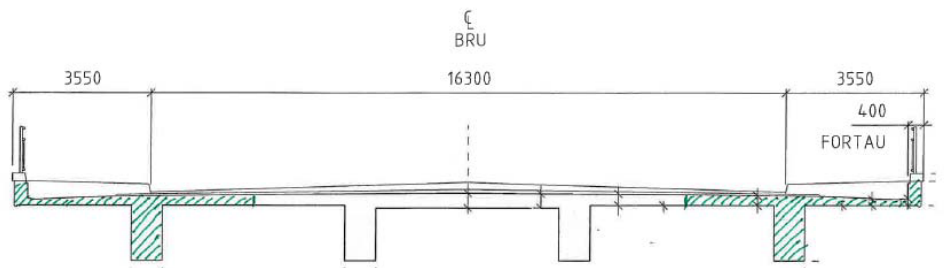


Figure 4.10: Cross- section of the bridge marked with the areas where the degree of Alkali- Silica reactions is assumed to be high (Aas Jacobsen, 2013).

In 2012 four 90 mm core tests were taken from the northern end of the bridge and delivered to Sintef for inspection (Aas Jacobsen, 2013).

- EB I V2: Beam 1 from west
- EB II V3: Beam 2 from west
- EB IV ϕ 4: Eastern beam (Beam 4 from west)
- EK1: Western edge beam (kantdrager)

Inspection of core tests was conducted with three methods:

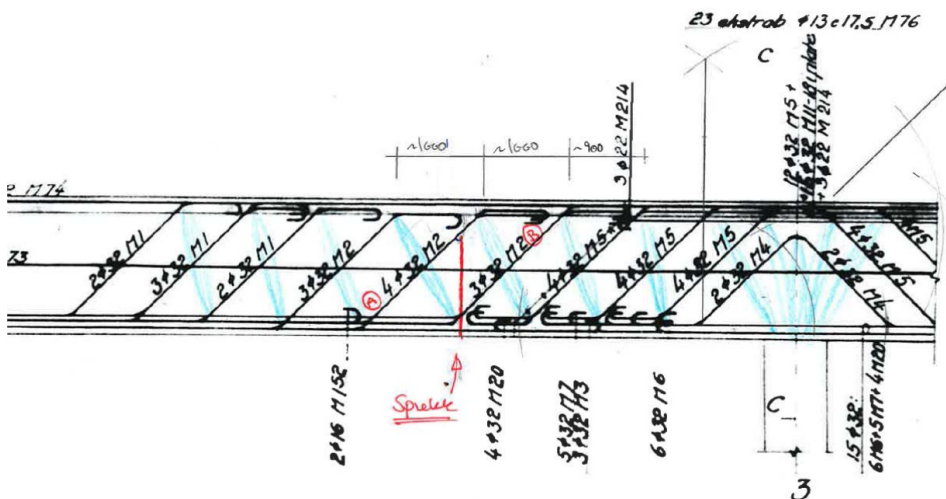
- Visual inspection of all tests:
- Macro analysis using UV light (EB I V2 and EB II V3)
- Micro analysis using a polarized microscope with UV- filter (EB I V2 and EB II V3)

Based on the visual inspections it was concluded that all core test showed some signs of Alkali- reaction. Core tests from the western beam (EB I V2) and western edge beam (EK1) had the clearest signs, while the other core tests showed signs of an early development of ASR. The more advanced analysis of the core tests (EB I V2 and EB II V3) supported the result from the visual inspection (Aas Jacobsen, 2013).

4.5.2 Conclusion from special investigation

Based on the assumption that the outer beams expand more than the central beam, Aas Jacobsen (2013) explains the vertical cracks occurring at the central beams with the fact that the central beams are strained as the outer beam expands more.

The reason why the most significant cracks appear at the zero moment spots, 4.5m from the columns is explained by the fact that the amount of (lower) reinforcement in these sections are designed to a minimum. As shown in figure 9.7, the cracks occur 4,5m from the columns where there is a limited amount of tensile reinforcement.



(Aas Jacobsen, 2013)

Figure 4.11: Reinforcement at inner beams supports, axis 2-8

4.6 Preventive actions on Elgeseter bridge

- 2003: Column in axis 7,8 and 9 were cut off and placed back into position (figure 4.12)
- 2003: Test project using carbon- fiber to cover columns in axis 2 established.
- 2013: Test project using carbon fiber strengthening on some of the inner beams where the most significant cracks appear (figure 4.13).
- 2014: New membrane and wearing course at driving lanes to prevent moisture.
- 2box: Moisture prevention of edge beams using hydrophobic impregnation.
- 2015: New membrane at pedestrian parts of the bridge.



Figure 4.12: Column top cut off and replaced



Figure 4.13: Test project using carbon fiber strengthening at inner beams. Glued to the beams with epoxy. Mechanical anchor at ends (Aas Jacobsen, 2015)

Chapter 5

Materials

5.1 Concrete

Based on the bridge drawings, the superstructure consists of $350\text{kg}/\text{m}^3$ cement, which is equal to C25 concrete. The concrete columns consist of $400\text{kg}/\text{m}^3$ of cement, which is equal to C30 concrete. As can be seen in table 5.1, the characteristic compression strength for C20 and C25 concrete are $16,8\text{ N}/\text{mm}^2$ and $19,6\text{ N}/\text{mm}^2$ respectively.

Table 5.1: Concrete strength. (Norwegian Public Roads Administration, 2014)

Byggeår	NS 427 (av 1939)	NS 427A (av 1962)		NS 3473 (av 1973 og senere)	
	Betong- kvalitet	Betong- kvalitet	σ_c (kg/cm^2)	Fasthets- klasse	f_{cn} (N/mm^2)
Før 1920	C-betong	B 200	40	C 15	11,2
1920-1945	B-betong	B 250	45	C 20	14,0
Etter 1945	A-betong	B 300	55	C 25	16,8
		B 350	60	C 30	19,6
		B 400	70	C 35	22,4
		B 450	80	C 40	25,2
				C 45	28,0

The design strength of the concrete is found by equation 5.1. According to NS 3473 2003, pt 10.4.3, the material safety factor γ_c in ULS is set to 1,4.

$$f_{cd} = \frac{f_{cn}}{\gamma_c} \quad (5.1)$$

To calculate the short term E- modulus, equation 5.2 was used. The characteristic cylindrical compression strength f_{cck} are $25 N/mm^2$ for the C25 concrete and $30 N/mm^2$ for the C30 concrete.

$$E_c = 9500(N/mm^2)^{0.7} \cdot (f_{cck})^{0.3} \quad (5.2)$$

Equation 5.3 gives an estimation of the long-term E- modulus. The concrete creep coefficient φ was assumed to be equal to 2.

$$E_{c.long} = \frac{E_c}{1 + \varphi} \quad (5.3)$$

Table 5.2: Concrete properties

	Bridge deck (C25)	Columns (C30)
f_{cn} [N/mm^2]	16,8	19,6
f_{cd} [N/mm^2]	$\frac{16,8}{1,4} = 12$	$\frac{19,6}{1,4} = 14$
f_{tk} [N/mm^2]	2,10	2,35
f_{td} [N/mm^2]	$\frac{2,10}{1,4} = 1,5$	$\frac{2,35}{1,4} = 1,68$
f_{cck} [N/mm^2]	25	30
E_c [N/mm^2]	$9500 \cdot 25^{0.3} = 24952$	$9500 \cdot 30^{0.3} = 26354$
$E_{c.long}$ [N/mm^2]	8317	8785

5.2 Reinforcement

According to the bridge drawings, most of the reinforcement consists of S32, classified as steel quality *St. 52*. The rest of the reinforcement is classified as *St. 37*. According to R412, annex 1, the characteristic yield strength of *St. 37* is $230 N/mm^2$ (Norwegian Public Roads Administration, 2014). Reinforcement of quality *St. 52* is however not tabulated in R412. The report from Aas Jacobsen (2013) predicts the characteristic yield strength of *St. 52* to be $340 N/mm^2$.

The design yield strength is found by equation 5.4. As the bridge was built after 1920, the material safety factor γ_s is set to 1,25 (Norwegian Public Roads Administration, 2014).

$$f_{yd} = \frac{f_{yk}}{\gamma_s} \quad (5.4)$$

The design yield strength f_{yd} for the *St. 37* and *St.52* reinforcement are then $184 N/mm^2$ and $272 N/mm^2$, respectively.

According to NS3473 2003 point 11.3.6, the ultimate reinforcement strain ε_{su} is set to 10 ‰.

Table 5.3: Reinforcement properties

	St 37 (ϕ_{16} and ϕ_{22} bars)	St 52 (ϕ_{32} bars)
f_{yk} [N/mm^2]	230	340
f_{yd} [N/mm^2]	$\frac{230}{1,25} = 184$	$\frac{340}{1,25} = 272$
E_s [N/mm^2]	200 000	
ε_{su}	10 ‰ = 0.010	
$\varepsilon_{yd} = \frac{f_{yd}}{E_s}$	$\frac{184}{200000} = 0.00092$	$\frac{272}{200000} = 0.00137$

Chapter 6

Loads

Norwegian Public Roads Administration (2014) handbook R412 chapter 2.3 classify loads in relation to probability of occurring and consequences. The loads are divided into four categories: Permanent-, variable-, deformation- and accidental loads.

6.1 Permanent loads

Permanent loads are loads considered to be more or less constant. Permanent loads involve dead load of construction and permanent equipment, outside water pressure and soil pressure. The weight of the different materials are found in Handbook R412, section 4.1.1 Permanent loads which are included in the analysis are:

- Deadload of reinforced concrete: $25\text{kN}/\text{m}^3$
- Deadload of asphalt layer: $25\text{kN}/\text{m}^3$

During the special investigation carried out by Aas Jacobsen (2013), the wearing course layer was found to be up to 30cm along the center line of the bridge. In 2014, the old wearing course was replaced with a new, thinner layer, as advertised by the report. The new wearing course consists of a 12mm membrane, 25mm adherent layer, and a 40mm asphalt layer. By assuming that the characteristic weight of all these layers is $25\text{kN}/\text{m}^3$, the wearing course weight is estimated to be. $25\text{kN}/\text{m}^3 \cdot 0,077\text{m} = 1,925\text{kN}/\text{m}^2$.

6.1.1 Minimum wearing course load

According to handbook N400, section 5.2.2.2 the minimum load from the wearing course is set to $3,5/\text{m}^2$ for bridge span smaller than 50m (Vegvesen, 2015). As this load is larger

than the calculated wearing course load, the minimum wearing course load is used.

6.2 Variable loads

Variable loads are considered to be varying during the lifetime of the construction. Variable loads involve traffic load, environmental load, and bumps/ anchoring loads from ferries. Variable loads which are included in the analysis is:

- Traffic load
- Wind load
- Temperature load

On road bridges, snow load is not considered to co-occur with traffic load (handbook R412, paragraph 5.1), and is therefore neglected.

6.2.1 Traffic load

Traffic loads include loads from vehicles, cyclists, and pedestrians on driving lane, hard shoulder, central reservation, cycle track, and sidewalk. Traffic loads from vehicles, lorries and special vehicles give rise to vertical, horizontal, static and dynamic forces.

Classification of traffic loads on existing bridges is defined in handbook R412 chapter 3. Normally, bridges are classified in relation to tabulated bridge classes.

Vertical traffic load

Each bridge class consists of six load model(LM): Wheel LM, axle LM, bogie LM, triple bogie LM, Vehicle LM, and lorry LM, as shown in figure 6.1. To assess the capacity of each section, the load models are applied in the most unfavorable position in the longitudinal and transverse direction (within the carriageway). When controlling the capacity of the different sections, all the load models have to be evaluated separately.

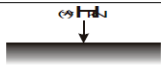

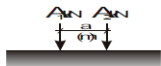
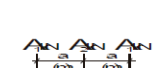
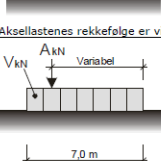
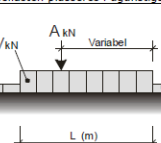
Lasttype	Lastkonfigurasjon	Bruksklasser					
			Bk 10/60	Bk 10/50	Bk T8/40	Bk 8/32	Bk 6/28
	Aksellast	kN	100		80	80	60
	Totalvekt	kN	600	500	400	320	280
Hjullast		H	80		56	56	42
Aksellast		A	160		112	112	84
Boggilast		A ₁	65		40	40	30
		A ₂	160		112	112	84
		a	1,3		1,3	1,3	1,3
Trippelboggilast		A ₁	70		60	50	40
		A ₂	140		84	84	56
		a	1,3		1,3	1,3	1,3
Kjøretøylast		A	40		32	32	24
		V	300		280	220	180
Vognlast		A	40		32	32	24
		V	600	500	400	320	280
		L	18,0	16,0	16,0	16,0	16,0
		p	6		6	6	6

Figure 6.1: Load models in relation to bridge class. Norwegian Public Roads Administration (2014)

According to handbook R412, the worst load model for small bridges will normally be achieved by axle LM, bogie LM or triple bogie LM, while larger bridge span will be limited to the vehicle LM or lorry LM.

Elgeseter bridge is classified as Bk10/50, which means that the tabulated loads connected to this bridge class are used. The lorry load model was found to be most critical for all sections. The lorry load model consists of an axle load (A), a total vehicle load (V) and an evenly distributed load (p), as shown in figure 6.2.1. The 40 kN axle load is placed in the most unfavorable position (within the 16m). The total lorry load of 500 kN is distributed along 16 meter, which results in an evenly distributed load with the value 31,25kN/m. The even distributed load $p=6\text{kN/m}$ is applied behind and in front of the vehicle load (V).

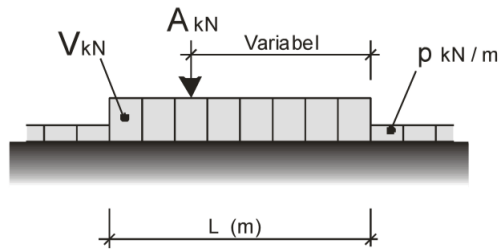


Figure 6.2: Lorry load model

The width of the of the different loads in the lorry model is shown in figure 6.3. The width of the axle and vehicle load is 3m, while the even distributed load is distributed within 2m.

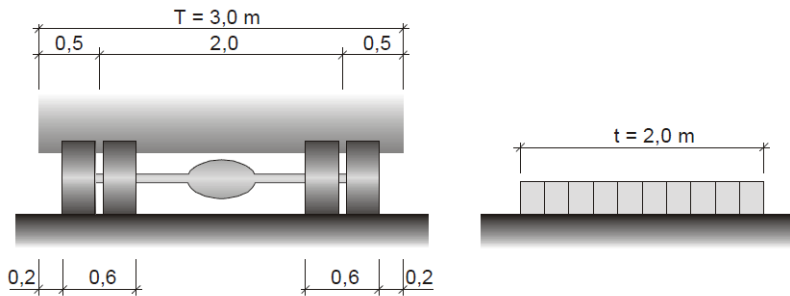


Figure 6.3: Width of the loads

According to handbook R412, paragraph 3.2.2, the maximal number of notional lanes loaded with axle loads, vehicle loads or lorry loads are set to two. The rest of the notional lanes are loaded with an evenly distributed load $p=6\text{kN/m}$.

Horizontal traffic load

Horizontal traffic loads are defined in Handbook R412, chapter 3.2.3. Horizontal traffic loads appear as braking and acceleration forces along with centrifugal and transverse forces. As the bridge is fixed to the abutment in axis 1, it was chosen to neglect the effect of horizontal traffic load in the longitudinal direction.

6.2.2 Wind load

Wind load on the construction is decided by handbook N400 and NS-EN 1991-1-4. According to handbook N400, chapter 5.4.3, the wind load on constructions depends on the wind class:

- Wind class I: Bridge construction with negligible to dynamic wind load.
- Wind class II: Bridge constructions dynamic response from wind load cannot be neglected.
- Wind class III: Bridge constructions sensitive to dynamic wind load.

Elgeseter bridge is a concrete slab beam bridge. This bridge type belong to wind class I. Bridge constructions has to be controlled for two separate cases: Wind load with- and without simultaneously acting traffic load. The two load-cases gives different wind loads due to different load area and the assumption that the maximal wind load will not coincide with traffic load. The detailed calculations of the wind load are found in appendix A.

According to table NA.4(901.1) in NS-EN 1991-1-5, the reference wind velocity in Trondheim is:

$$v_{b,0} = 26m/s$$

To transform the wind velocity to an evenly distributed load on the bridge, the basis wind velocity has to be defined. According to NA.4.2(2)P, the reference wind velocity is multiplied with four factors which take into account wind direction (c_{dir}), season variations (c_{season}), altitude ($c_{altitude}$) and the probability reference period (c_{prob}). As the reference period is set to 50 years, c_{prob} is equal to 1,0. All the other factors is also found to be 1,0, which means that the basic wind speed velocity is:

$$v_b = v_{b,0} * c_{dir} * c_{season} * c_{altitude} * c_{prob} = 26m/s$$

The mean wind speed is calculation by taking into account the roughness and orography at the bridge localization. The orography factor ($C_o(z)$) is set to 1, while the roughness factor ($C_r(z)$) depends on the bridge maximal height above the terrain ($z=16,5$), and the terrain roughness category at the localization. To be conservative, category I: *Near coastal places with aggressive sea* was selected. The factors used to calculate the roughness factor are given in table NA.4.1 in NS-EN 1991-1-4. According to NA.4.3.3(901.2), the mean wind velocity is calculated to be:

$$v_m = C_r(z) * C_o(Z) * v_b = 32.75m/s$$

The peak velocity pressure is calculated according to NA.4.5(1):

$$q_{p,notraffic} = \frac{1}{2}\rho*v_m(z)^2 * (1 + 2k_p * I_v(z)) = 1303Pa$$

To find the distributed forces in the different directions acting on the bridge, the force coefficients are calculated according to NS-EN 1991-1-4, chapter 8. The axis system for calculating the resulting forces on the bridge is shown in figure 6.4.

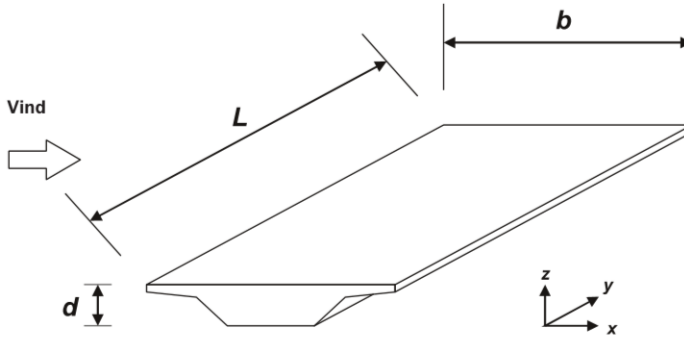


Figure 6.4: Axis system for wind loads - m ha kilde her

According to point 8.3.2(1) in NS-EN 1991-1-4, the simplified method for calculating wind forces can be used if dynamic response calculations are to be neglected. Since the bridge is in wind class I, the simplified method is used. This gives the following equations for calculating the resulting wind forces:

$$F_{wx} = \frac{1}{2}\rho*v_b^2 * C_x * A_{ref,x} \quad (NS-EN1991-1-4; pt.8.3.2(1))$$

$$F_{wy} = 0.25 * F_{wx} \quad (NS-EN1991-1-4; pt.NA.8.3.4(1))$$

$$F_{wz} = \frac{1}{2}\rho*v_b^2 * C_z * A_{ref,z} \quad (NS-EN1991-1-4; pt.8.3.3)$$

ρ represents the mass density of the air. The wind load factor C is calculated by multiplying the exposure factor c_e and the force factor c_f . The exposure factor is found to be $c_e = \frac{q_{p,notraffic}}{q_b} = 3.085$, according to NS-EN 1991-1-4, pt 4.5(1). The force factor in the x-direction (c_{fx}) is found to be 1,3 according to pt 8.3.1 in NS-EN 1991-1-4. According to NA. 8.3.(1) in NS-EN 1991-1-4, the force factor in the z-direction c_{fz} is set to +0,9. According to NS- EN 1991-1-5, pt 8.3.3(5), the wind force eccentricity acting in the z-direction is set to $e = \frac{b}{4}$ (from center line of the bridge). The reference area is set to 1 to get the even distributed load. The result of the wind calculations without simultaneous traffic load is shown in table 6.1.

Table 6.1: Wind load without simultaneously acting traffic load

Wind load direction	Even distributed wind load without simultaneously traffic load
x	1,694 kN/m ²
y	0,423 kN/m ²
z	+ - 1,173 kN/m ²

In the event of simultaneously acting wind- and traffic load, the "throw wind speed" is set to 35m/s, as defined in Handbook N400, chapter 5.4.3.3. The wind speed pressure is decided according to NS-EN 1991-1-4 NA.4.5(1):

$$q_{p.traffic} = \frac{1}{2} * \rho * (35\text{m/s})^2 = 766\text{Pa}$$

The resulting wind forces $F_{wx.t}$, $F_{wy.t}$ and $F_{wz.t}$ is calculated with the same equations as given in chapter 6.2.2. The new exposure factor $c_{e.t} = \frac{q_{p.traffic}}{q_b} = 1.812$. The resulting wind forces acting simultaneously with traffic load is shown in table 6.2.

Table 6.2: Wind load acting simultaneously with traffic load

Wind load direction	Even distributed wind load acting simultaneously with traffic load
x	0,995 kN/m ²
y	0,25 kN/m ²
z	+ - 0,689 kN/m ²

6.2.3 Temperature load

Temperature load is a variable environmental load. Temperature influences is shortly described in Handbook N400, chapter 5.4.8. The method for calculating temperature-changes in bridges is done according to NS-EN 1991-1-5, chapter 6.

Different super structures divided in three main classes:

- Type 1: Steel bridge
- Type 2: Coherence bridge (Steel/ concrete)
- Type 3: Concrete bridge

Elgeseter bridge is classified according to NA.6.1.(1) as type 3: concrete slab beam bridge. Minimum and maximum shadow temperature based on geographical terms are given in figure NA.A1 and NA.A2. The design values are based on extrema temperatures in a 50 year period. Elgeseter bridge in Trondheim has the following design temperatures.

$$T_{max} = 36^{\circ}C$$

$$T_{min} = -30^{\circ}C$$

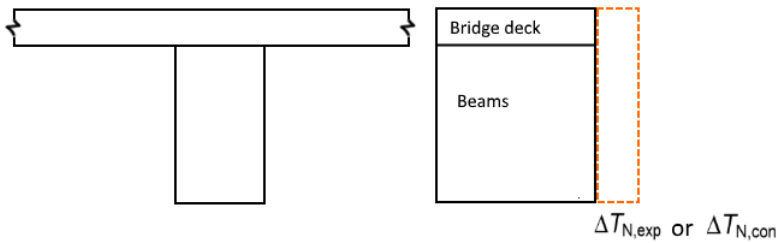


Figure 6.5: Uniform temperature components

The uniform temperature components depend on the minimum and maximum temperature which a bridge will achieve. Elgeseter bridge is statically undetermined with columns restraining the elongation which means that this load effect has to be considered. To calculate uniform temperature loading on the bridge, the equations in figure NA 6.1 for type 3 bridge are used to calculate the min- and maximum temperature in the bridge.

$$T_{e,max} = T_{max} - 3^{\circ}C = 36^{\circ}C - 3^{\circ}C = 33^{\circ}C$$

$$T_{e,min} = T_{min} + 8^{\circ}C = -30^{\circ}C + 8^{\circ}C = -22^{\circ}C$$

The maximal contraction- and expansion interval are dependent on the initial temperature T_0 . According to NA. A.1, the initial temperature T_0 is set to $10^{\circ}C$. This gives the following contraction- and expansion values:

$$\Delta T_{N,con} = T_0 - T_{e,min} = 10^{\circ}C - (-22^{\circ}C) = -32^{\circ}C$$

$$\Delta T_{N,exp} = T_{e,max} - T_0 = 33^{\circ}C - 10^{\circ}C = 23^{\circ}C$$

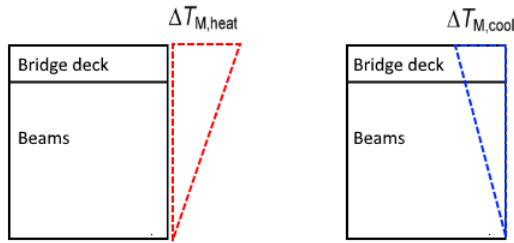


Figure 6.6: Linear vertical temperature difference components

Temperature differences between the lower and upper side of the cross-section have to be considered as it introduces new forces and moment to the statically undetermined system. These temperature differences are normally connected to daily temperature variations. This effect is covered by two different methods in chapter 6.1.4.

- Approach 1: Linear vertical component
- Approach 2: Vertical temperature with non- linear effects

In this thesis, the linear solution model covered in chapter 6.1.4.1 is used. Table NA. 6.1 gives values of linear temperature difference component for different types of bridge decks. The values in the table is based on bridge decks with a 50mm thick asphalt deck layer. If the bridge deck has an asphalt deck larger than 50mm, the vertical temperature difference has to be multiplied by a reduction factor k_{sur} found in table NA. 6.2. According to the bridge drawings from 2014, when the wearing course (membrane, adherent layer, asphalt) was replaced, the thickness of the wearing course was found to be 77mm, as shown in figure 6.8. By interpolating between 50mm and 100mm, the $k_{sur,heat}$ reduction factor was found to be 0,85. This gives the following estimation of the vertical temperature difference component.

$$\begin{aligned}
 k_{sur,heat} &= 0.85 \\
 k_{sur,cool} &= 1.0 \\
 \Delta T_{M,heat} &= 15^{\circ}C * k_{sur,heat} = 12,75^{\circ}C \\
 \Delta T_{M,cool} &= -8^{\circ}C * k_{sur,cool} = -8^{\circ}C
 \end{aligned}$$

$\Delta T_{M,heat}$ represent the temperature difference when the top side is warmer than the bottom, while $\Delta T_{M,cool}$ represent the temperature difference in the case when the bottom side is warmer than the top.

Horizontal temperature differences

In special cases where one side of the bridge is significantly more exposed to radiation from the sun, horizontal temperature effects should be included. As this is not the case in Elgeseter, it was chosen to only look at vertical temperature difference effects, as proposed in point NS-EN 1991-1-5, point 6.1.3.4(1).

Simultaneity of uniform and vertical temperature component

To describe the final temperature loading, it is necessary to take into account both the uniform temperature component (season variations) and vertical temperature component (daily variations). The worst combinations of the two temperature components are found by one of the following equation:

$$\Delta T_{M,heat} \text{ (or } \Delta T_{M,cool}) + \omega_N * \Delta T_{N,exp} \text{ (or } \Delta T_{N,con})$$

or

$$\omega_M * \Delta T_{M,heat} \text{ (or } \Delta T_{M,cool}) + \Delta T_{N,exp} \text{ (or } \Delta T_{N,con})$$

The combination factors ω_N and ω_M are set to 0,35 and 0,75 respectively, according to NA 6.1.5(1). The two equations can be combined in four different ways. This gives a total of eight different temperature combinations, as shown in table 6.3.

Table 6.3: Combinations of uniform and vertical temperature components

Combinations	$\Delta T_{M,heat}$	$\Delta T_{M,cool}$	$\Delta T_{N,exp}$	$T_{N,con}$
T1	1,0		0,35	
T2	0,75		1,0	
T3	1,0			0,35
T4	0,75			1,0
T5		1,0	0,35	
T6		0,75	1,0	
T7		1,0		0,35
T8		0,75		1,0

Knowing that the bridge has elongated up to 200mm from the alkali-reaction, only load combinations T1, T2, T5, T6. The final load combinations from temperature loading are shown in table 6.4 for combination T1 and T2.

Table 6.4: Final temperature combinations

Comb	$\Delta T_{M,heat}$	$\Delta T_{M,cool}$	$\Delta T_{N,exp}$	$\Delta T_{N,con}$
T1	$1,0 * 12,75^{\circ}C = 12,75^{\circ}C$		$0,35 * 23^{\circ}C = 8,05^{\circ}C$	
T2	$0,75 * 12,75^{\circ}C = 9,56^{\circ}C$		$1,0 * 23^{\circ}C = 23^{\circ}C$	
T5		$1,0 * -8^{\circ}C = -8^{\circ}C$	$0,35 * 23^{\circ}C = 8,05^{\circ}C$	
T6		$0,75 * -8^{\circ}C = -6^{\circ}C$	$1,0 * 23^{\circ}C = 23^{\circ}C$	

6.3 Deformation load - Alkali-Silika reaction (ASR)

The alkali-silica load is categorized as a deforming load. As revealed in section ASR contributes to inner and external load effects on the bridge. In the capacity control of the different section, only the external load effect from ASR was included.

As the bridge is statically undetermined with columns restraining the elongation, both uniform and different expansion over the height of the cross-section will give outer load effects on the bridge.

6.4 Ultimate limit state

To assess the limit state capacity, Handbook R412 annex 1 introduces two sets of load combinations; a and b , as shown in table 6.5. Each section of the construction has to be controlled towards the most unfavorable load combination. Q_1 represent the characteristic value of the most unfavorable load action for the given section. Q_n represents the characteristic value of the other variable loads that give the most unfavorable action in the given section.

Table 6.5: Ultimate limit state load combination according to Handbook R412

Load combination	Permanent loads, P		Deformational loads, D	Variable loads Q
	Soil pressure, J	Other		
a	1,0	1,15	1	$\gamma_1 \times Q_1$
b	1,0	1,0	1,0	$\gamma_2 \times Q_1 + 0,8 \sum Q_n$

Load combination a

$\gamma_1 = 1,3$ (two lorries)

Load combination b

$\gamma_1 = 1,2$

6.5 Vertical line load on internal T-beams

In this thesis, it was chosen to assess the capacity of the internal T-beams, as these beams have to carry most of the traffic load. As the bridge plate has different height over the width, it was decided to include all forces acting within the width of 5500mm, when calculating the line load on the internal T-beams. This is a conservative assumption: Looking at the cross-section of the bridge (figure 6.7), the plate is cantilevered at the free side of the external beams. This contributes to reduced line load (from dead load) on the inner T-beams.

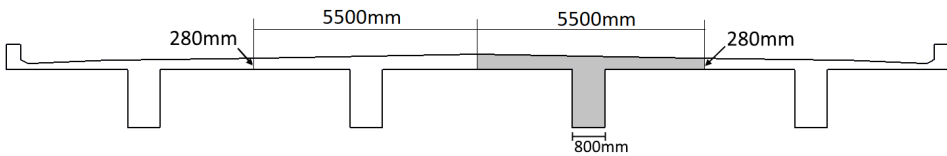


Figure 6.7: T- beam simplification

6.5.1 Dead load

Figure 6.8 shows the dimension of the different materials the inner T-beams has to carry.

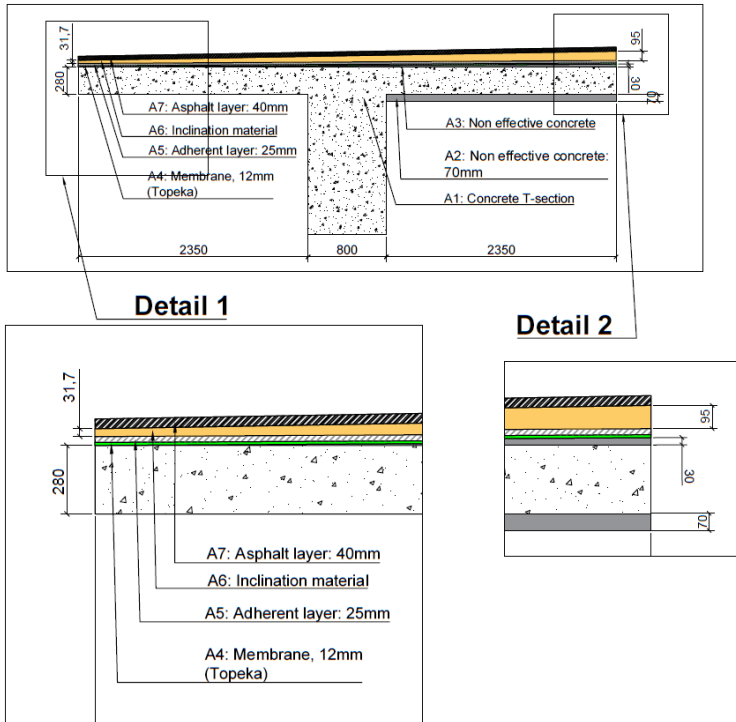


Figure 6.8: T-beam materials

T- section (A1)

$$g_{A1} = (0,8m * 1,43m + 0,28 * 5,5m) * 25kN/m^3 = 67,1kN/m$$

Non effective concrete (A2, A3))

$$g_{A2} = 0,07m * 2,35m * 25kN/m^3 = 4,1 kN/m$$

$$g_{A3} = \frac{0,07m+0m}{2} * 5,5m * 25kN/m^3 = 2,1 kN/m$$

Wearing course (A4,A5,A7)

As revealed in section 6.1.1, the weight of the wearing course (membrane, adherent layer and asphalt) is set to $3,5\text{kN}/\text{m}^2$.

$$g_{wc} = 3,5\text{kN}/\text{m}^2 * 5,5\text{m} = 19,3\text{ kN}/\text{m}$$

Inclination (A6)

$$g_{A6} = \frac{0,095\text{m}+0,0317\text{m}}{2} * 5,5\text{m} * 25\text{kN}/\text{m}^3 = 8,7\text{kN}/\text{m}$$

Total dead load

$$g_c = g_{A1} + g_{A2} + g_{A3} + g_{wc} + g_{A6} = 101,3\text{kN}/\text{m}$$

6.5.2 Traffic load

As revealed in section 6.2.1, the lorry load model was found to be the most unfavorable load combination considering maximal shear and moment. The lorry load model is placed in the two notional lanes over the beam, as shown in figure 6.9.

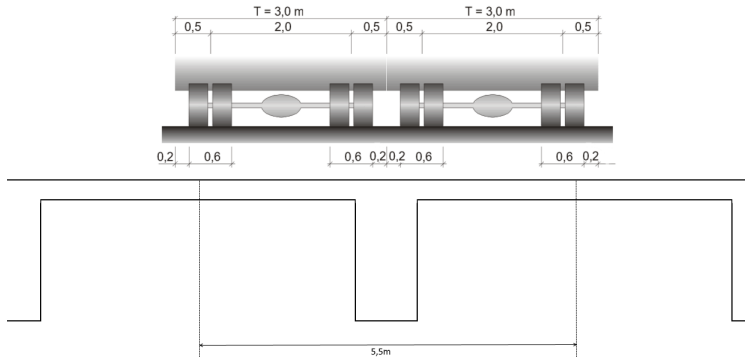


Figure 6.9: Worst load case above internal T-beam.

To calculate the line load from the two notional lanes on the most loaded inner beam, the axle load (A) and the vehicle load (V) is multiplied with a factor = $\frac{5.5}{3\text{m}}$, while the distributed load (p) is multiplied with a factor = 2. This gives the following load, which is shown in table 6.6.

Table 6.6: Lorry model applied to T-beam

	Total load (V)	Axle load (A)	Even distributed load (p)
Lorry load model: - one notional lane	31,25 kN/m	40 kN	6 kN/m
Lorry load model - transferred to internal T-beam from two notional lanes.	57,3 kN/m	73,3 kN	12 kN/m

6.5.3 Wind load

As revealed in section 6.2.2, the eccentricity of the wind load acting in the vertical (z-direction) is set to $e = \frac{b}{4}$. To find the wind load on the most loaded T-beam, a triangular distributed wind load is applied to the bridge plate, as shown in figure 6.10. This gives an eccentricity of the load equal to $e = \frac{b}{3}$, which is assumed to be good enough to get an estimation of the wind load on the most loaded T-beam.

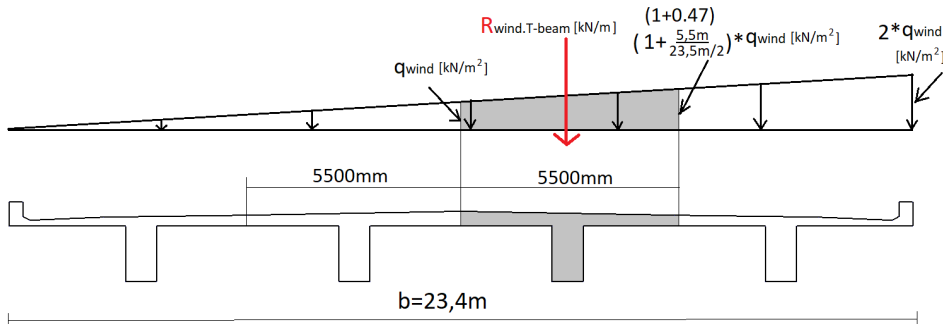


Figure 6.10: Wind load on most loaded T-beam

Wind load without simultaneously traffic load

As shown in table 6.1, the even distributed load in the z-direction was calculated to be $q_{wind.no.traffic} = (+-)1.173kN/m^2$.

The force resultant acting on the most loaded T-beam is calculated to be:

$$R_{wind.T-beam.no.traffic} = (+-)\left(\frac{1+(1+0,47)}{2}\right) * 1.173kN/m^2 * 5,5m = 7.9 kN/m$$

Simultaneity of wind- and traffic load

As shown in table 6.2, the even distributed load in the z- direction was calculated to be $q_{wind.with.traffic} = (+-)0,689kN/m^2$.

$$R_{wind.T-beam.with.traffic} = (+-)\left(\frac{1+(1+0,47)}{2}\right) * 0,689kN/m^2 * 5,5m = 4.5 kN/m$$

6.5.4 Temperature load

The temperature load $\Delta T_{N,exp} = 23^{\circ}C$, $\Delta T_{M,heat} = 12,75^{\circ}C$ and $\Delta T_{M,cool} = -8^{\circ}C$, derived in section 6.2.3 are applied to the T-beam cross-section in three different load sets in Robot Structural analysis, without including the temperature combination factors. The temperature load combination factors described in table 6.4 was then taken into account when calculating the worst load case for each section.

The effect of the temperature load regarding forces on the structure depends on the E-modulus of the T-beam. The uniform temperature component ($\Delta T_{N,exp}$) is due to season variations. As this is a long-term effect, it was decided to use the long-term E- modulus. As the vertical temperature difference component is a daily effect, it was decided to use the short-term E - modulus when considering this load effect.

6.5.5 ASR load

To quantify the outer load effect of ASR on the inner T- beam, it was decided to use a combination of load model 1 and 2, as shown in figure 6.11, over the whole length of the bridge. The magnitude of the load depends on the total elongation of the bridge, and the ratio between load model 1 and 2. The total elongation of the bridge in a stadium I linear elastic analysis is found by equation 6.1.

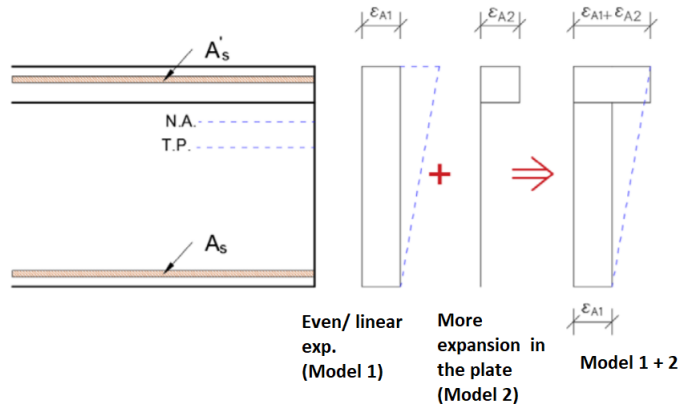


Figure 6.11: Assumed strain state from the expansion in the calculations. Modified figure (Norwegian Public Roads Administration, 2016)

$$\varepsilon_{T.section} = \frac{A_{plate} \cdot \varepsilon_{plate} + A_{beam} \cdot \varepsilon_{beam}}{A_{plate} + A_{beam}} \quad (6.1)$$

Assuming the expansion in the plate is twice as large as the expansion in the beam, equation 6.2 can be used to find the total elongation.

$$\varepsilon_{T.section} = \frac{(A_{plate} + 0,5 \cdot A_{beam}) \cdot \varepsilon_{plate}}{A_{plate} + A_{beam}} \quad (6.2)$$

The total elongation of the bridge is important to quantify the loads from Alkali- Silika expansion. Based on the measurements of the bridge elongation (section 4.4), the total elongation was set to 180mm, which is equal to 0,9‰. From equation, 6.2, the total expansion in the plate was found to be 1.144‰ when $\varepsilon_{T.section}$ was set to the target elongation = 0.9‰.

Calculated expansions in the beam and the plate

- $\varepsilon_{plate} = 1.144 \text{ ‰}$
- $\varepsilon_{beam} = \frac{1.144}{2} \text{ ‰} = 0.572 \text{ ‰}$

Uniform ASR expansion component, $\Delta ASR_{N,exp}$

The Uniform expansion component is equal to 0.9 ‰. Knowing that the temperature expansion coefficient in concrete, α_T is equal to $10^{-5}/K$, the uniform ASR expansion component can be modeled as an even temperature over the cross-section = $90^\circ C$.

Vertical ASR expansion component, $\Delta ASR_{M,plate}$

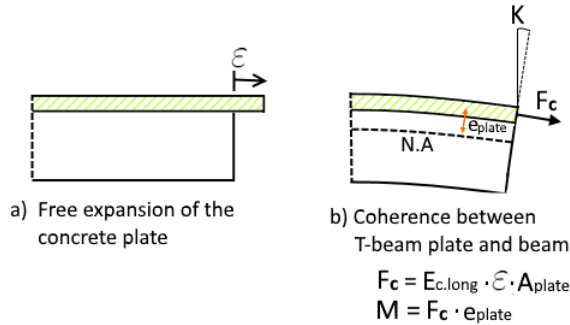


Figure 6.12: Calculation of curvature due to more expansion in the plate

When applying the vertical temperature difference component from ASR in Robot Structural Analysis, it has to be considered as a linear temperature- load over the cross-section. Knowing that the difference between the expansion in the plate and the beam is equal to $\Delta\varepsilon = 0.572 \text{ ‰}$, the curvature of the beam can be calculated with equation 6.3.

$$K = \frac{M}{E_{c.long} \cdot I_y} = \frac{E_{long} \cdot A_{plate} \cdot \Delta\varepsilon \cdot e_{plate}}{E_{c.long} \cdot I_y} \quad (6.3)$$

The total strain difference component is shown in figure 6.13a. This strain can be modeled in Robot with a vertical temperature difference component, $\Delta T = \frac{\Delta\varepsilon_K}{\alpha_T}$

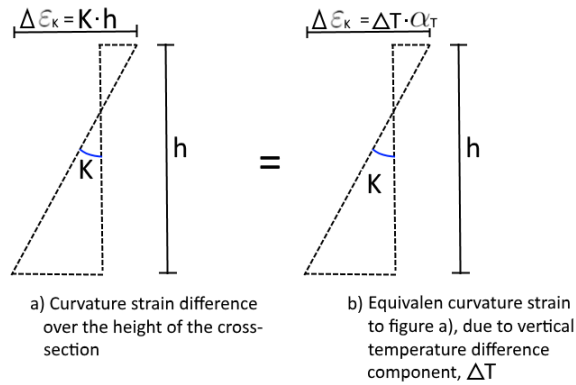


Figure 6.13: Equivalent curvature strain

Input variables

- $I_y = 6.84848 \cdot 10^{11} \text{ mm}^4$ (Appendix B)
- $e_{plate} = 364.4 \text{ mm}$ (Appendix B)
- $A_{plate} = 1540000 \text{ mm}^2$

By implementing the variables in equation 6.3, K was found to be $0.000468 / \text{m}$. This gives $\Delta T = \frac{K \cdot h}{\alpha_T} = 0.000468 / \text{m} \cdot 1.71 \text{ m} \cdot 10^{-5} / K = 80^\circ \text{C}$.

Analysis of loads in Robot - Longitudinal direction

7.1 Building the model

7.1.1 Dead load, traffic load, and wind load model

When considering the dead load, traffic load and wind load to the T- section, the bridge was modeled as fixed in axis 1 and roller supported in axis 2-10. This was done with the assumption that the bridge deck is much stiffer than the columns.

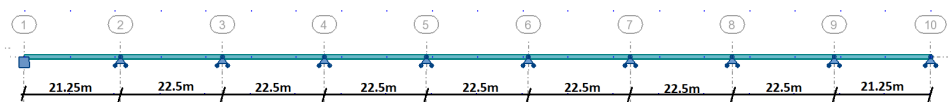


Figure 7.1: Traffic, dead load and wind load model in Robot structural analysis

7.1.2 ASR and temperature model

As the forces on the construction due to temperature load and ASR are dependent on the properties of the T-section and columns, a new model including the columns were made.

Geometry

The geometry of the T-section was applied as shown in figure 7.2. The E- modulus of the prescribed material C25 (T-beam) and C30 ($\phi 800$ mm columns) was modified according to the material properties derived in table 5.2. The long-term E-modulus was used when considering the uniform temperature component and ASR. The short-term E- modulus was used when calculating the load effects due to the vertical temperature difference component.

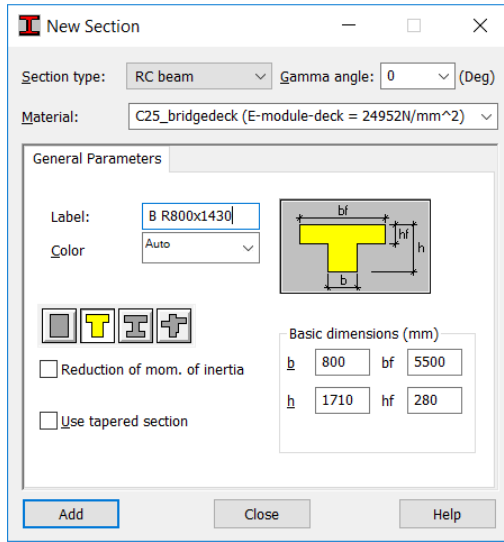


Figure 7.2: T-section, Elgeseter, Robot Structural Analysis

Boundary conditions

The T-section was fixed in axis 1 and roller supported in axis 10. All the columns was fixed to the ground. According to the bridge drawing, the column in axis 9 is hinged. As the rest of the columns (axis 2-8) are monolithically cast to the superstructure, the columns was fixed to the T-section.

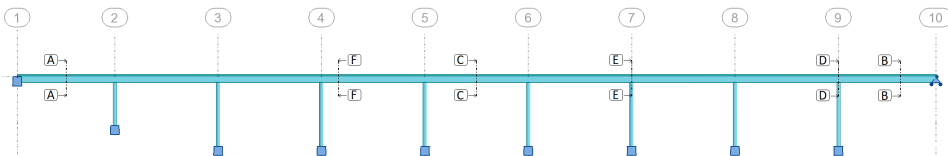


Figure 7.3: Model of Elgeseter bridge with columns in Robot Structural Analysis

7.2 Moment

7.2.1 Dead load

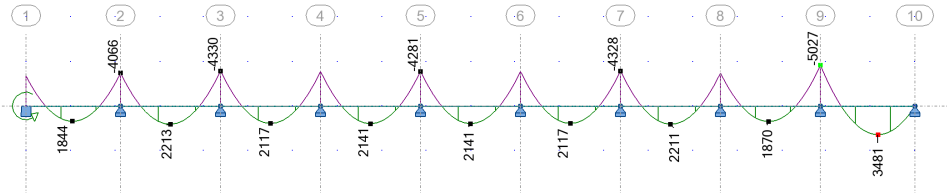


Figure 7.4: Dead load moment

7.2.2 Traffic load

The lorry load model was applied as a load-train, calculating the worst moment for each 0,2m. The position of the axle load was adapted to find the largest moments in each section.

Support moment

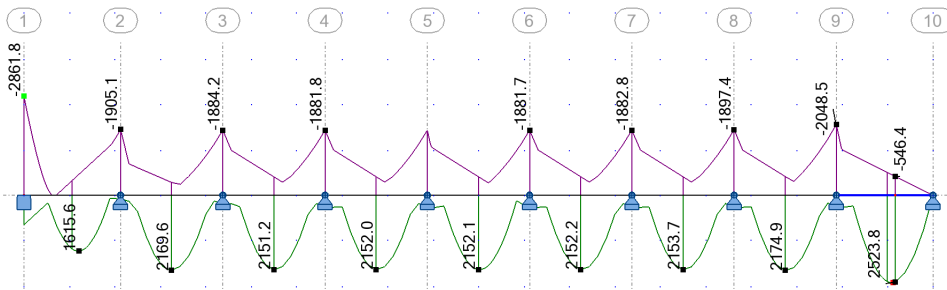


Figure 7.5: Lorry load model: Max support moments

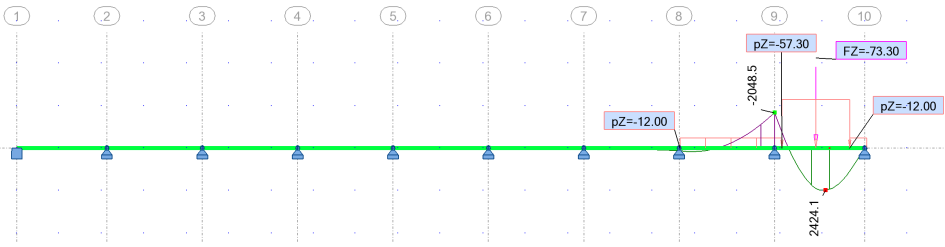


Figure 7.6: Lorry load model: Max moment support 9

Field moment

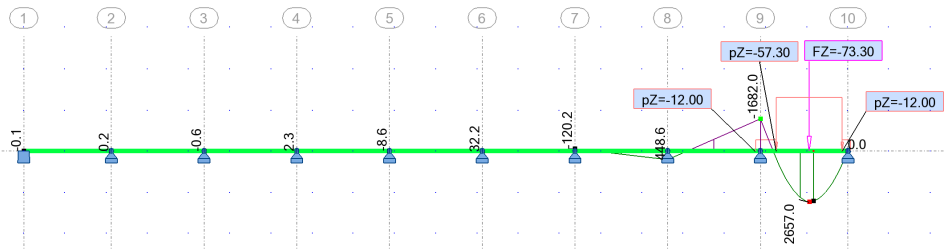


Figure 7.7: Lorry load model: Max field moment axis 9-10

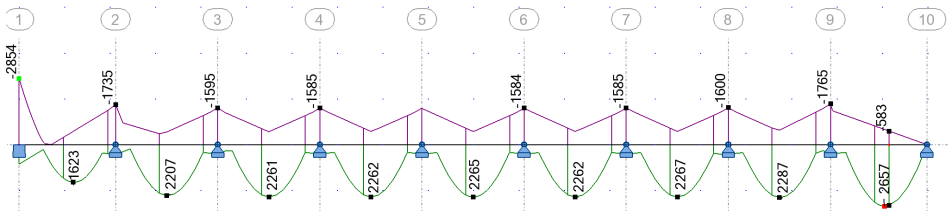


Figure 7.8: Lorry load model: Max field moments

7.2.3 Wind load

Support moment

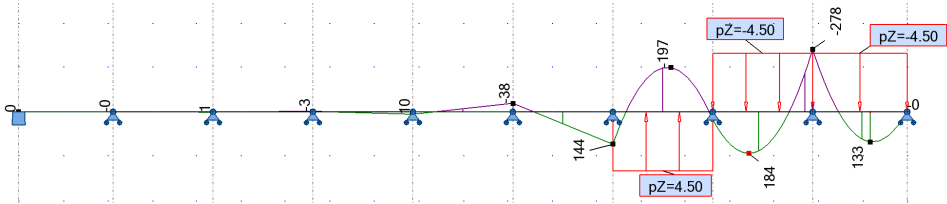


Figure 7.9: Max support-moment axis 9 from wind

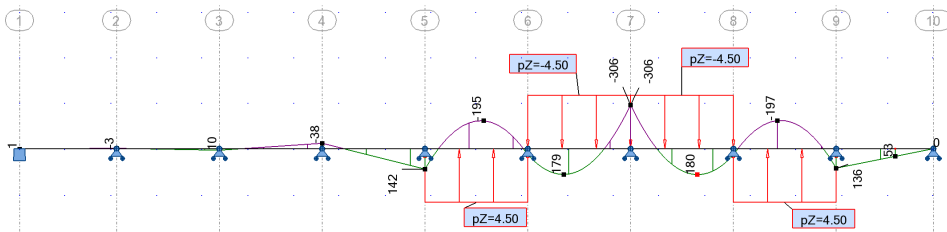


Figure 7.10: Max support-moment axis 7 from wind

Field moment

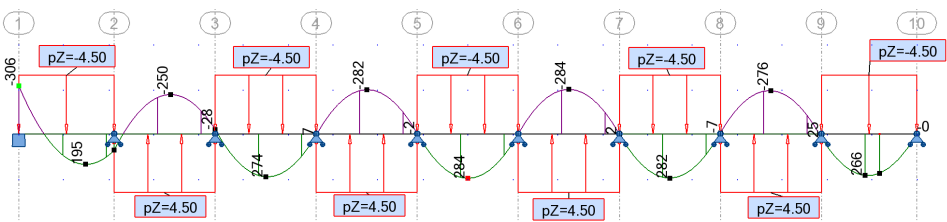


Figure 7.11: Max field moment

7.2.4 Temperature

Uniform temperature expansion component, $\Delta T_{N,exp}$

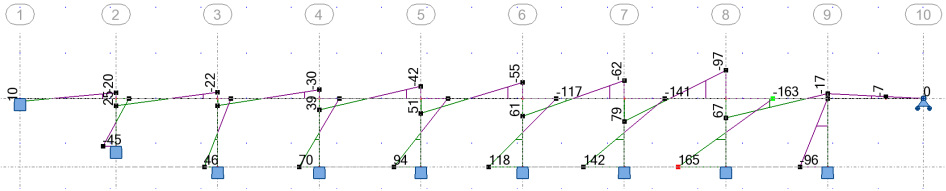


Figure 7.12: Moment diagram uniform expansion, $\Delta T_{N,exp}$

Vertical temperature difference components, $\Delta T_{M,heat}$ and $\Delta T_{M,cool}$

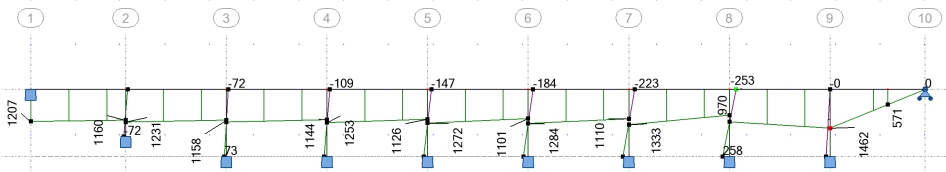


Figure 7.13: Moment diagram vertical heat component, $\Delta T_{M,heat}$

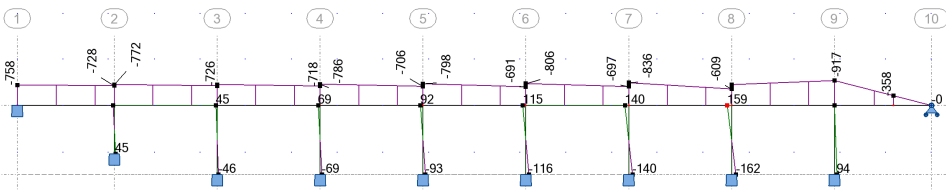


Figure 7.14: Moment diagram vertical cool component, $\Delta T_{M,cool}$

7.2.5 ASR expansion

Uniform ASR expansion component, $\Delta ASR_{N,exp}$

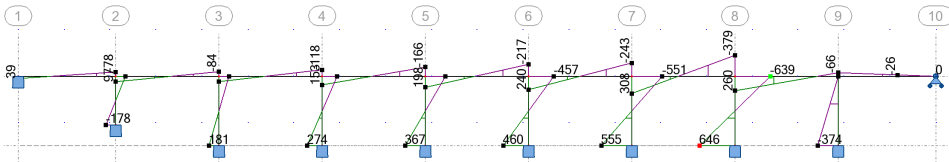


Figure 7.15: Moment diagram uniform ASR component, $\Delta ASR_{N,exp}$

Vertical ASR difference component, $\Delta ASR_{M,plate}$

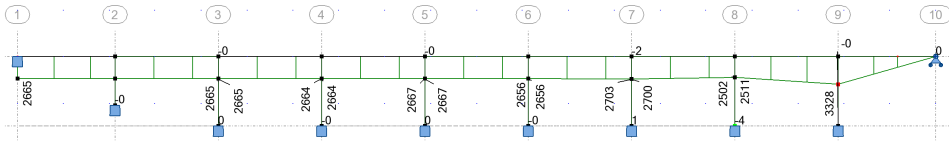


Figure 7.16: Moment diagram ASR difference component, $\Delta ASR_{M,plate}$

Total ASR expansion, $\Delta ASR_{N,exp} + \Delta ASR_{M,plate}$

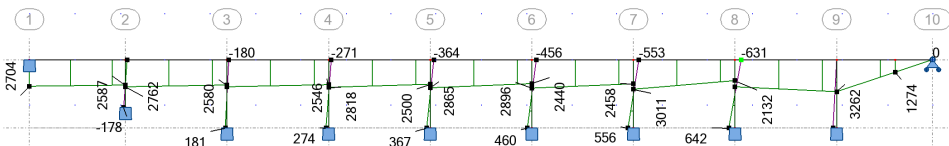


Figure 7.17: Total ASR expansion, $\Delta ASR_{N,exp} + \Delta ASR_{M,plate}$

7.3 Shear forces

7.3.1 Dead load

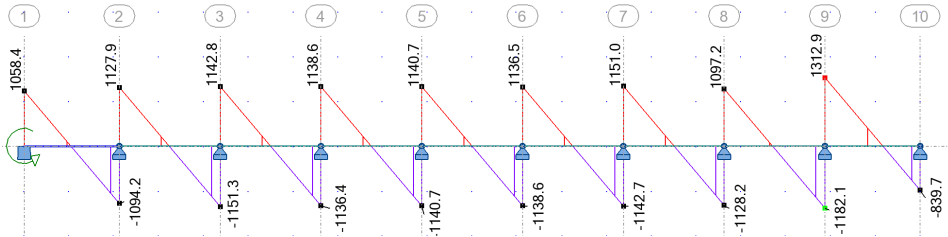


Figure 7.18: Shear force diagram dead load [kN]

7.3.2 Traffic load

The lorry load model was applied as a load-train, calculating the worst shear forces for each 0,2m section. Figure 7.19 shows the positioning of the loads giving the largest shear forces in axis 1-9. Figure 7.20 shows maximal shear forces in each section (axis 1-9).

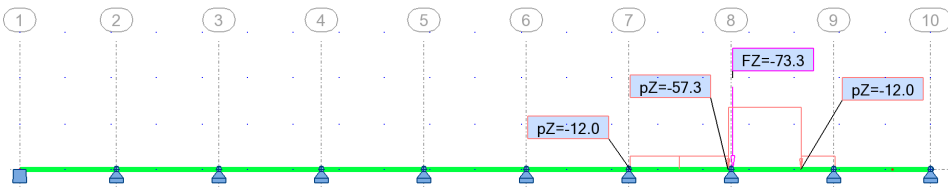


Figure 7.19: Lorry load model; Positioning of loads

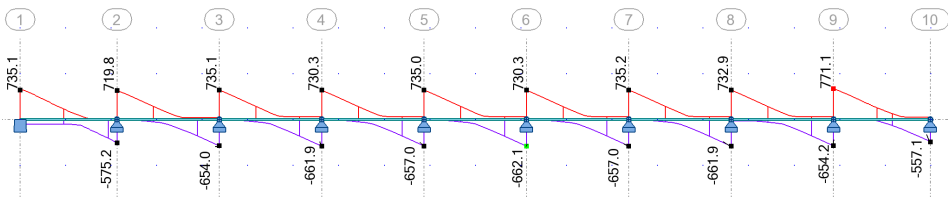


Figure 7.20: Max shear force lorry load model [kN]

Ultimate limit state - longitudinal direction

In this chapter, the ultimate limit state is controlled for the internal T-beams regarding shear and moment forces. The most critical forces achieved in each section from traffic load, dead load, wind load, temperature load and deformational load (ASR) were collected from the shear and moment diagrams in Robot. The forces were then multiplied with load factors according to R412 load combinations a and b, given in section 6.4. Control of the results from Robot by hand calculations are given in appendix D.

Figure 10.1 displays the sections that have been assessed regarding the moment capacity. The assessment of the shear capacity is limited to section D-D (axis 9). This section was selected as the analysis in Robot revealed that the most significant design shear forces appeared here.

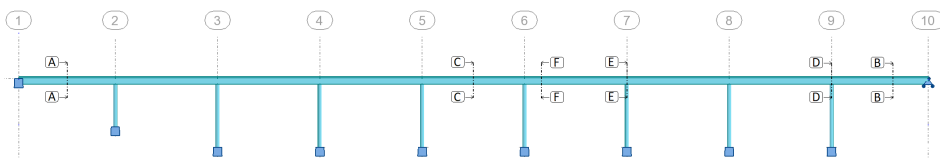


Figure 8.1: Illustration of sections

8.1 Section forces

8.1.1 Moment

Load combinations, not including deformational loads (ASR expansion)

Section A-A (First span)

Table 8.1: Load combinations section A-A [kNm]

Comb	Dead load	Traffic load	Wind	Temperature (Comb T1)	Total
a	$1844 \cdot 1,15 = 2121$	$1623 \cdot 1,3 = 2110$			4231
b	$1844 \cdot 1 = 1844$	$1623 \cdot 1,2 = 2213$	$195 \cdot 0,8 = 156$	$(\frac{1207+1160}{2}+0) \cdot 0,8 = 945$	4895

Section B-B (Last span)

Table 8.2: Load combinations section B-B [kNm]

Comb	Dead load	Traffic load	Wind	Temperature (Comb T1)	Total
a	$3481 \cdot 1,15 = 4003$	$2657 \cdot 1,3 = 3454$			7457
b	$3481 \cdot 1 = 3481$	$2657 \cdot 1,2 = 3188$	$266 \cdot 0,8 = 213$	$(571-19 \cdot 0,35) \cdot 0,8 = 451$	7334

Section C-C (span 4-5)

Table 8.3: Load combinations section C-C [kNm]

Comb	Dead load	Traffic load	Wind	Temperature (Comb T1)	Total
a	$2141 \cdot 1,15 = 2462$	$2265 \cdot 1,3 = 2944$			5407
b	$2141 \cdot 1 = 2141$	$2265 \cdot 1,2 = 2718$	$284 \cdot 0,8 = 227$	$(\frac{1253+1126}{2}+0) \cdot 0,8 = 952$	6038

Section D-D (Support 9)**Table 8.4:** Load combinations section D-D [kNm]

Comb	Dead load	Traffic load	Wind	Temperature (Comb T5)	Total
a	$-5027 \cdot 1,15$ = -5781	$-2048 \cdot 1,3$ = -2662			-8443
b	$-5027 \cdot 1 =$ -5027	$-2048 \cdot 1,2$ = -2457	$-278 \cdot 0,8$ = -222	$-(917 + 17 \cdot 0,35) \cdot 0,8$ = -738	-8410

Section E-E (Support 7)**Table 8.5:** Load combinations section E-E [kNm]

Comb	Dead load	Traffic load	Wind	Temperature (Comb T5)	Total
a	$-4328 \cdot 1,15$ = -4927	$-1882 \cdot 1,3$ = -2446			-7424
b	$-4328 \cdot 1 =$ -4328	$-1882 \cdot 1,2$ = -2258	$-306 \cdot 0,8$ = -245	$-(836 + 62 \cdot 0,35) \cdot 0,8$ = -686	-7517

Load combinations, including deformational loads (ASR expansion)

As moment from ASR expansion increase the field moment and reduce the support moments, it was decided to only evaluate the field sections and the original zero moment spots (section F-F) when including the additional moments from ASR expansion.

Field moments

As the sum of the field moments due to the vertical temperature heat component, $\Delta T_{M,heat}$ and the vertical ASR expansion component, $\Delta ASR_{M,plate}$ are limited by the zero moment spot capacities, it was decided to neglect R412 load combination b), when calculating the maximal field moments.

Table 8.6: R412 load combination a, including ASR moment, field sections A-A, B-B, C-C [kNm]

Section	R412 load combination a (without ASR moment)	Additional ASR moment	R412 load combination a (including ASR moment)
A-A	4231 kNm	2667 kNm	6898 kNm
B-B	7457 kNm	1300 kNm	8757 kNm
C-C	5407 kNm	2667 kNm	8074 kNm

Original zero moment sections, section F-F

Table 8.7: Section F-F

Section	R412 load combination b, (Only temperature, without ASR moment)	Additional ASR moment	R412 load combination b (temperature- + ASR- moment)
F-F	1300 kNm	2667	3967 kNm

8.1.2 Shear forces

Section D-D, support 9

R412 load combination a gave the largest shear forces in section D-D:

$$V_d = 1,15 \cdot V_g + 1,3 \cdot V_{TR} = 1,15 \cdot 1312 \text{ kN} + 1,3 \cdot 771 \text{ kN} = 2511 \text{ kN}$$

8.2 Section capacity

Moment- and shear capacities are calculated for the internal T-beams, shown in figure 8.3.

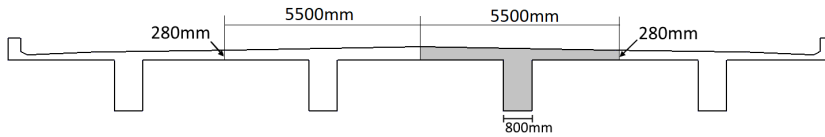


Figure 8.2: Internal T-beams

8.2.1 Moment capacity

The different sections that have been controlled are:

- Section A-A: First span (span between axis 1-2)
- Section B-B: Last span (span between axis 9-10)
- Section C-C: Internal spans (span between axis 5-6)
- Section D-D: Support axis 9
- Section E-E: Internal supports (Axis 3-8)
- Section F-F: Zero moment spots (Axis 1-9)

The method to assess the moment capacity are based on *Concrete Structures - Calculation and dimensioning according to Eurocode 2* (Sorensen, 2015). The calculations are done according to NS 3473 2003 (Norges Standardiseringsforbund, 2003).

In order to calculate the moment capacity of a cross-section, the effective flange width has to be calculated. According to NS 3473 2003, chapter 9.5, the effective flange width is given as the smallest of:

- Max flange width
- 10 % of the distance between the z-moment
- 8 times the thickness of the plate

Field moment capacity

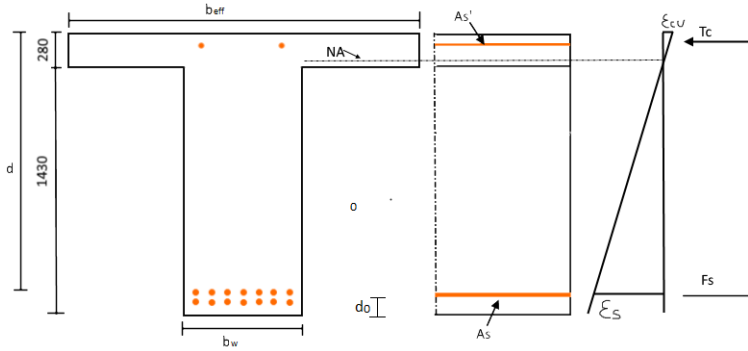


Figure 8.3: Flange in compression zone

In the span between two axes, the flange is on the compressed side of the cross-section. To calculate the field moment capacity, the cross-section has to be controlled to find out if it is under- or over-reinforced. This is done by calculating the amount of reinforcement in a balanced cross-section and compare with the amount of tensile reinforcement.

For under reinforced cross-sections, the height of the concrete compression zone is found by formula 8.1, assuming the ultimate concrete compression strain is reached before the ultimate reinforcement strain.

$$\alpha = \frac{A_s \cdot f_{sd}}{0,8 \cdot b_f \cdot d \cdot f_{cd}} \tag{8.1}$$

The flange has to be controlled to decide if it is thin or thick. The flange can be categorized as thick if the thickness of the flange $t_f \geq 0,8\alpha \cdot d$. If this equation is satisfied, the height of the compression zone is $t = \alpha \cdot d$.

The moment capacity of the compression zone can be found by equation 8.2.

$$M_d = 0,8 \cdot f_{cd} \cdot (1 - 0,4 \cdot \alpha) \cdot \alpha \cdot b_{eff} \cdot d^2 \tag{8.2}$$

Normally, the flange cross section is so wide that the height of the compression zone is small. This effect gives large strain ϵ_s in the reinforcement before the ultimate compression strain ϵ_{cu} in the concrete is reached. To find the reinforcement strain, equation 8.3 is used. As revealed in chapter 5.2, the maximal reinforcement strain is 10 %.

$$\varepsilon_s = \frac{1 - \alpha}{\alpha} \cdot \varepsilon_{cu} \quad (8.3)$$

By implementing equation 8.3, the reinforcement strain in all field sections was found to be too large by this method. This is a normal effect for T-sections with large flanges in compression, described in *Concrete Structures - Calculation and dimensioning according to Eurocode 2*, chapter 4.2.4 (Sorensen, 2015). If the max reinforcement strain criteria is reached, the compression strain $\varepsilon_c \leq \varepsilon_{cu}$, and the neutral axis will be moved down in the cross-section. In such cases, the moment capacity can be calculated by assuming constant concrete stress in the flange, as shown in figure 8.4. The compression force resultant will attack in the middle of the flange (Sorensen, 2015).

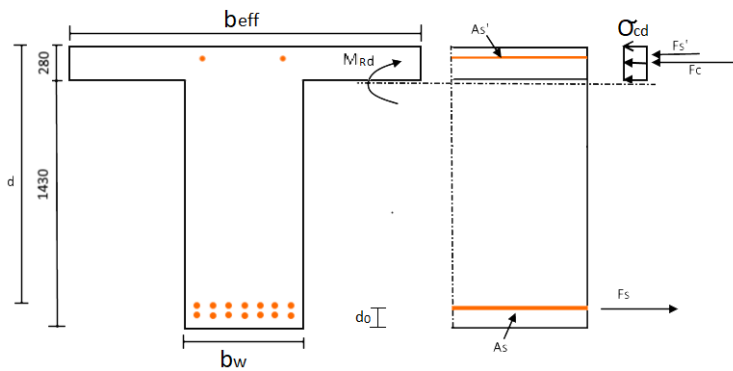


Figure 8.4: Flange in compression zone

The moment capacity of the section can be found by equation 8.4.

$$M_{Rd} = f_{yd} \cdot A_s \cdot \left(d - \frac{t_{flange}}{2}\right) \quad (8.4)$$

The compression stress in the flange has to be controlled by equation 8.5, to ensure $\sigma_{cd} \leq f_{cd}$.

$$\sigma_{cd} = \frac{M_{Rd}}{t_{flange} \cdot \left(d - \frac{t_{flange}}{2}\right)} \quad (8.5)$$

Summary of calculated field moment capacities, section A-A, B-B and C-C

The complete calculations of the field moment sections are found in appendix C. The key properties for each section are given in table 8.8. The design yield strength of the reinforcement is described in section 5.2. The small amount of compression reinforcement in the field sections were neglected since they were close to the neutral axis.

Table 8.8: Properties field sections (A-A, B-B, C-C)

Section	$A_{s,\phi32}$	$A_{s,\phi16}$	d_0	d	b_{eff}
A-A	15281 mm ²	0	133.4 mm	1577 mm	3775 mm
B-B	24127 mm ²	0	170.5 mm	1539.5 mm	4412.5 mm
C-C	16080 mm ²	402 mm ²	144.4 mm	1565.6 mm	3950 mm

The calculated moment capacity and flange compression stress are found in table 8.10. The concrete flange stress criteria $\sigma_{cd} \leq f_{cd}$ are satisfied for all the sections.

Table 8.9: Moment capacities field sections (A-A, B-B, C-C)

Section	M_{Rd} (equ 8.4)	σ_{cd} (equ 8.5)
A-A	5971 kNm	3.93 N/mm ²
B-B	9184 kNm	5.31 N/mm ²
C-C	6343 kNm	4.22 N/mm ²

Capacity zero moment- spots

Due to changes in the outer moment and strain due to the alkali reaction, cracks have been localized in the zero moment spots. As the amount of tensile reinforcement in the zero moment localizations are minimal compared to the concrete flange area, the neutral axis will be at the top side of the flange. This also means that the tensile reinforcement will reach its ultimate reinforcement strain ε_{su} before the ultimate compression strain capacity ε_{cu} . The moment capacity of the zero moment sections is found by calculating the moment in the strain state of the section when the reinforcement has reached its ultimate strain criteria ε_{su} . The concrete compression zone is assumed to have a linear elastic behavior and the reinforcement to take up all stress forces, as shown in figure 8.5. The reinforcement in the compression zone was neglected from the calculations. The dominant moment load at the zero moment localization is due to different ASR expansion over the height of the cross-section. As ASR expansion is a long time load, it was decided to use the long-term E-modulus of the concrete when calculating the capacity of the zero moment sections. Using the long-term E-modulus reduce the capacity of these sections, since the compression zone has to be increased to achieve axial equilibrium, reducing the moment lever arm, Z (equ 8.9).

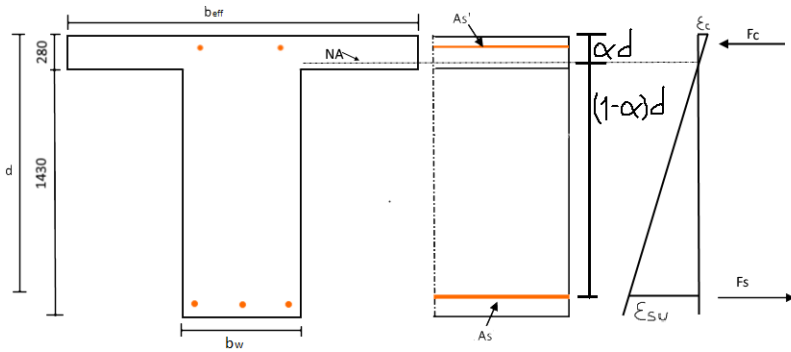


Figure 8.5: Moment capacity at zero moment spots

The α value, defining the neutral axis is found by demanding axial equilibrium in the section. This is fulfilled by guessing the α value until $F_c = F_s$. It has to be controlled that the height of the compression zone is less than the thickness of the flange plate. The concrete compression strain ε_c must also be controlled so that $\varepsilon_c \leq \varepsilon_{cu}$.

$$F_c = \left(\frac{1}{2} \cdot \varepsilon_c\right) \cdot E_c \cdot b_{eff} \cdot \alpha \cdot d \quad (8.6)$$

$$\varepsilon_c = \frac{\alpha \cdot d}{(1 - \alpha)d} \cdot \varepsilon_s \quad (8.7)$$

$$F_s = f_{yd} \cdot A_s \quad (8.8)$$

To calculate the moment capacity of the section, the internal lever arm Z has to be calculated. Knowing that the pressure resultant T_c attacks $\frac{1}{3} \cdot \alpha \cdot d$ from the top, the moment lever arm is calculated by equation 8.9. The moment capacity of the cross-section is then calculated with equation 8.10.

$$Z = d - \frac{1}{3}(\alpha \cdot d) \quad (8.9)$$

$$M_{Rd} = A_s \cdot f_{yd} \cdot Z \quad (8.10)$$

Calculation of zero moment section capacities (section F-F)

Table 8.10: Key properties zero moment section (F-F)

Section	$A_{s,\phi32}$	$A_{s,\phi16}$	d_0	d	b_{eff}
F-F	4825 mm ²	0	110 mm	1600 mm	3950 mm

By implementing different α value in equation 8.6, 8.7 and 8.8, until $F_c = F_s$, α was found to be 0.05812. This gives the height of the concrete compression zone:

$$t = \alpha \cdot d = 0.05812 \cdot 1600\text{mm} = 93\text{mm}$$

By implementation of the variables in equation 8.9, the internal lever arm was found to be:

$$Z = 1600 - \frac{1}{3} \cdot (0.05812 \cdot 1600 \text{ mm}) = 1569 \text{ mm}$$

By implementation of equation 8.10, the moment capacity of the zero moment sections are found to be:

$$M_{Rd} = 4825\text{mm}^2 \cdot 272 \text{ N/mm}^2 \cdot 1569 \text{ mm} = 2059 \text{ kNm}$$

Capacity supports

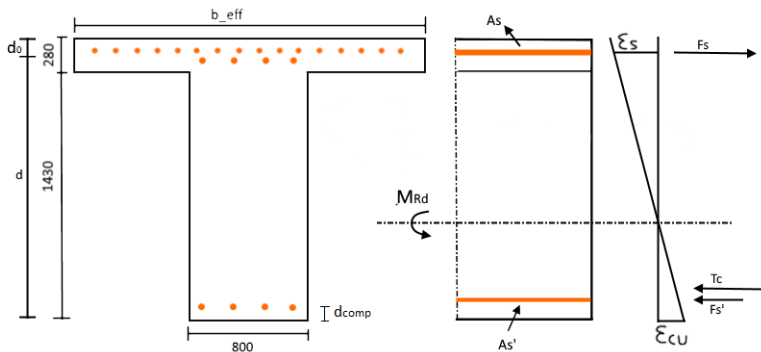


Figure 8.6: Flange on tensile side

Over supports, the flanges are on the tensile side of the cross-section. In such cases, the cross-sections are calculated as rectangular with the width equal to the width of the beams b_w . All the reinforcement inside the effective flange width b_{eff} has to be included. According to NS3473, chapter 9.5, the flange width of the tensile flange is the same as the adherent compression flanges (Norges Standardiseringsforbund, 2003).

At the bridge supports, the reinforcement drawings show that the beams have reinforcement in the compression zone. With the assumption that all the compression yields when the maximum concrete strain is reached, the compression zone factor was calculated with equation 8.11.

$$\alpha = \frac{A_s \cdot f_{yd} - A'_s \cdot f_{yd}}{0,8 \cdot b_w \cdot d \cdot f_{cd}} \quad (8.11)$$

The moment capacity of the compression zone can be found by equation 8.12. h' is the height between the tensile and compression reinforcement.

$$M_d = 0,8 \cdot f_{cd} \cdot (1 - 0,4 \cdot \alpha) \cdot \alpha \cdot b_w \cdot d^2 + A'_s \cdot f_{yd} \cdot h' \quad (8.12)$$

Maximum tensile reinforcement strain has to be controlled to ensure $\varepsilon_s \leq 10 \%$. Tensile reinforcement strain can be found by equation 8.3. The compression zone factor found in equation 8.11 is only valid if the compression reinforcement yields when the concrete reaches the ultimate strain ε_{cu} . The compressing reinforcement strain can be found by equation 8.13

$$\varepsilon'_s = \frac{\alpha \cdot d - d_{comp}}{\alpha \cdot d} \cdot \varepsilon_{cu} \quad (8.13)$$

Moment capacity calculations section D-D and E-E

Calculation of moment capacity parameters are given in table 8.11.

Table 8.11: Properties support sections (D-D, E-E)

Section	Upper face (OK)				Lower face (UK)		h'
	$A_{s,\phi32}$	$A_{s,\phi16}$	\bar{d}_0	d	$A_{s,\phi32}'$	d_{comp}	
D-D	29757 mm ²	2281 mm ²	148.8 mm	1561 mm	16889 mm ²	144.7 mm	1416.5 mm
E-E	24127 mm ²	1901 mm ²	135.1 mm	1575 mm	12064 mm ²	115.3 mm	1459.6 mm

Table 8.12: Moment capacity and controls section (D-D and E-E)

Section	Compression zone factor α (Equ 8.11)	Moment capacity M_{Rd} (Equ 8.12)	Ultimate reinforcement strain control: $\varepsilon_s \leq \varepsilon_{su} = 10 \text{‰}$		Compression reinforcement strain control: $\varepsilon_s' \geq \varepsilon_{yd} = 0.00137$	
			ε_s (Equ 8.3)	Control	ε_s' (Equ 8.13)	Control
D-D	0.3295	-11826 kNm	0.0071	OK!	0.0025	OK!
E-E	0.2573	-9821 kNm	0.0101	$\varepsilon_s = \varepsilon_{su}$ OK	0.0025	OK!

Calculated moment capacities

A summary of the calculated capacities are found in table 8.13.

Table 8.13: Moment capacity of the different sections

Section	M_{Rd}
A-A	5971 kNm
B-B	9184 kNm
C-C	6343 kNm
D-D	-11826 kNm
E-E	- 9821 kNm
F-F	2059 kNm

8.2.2 Shear capacity

The shear capacity is calculated according to the rules given in NS3473 2003 (Norges Standardiseringsforbund, 2003). The most critical section regarding shear forces appears at a distance d from the columns. In this thesis, it was decided to control the shear capacity at a distance d (right side) from column 9. Capacity regarding shear forces is to be controlled for both diagonal tension failure and for compressive shear failure. According to NS3473, the shear capacity can be assessed by three methods:

- Simplified method, Point 12.3.2
- Truss method, Point 12.3.3
- General design method, Point 12.5

In this thesis, it was decided to use the simplified method given in point 12.3.2 to assess the shear capacity.

Diagonal tension failure capacity

Diagonal tension failure capacity without shear reinforcement:

$$V_{cd} = V_{co} = 0.3 \cdot \left(f_{td} + \frac{k_A \cdot A_s}{\gamma_c \cdot b_w \cdot d} \right) \cdot b_w \cdot d \cdot k_v \leq 0,6 \cdot f_{td} \cdot b_w \cdot d \cdot k_v \quad (8.14)$$

Diagonal tension failure capacity without shear reinforcement is given by equation 8.15. Using this equation, all the reinforcement crossing in a 45 degree angle within a height equal z from the tensile reinforcement shall be included.

$$V_{sd} = \sum (f_{sd} A_{sv} \sin \alpha) \quad (8.15)$$

The angle of the reinforcement is 45 degrees, which means $\sin \alpha = 0,707$.

Total diagonal tension failure capacity

The total diagonal tension capacity is found by adding the contribution from the concrete and the reinforcement:

$$V_{tfc} = V_{cd} + V_{sd} \quad (8.16)$$

Compressive shear failure capacity

Compressive shear failure capacity is determined by equation 8.17, given in NS 3473, point 12.3.2.5.

$$V_{ccd} = 0,3f_{cd}b_wz(1 + \cot\alpha) \leq 0,45f_{cd}b_wz \quad (8.17)$$

Minimum transverse reinforcement

Demands regarding minimum transverse reinforcement are given in NS 3473, point 18.3.6 (Norges Standardiseringsforbund, 2003). It is a demand that beams shall have transverse reinforcement in the whole length. Minimum cross- section of transverse reinforcement is given by the equation :

$$A_{sv.min} = 0,2A_c f_{tk} \frac{\sin\alpha}{f_{sk}} \quad (8.18)$$

The minimum requirements of the transverse reinforcement are satisfied in the most critical section, in a distance d from axis 9.

Calculation of shear capacity section D-D

- $f_{td} = 1,5 \text{ N/mm}^2$
- $d = 1561 \text{ mm}$
- $k_A = 100 \text{ N/mm}^2$
- $\gamma_c = 1,4$
- $A_s = 35 \phi 32 \text{ bars} = 28148 \text{ mm}^2$
- $k_v = 1$
- $A_{sv} = 12 \phi 32 \text{ bars} = 9651 \text{ N/mm}^2$
- $f_{sd} = 272 \text{ N/mm}^2$
- $f_{cd} = 12 \text{ N/mm}^2$
- $z = 0,9d = 1405 \text{ mm}$

Diagonal tension failure capacity

$$V_{cd} = 1124 \text{ kN (Equation 8.14)}$$

$$V_{sd} = 1856 \text{ kN (Equation 8.15)}$$

$$V_{tfc} = V_{cd} + V_{sd} = 1124 \text{ kN} + 1856 \text{ kN} = 2980 \text{ kN (Equation 8.16)}$$

Compressive shear failure capacity

$$V_{ccd} = 6069 \text{ kN (Equation 8.17)}$$

Shear capacity

$$V_{Rd} = \min (V_d, V_{ccd}) = 2980\text{kN}$$

8.3 Degree of utilization: Comparing design forces and capacity

8.3.1 Moment

Not including external ASR expansion moment

Table 8.14: Degree of utilization, moment capacity: not including external ASR expansion moment

Section	Design moment M_d	Moment capacity M_{Rd}	Degree of utilization
A-A	4895 kNm	5971 kNm	82%
B-B	7457 kNm	9184 kNm	82%
C-C	6038 kNm	6343 kNm	95 %
D-D	-8443 kNm	-11826 kNm	71 %
E-E	-7517 kNm	- 9821 kNm	77%

Including external ASR expansion moment

Table 8.15: Degree of utilization, moment capacity: including external ASR expansion moment, section A-A, B-B, C-C

Section	Design moment M_d	Moment capacity M_{Rd}	Degree of utilization
A-A	6898 kNm	5971 kNm	115 %
B-B	8757 kNm	9184 kNm	95 %
C-C	8074 kNm	6343 kNm	127 %
F-F	3967	2059 kNm	192 %

8.3.2 Shear

Table 8.16: Degree of utilization shear capacity

Section	Design moment V_d	Moment capacity V_{Rd}	Degree of utilization
A-A	2511 kNm	2980 kNm	84 %

2D model Elgeseter bridge: Nonlinear analysis

DIANA is a finite element program, for predicting strength and deformations both in the linear and non-linear range. Among structural engineers, DIANA is considered to be one of the best tools to describe the non-linear behavior of concrete. Even though the program has not adopted a solution to apply deteriorating Alkali-silica reactions in concrete, it has a well-developed functionality regarding temperature-loading, which has been used to simulate alkali-silica behavior in this 2D model.

When applying temperature load to simulate ASR loading, it is essential to make sure that only the concrete expands on increasing temperature. This was implemented by setting the expansion coefficient in the reinforcement to zero.

The temperature loading was based on the assumption that the top plate expands twice as much as the beam. It was also decided to have a constant temperature field over the height of the plate and beam, which give a jump in the temperature field in the intersection between the beam and the plate, as shown in figure 9.1.

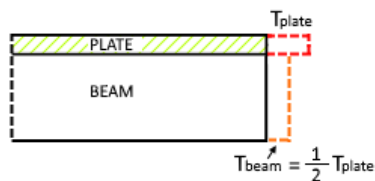


Figure 9.1: Illustration of selected temperature expansion

9.1 Solution strategy to model the ASR expansion in the superstructure

To implement temperature loading to the model, it was decided to run time-dependent heat flow analysis along with the nonlinear structural analysis. In this way, the temperature field in the model was implemented to the non-linear structural analysis for each time step. By manipulation of the heat flow properties (conduction coefficient) in the concrete and interface elements, the target temperature field, shown in figure 9.1 was achieved. Temperature flux was set as heat flow boundary's at the face of the plate and beam as the source of the temperature increase.

9.2 Creating the model

When modeling in 2D, the x-axis follows the longitudinal direction of the bridge and the y-axis follows the height of the bridge deck. The z-axis is normal to the x-y plane, as shown in figure 9.2.

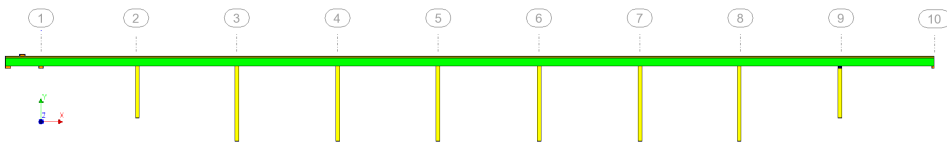


Figure 9.2: DIANA 2D model of Elgeseter bridge

9.2.1 Defining shapes

The bridge model consists of the T-beam, the abutment in axis 1 (3 shapes), the columns (axis 2-9) and the roller support in the end axis (axis 10).

The T-beam was defined by two separate shapes; the top plate and the underlying beam. The height of the plate and the beam was set to 280mm and 1430mm respectively. The geometry thickness of the plate was set to the 5500mm, while the thickness of the beam was set to 800mm.

The columns were defined with rectangular shapes with height according to the bridge drawings, revealed in section 4.2. The width of the columns was set to 800mm. The material thickness was set to 471mm to represents the same second moment of area as a circular ϕ 800mm column. As revealed in section 4.2, the column in axis 9 is hinged to the superstructure. This was implemented by defining a shape with low bending stiffness, as shown in figure 9.4. The geometry thickness of the hinged shape was set to 800mm.

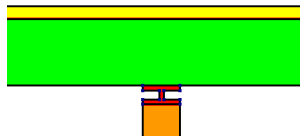


Figure 9.3: DIANA 2D model: Modeling of steel hinge axis 9

The three abutment shapes in axis 1 were modeled with a rectangular 1000x400 shape. The support in axis 10 was modeled with a 400mm square shape. The material thickness was set to 800mm.

The main- and shear- reinforcement in the T-beam was drawn and defined according to the original drawings. As a simplification, the upper reinforcement was defined at a height 100mm below the top edge of the flange plate, while the lower reinforcement was set at a height 100mm above the lower edge of the beam, as shown in figure 9.4. It was also decided to neglect all reinforcement in the columns.

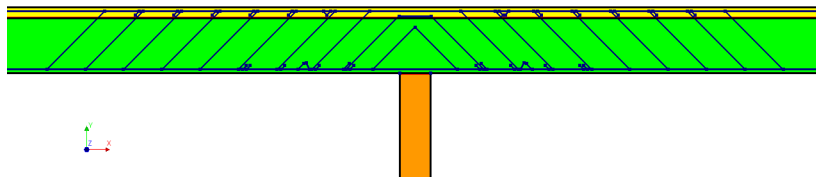


Figure 9.4: DIANA 2D model: Geometry of reinforcement, axis 3-8

9.2.2 Defining material properties of shapes

The plate, beam and columns were defined as plane stress material with concrete properties according to table 5.2. As ASR expansion is a long time load, the long-term E-modulus was used. Concrete properties in the beam and plate used in the model are shown in figure 9.5.

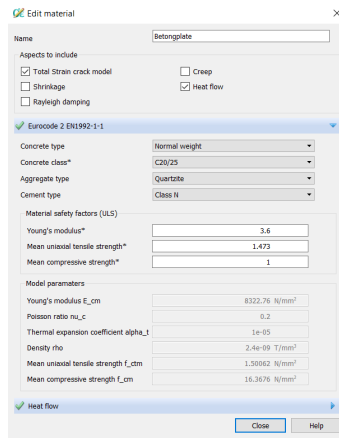


Figure 9.5: DIANA 2D model: Concrete properties, beam and plate

The supports in axis 1, axis 10 and the hinge in axis 9 were modeled as plane stress material with steel of high strength and stiffness.

The reinforcement was modelled with Youngs- modulus $200\ 000\ N/mm^2$. The design yield strength was set according to the properties revealed in section 5.3. The nonlinear relation between stress and strain was defined as shown in figure 9.6. To make sure that only the concrete expanded on increasing temperature, the expansion coefficient in the reinforcement was set to zero.

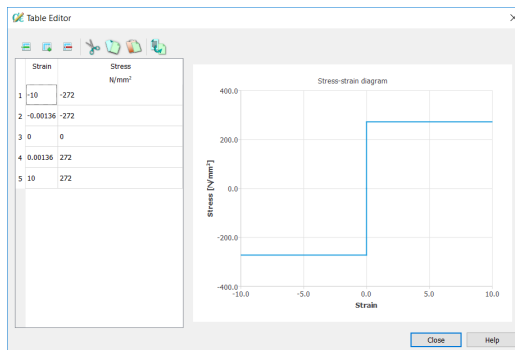


Figure 9.6: DIANA 2D model: Relation between strain and stress, reinforcement

9.2.3 Defining heat flow properties of the shapes

To enable uniform temperature behavior in each part (beam and plate), the conduction coefficient was set to an infinitely large number. The heat capacity of the plate and beam was set equal to each other (low value).

9.2.4 Interface elements

Structural interface elements are needed between shapes of different material definition, which means structural interfaces had to be defined between the beam and the intersecting supports and columns. The shear and normal stiffness of the interface material were set to $50\,000\text{N/mm}^3$ and $200\,000\text{N/mm}^3$ based on an initial guess. The conduction coefficient of the interface material was set to zero to prevent heat flow between the different parts. A heat flow interface with conduction coefficient equal to zero was also defined between the top plate and beam to prevent heat flow between these parts.

9.2.5 Structural boundary conditions

Displacements DOF's are described as U1, U2 and U3 corresponding to the displacement in the x, y, and z-direction respectively.

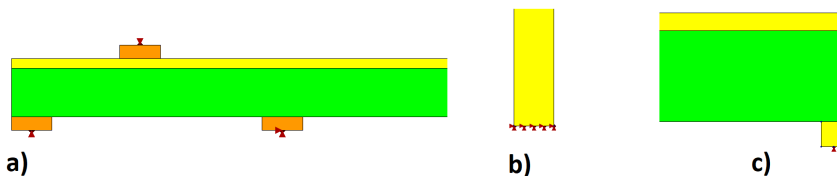


Figure 9.7: DIANA 2D model: Supports

Abutment axis 1

The abutment in axis 1 was modeled as shown in figure 9.7.

Columns

Translations U1, U2 and U3 were fixed along the lower edge of the columns, as shown in figure 9.7 b). By this method, the columns were fixed toward rotation.

Roller support, axis 10

Translations U2 and U3 were fixed in the mid-side node of the support- plate in axis 10, as shown in figure 9.7 c).

9.2.6 Dead load

The dead load was defined by two separate loads:

- Global dead load of modeled structure
- Even distributed force load applied to the top edge of the plate

By attaching global dead load, the program automatically applies the dead load of the modeled structure. The remaining load of the T-section (wearing course etc) was calculated based on the values given in section 6.5.1. The total dead load of the T-beam (including wearing course etc) is 101,3 kN/m and the weight of the load bearing concrete T-beam is 67,1 kN/m. This means that the remaining 34,2 kN/m had to be applied to the top edge of the plate.

Time-dependent factors were implemented such that the dead load was applied within the first 10 seconds of the analysis, as shown in figure 9.8.



Figure 9.8: DIANA 2D model: Dead load; time dependent factor

9.2.7 Temperature loading

The initial temperature in the whole structure was set to 0 °C. Heat flux was set as a boundary condition at the face of the beam and the top plate. By applying twice as much heat flux in the top plate as in the beam, the desired temperature field is shown in figure 9.1 was described for each time step.

By defining time-dependent factors, the heat flux was set to zero within the first 10 seconds and gradually increasing from $t = 11$ s, as shown in figure 9.9.

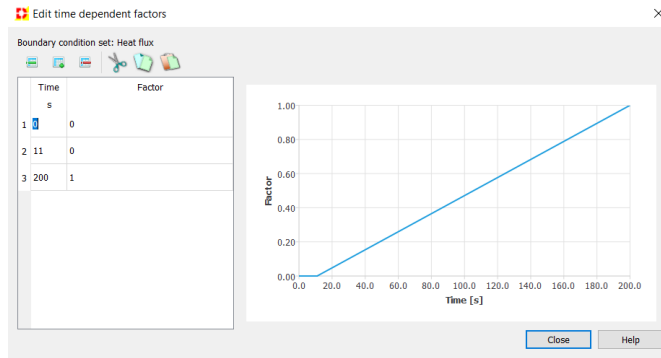


Figure 9.9: DIANA 2D model: Heat flux; time dependent factor

9.2.8 Meshing

The beam, plate, supports, and columns were meshed with 200mm hexa/quad dominant membrane elements. The quadrilateral elements were of type CQ16M and the triangular elements were of type CT12M, as illustrated in figure 9.10. The interface elements was of type CL12I, as shown in figure 9.11.

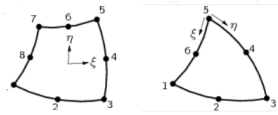


Figure 9.10: DIANA 2D model: CQ16M- elements to the left and CT12M- elements to the right (BV, 2012)

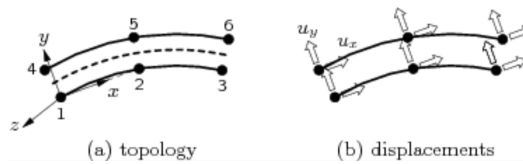


Figure 9.11: DIANA 2D model: CL12I interface element (BV, 2012)

The meshing over one of the internal columns can be seen in figure 9.12.

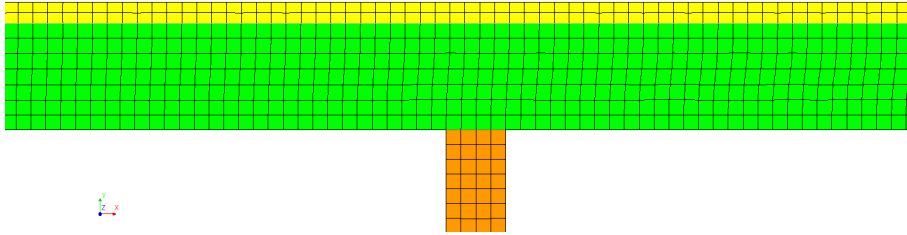


Figure 9.12: DIANA 2D model: Meshing over internal support

Embedded reinforcement The reinforcement in the model are embedded in structural elements, the so-called mother elements. According to (BV, 2011), the main characteristics of embedded reinforcement are:

- *DIANA ignores the space occupied by an embedded reinforcement. The mother element neither diminishes in stiffness, nor in weight. The reinforcement does not contribute to the weight (mass) of the element.*
- Standard reinforcements do not have degrees of freedom of their own.
- In standard reinforcements, the strains in the reinforcements are computed from the displacement field of the mother elements. This implies perfect bond between the reinforcement and the surrounding material.

9.3 Defining the analysis

9.3.1 Time steps

The selection of time steps has to be similar in the heat flow analysis as in the nonlinear structural analysis. Table 9.1 show how the different time steps 1-48 was implemented.

Table 9.1: DIANA 2D analysis: Selection of time steps

Time step	Seconds per time step	Loading
1-11	1s	Applying dead load to the structure. At step 10 (t=10s), all the dead load is applied
12-46	5s	Gradually increasing heatflux from step 12 (t=16s) to step 46 (t= 186s)

9.3.2 Time dependent heat flow analysis

Time steps from table 9.1 was implemented. The temperature was selected as the output of the analysis.

9.3.3 Structural nonlinear time dependent analysis

Time steps from table 9.1 was implemented. Temperatures from the heat flux analysis were implemented to the structural time-dependent analysis. Newton-Raphson was set as the iteration method. The maximum number of equilibrium iterations was set to 20. The force norm ratio and the displacement ratio was set as convergence criteria. The convergence tolerance was set to 0.01 and the abort criteria to 10000.

The following was selected as output selection:

- Displacement total translation global
- Strain total global
- Strain crack width global
- Stress total Cauchy global

9.3.4 Results: Transient heat flow analysis

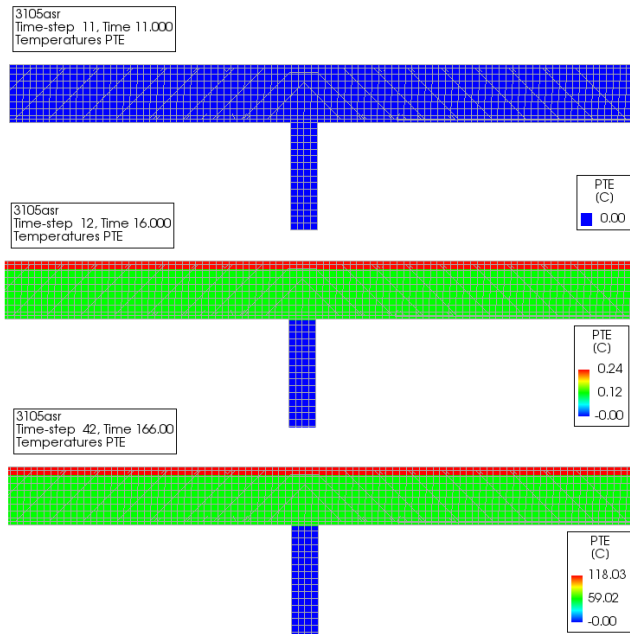


Figure 9.13: DIANA 2D model: Illustration of temperature field for selected time steps

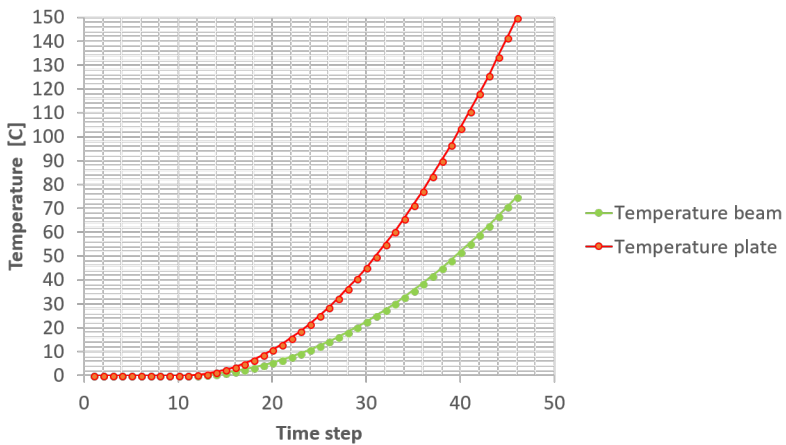


Figure 9.14: DIANA 2D model: Temperature in beam and plate, time steps 1-46

9.4 Results: Non- linear structural analysis

Displacements x - direction

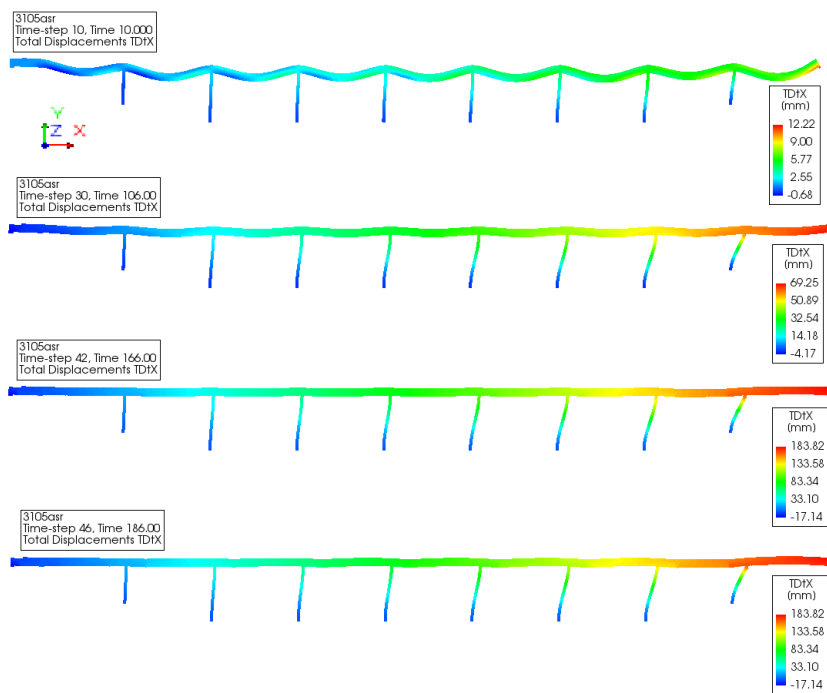


Figure 9.15: DIANA 2D model: Displacement x, illustration

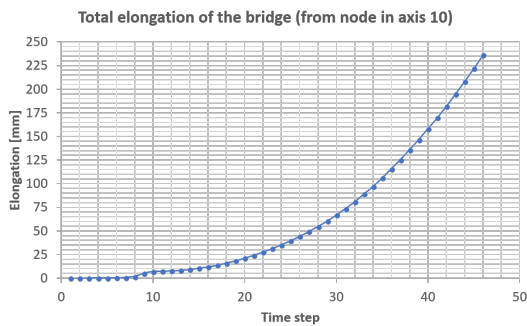


Figure 9.16: DIANA 2D model: Displacement x, time steps 1-46

Displacements y-direction

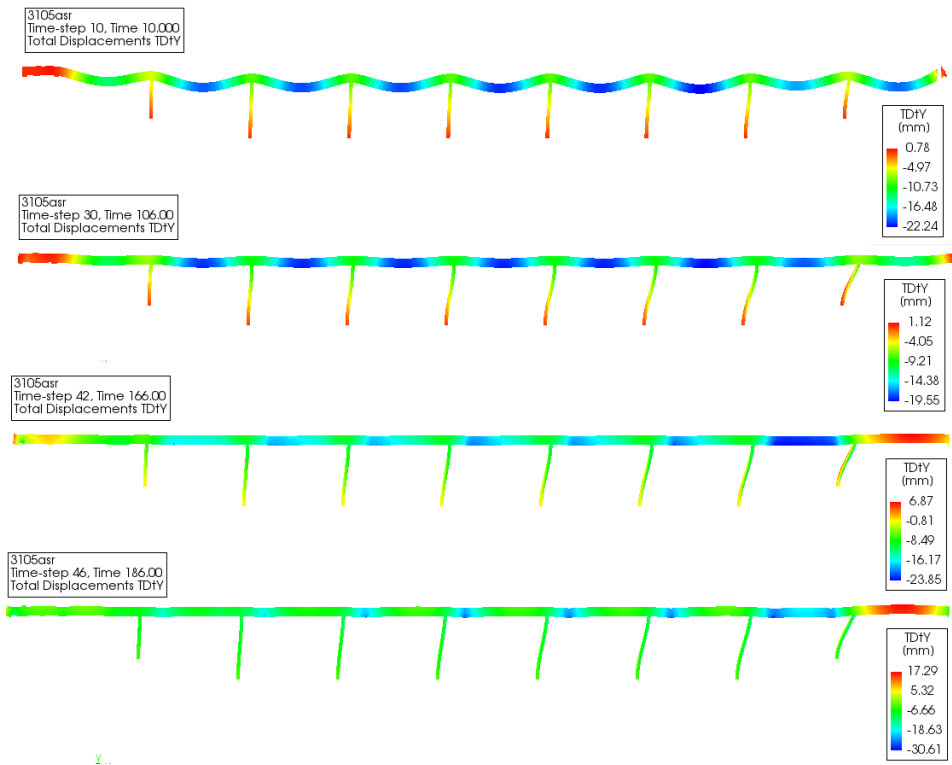


Figure 9.17: DIANA 2D model: Displacement y, illustration

At time step 10, all the dead load is applied to the structure, giving a maximal displacement equal to 25mm, as shown in figure 9.17. As the temperature starts to increase from time step 12, the field sections are gradually lifted up, reducing the displacement.

As the superstructure is pinned to the support in axis 9 and roller-supported in axis 10, the last span is allowed to curve upwards, introducing a curvature change in the zero moment section left of support 9.

Stresses in concrete, internal span (axis 6-7)

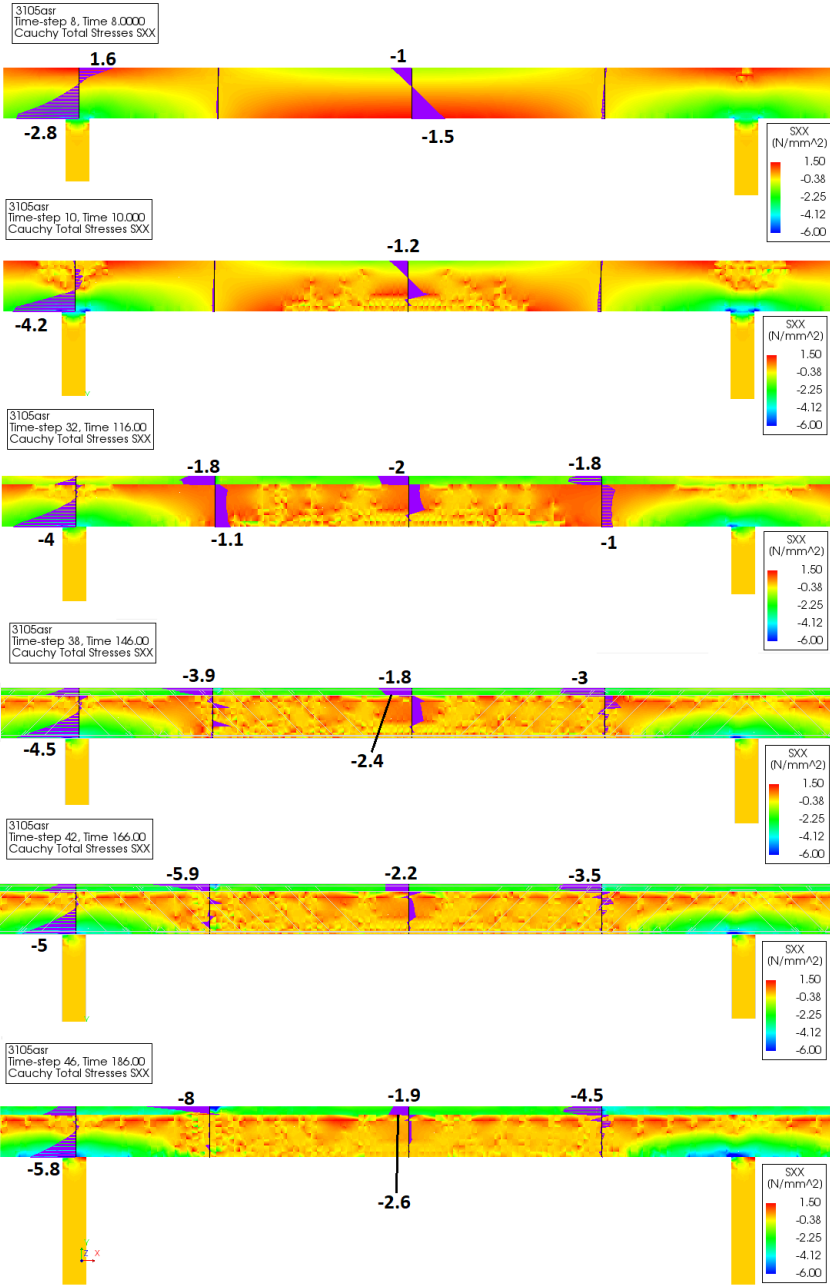


Figure 9.18: DIANA 2D MODEL: Stresses in concrete, $\sigma_{c,xx}$, internal span (axis 6-7)

As shown in figure 9.19, the bending stresses at the original zero moment spots builds fast as the temperature is increasing. The neutral axis in these sections are gradually lifted up, increasing the maximal stresses in the top of the plate.

At the beginning of the temperature increase, the bending stresses also build up fast in the field section. When the reinforcement in the zero moment spots starts to yield (step 35), most of the external moment due to the temperature increase is utilized on the field sections. This is believed to be the reason why the increase in bending strain from time step 38 to 46 is so small (Some of the increase in compression stresses also comes from axial strain resistance in the reinforcement).

As the external moment on the bridge due to more expansion in the plate builds up must faster than the moment introduced at the supports due do elongation of the bridge, it is believed that elongation of the bridge mainly contribute to curvature changes at the zero moment spots, at the right side of the internal columns.

Figure 9.19 display how the maximal bending stress is increasing in the section, 4.5m from the column in axis 6.

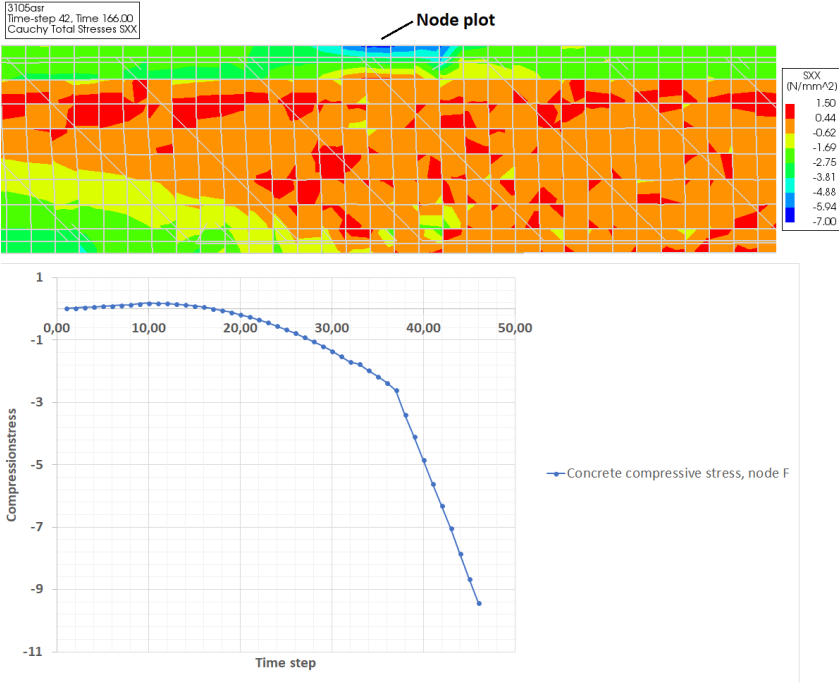


Figure 9.19: DIANA 2D model: Node plot, compression stress concrete, $\sigma_{c.xx}$

Crack width development, internal span (axis 6-7)

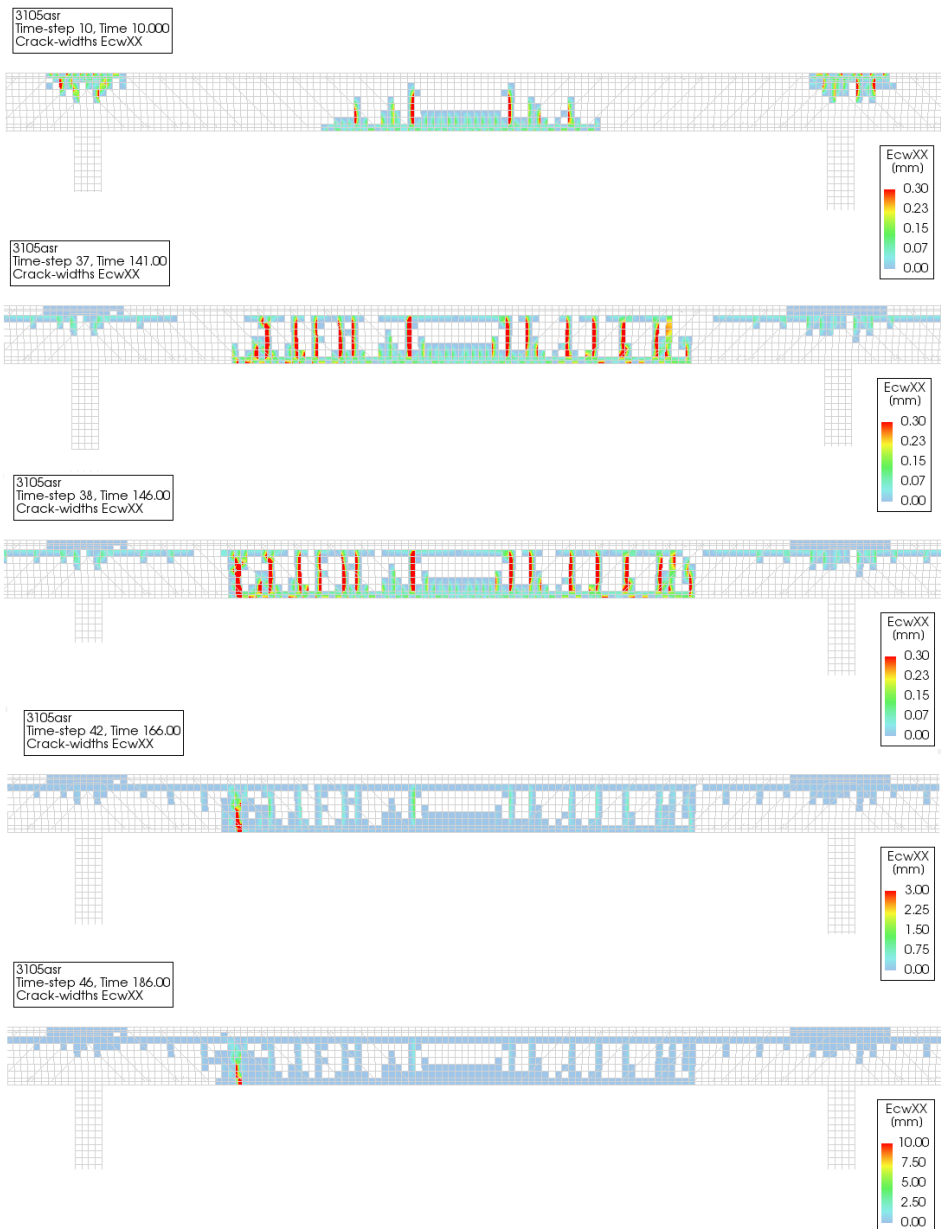


Figure 9.20: DIANA 2D model: Crack width, internal span (axis 6-7)

As all the dead load is applied at time step 10, small microcracks are appearing above the supports and in the field sections. As the temperature loading is applied, the cracks above the supports are gradually closing, leading these sections back to stadium I. The field sections remain in stadium II, with an increasing number of microcrack. The characteristic crack pattern in these is that they are closed in the top and bottom of the beam. The cracks appearing at the zero moment spots are typical bending cracks (Opens from the bottom of the beam).

Reinforcement stress (axis 6-7)

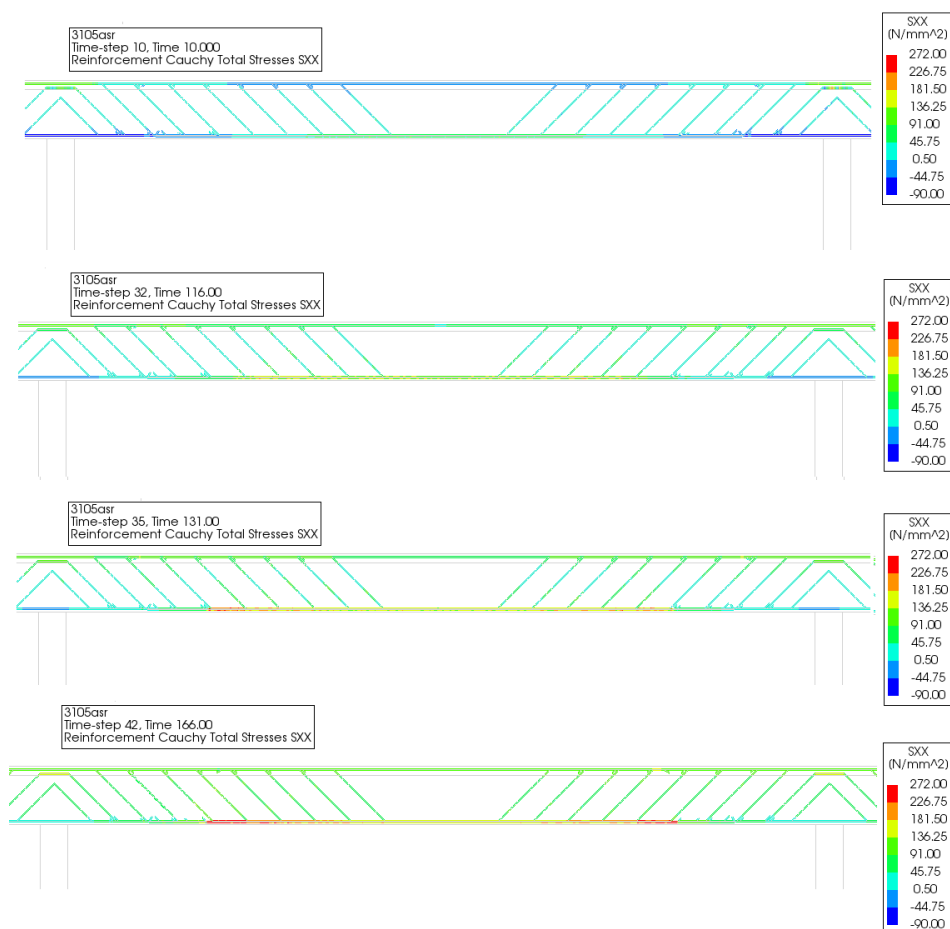


Figure 9.21: DIANA 2D model: reinforcement stress ($\sigma_{s,xx}$), internal span (axis 6-7)

Reinforcement strain (axis 6-7)

As shown in figure 9.22, both reinforcements, $3\phi 32$ M2 and $3\phi 32$ M3 are yielding.

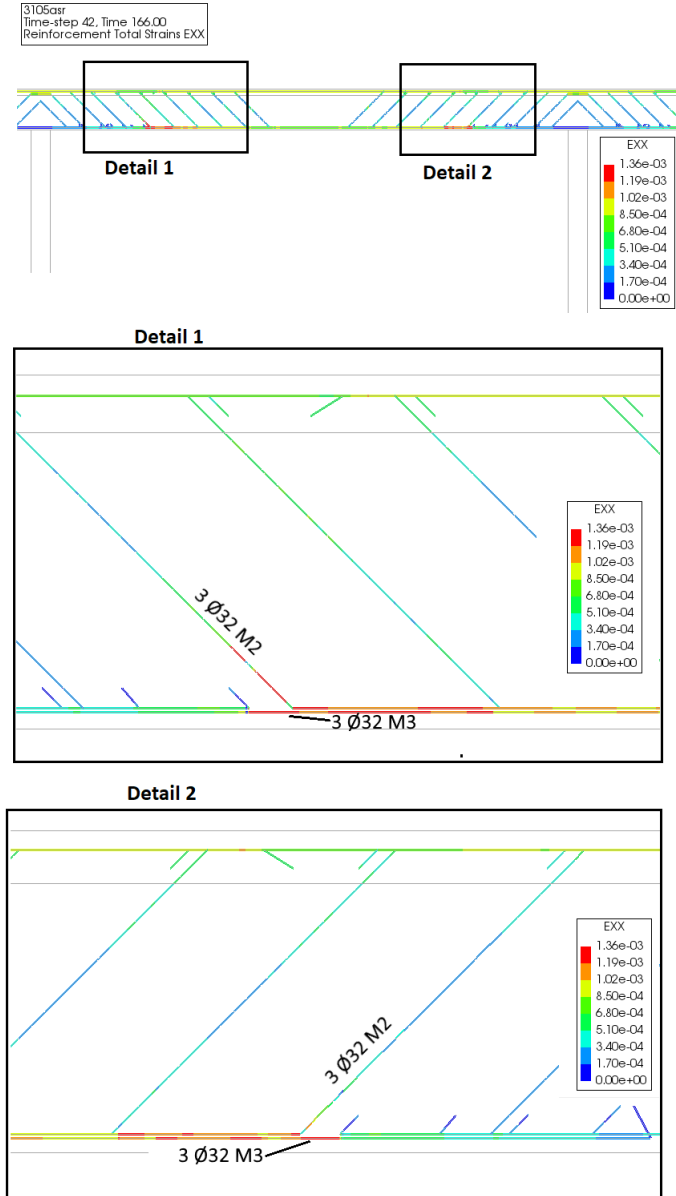


Figure 9.22: DIANA 2D model: reinforcement strain ($\varepsilon_{s,xx}$), internal span (axis 6-7)

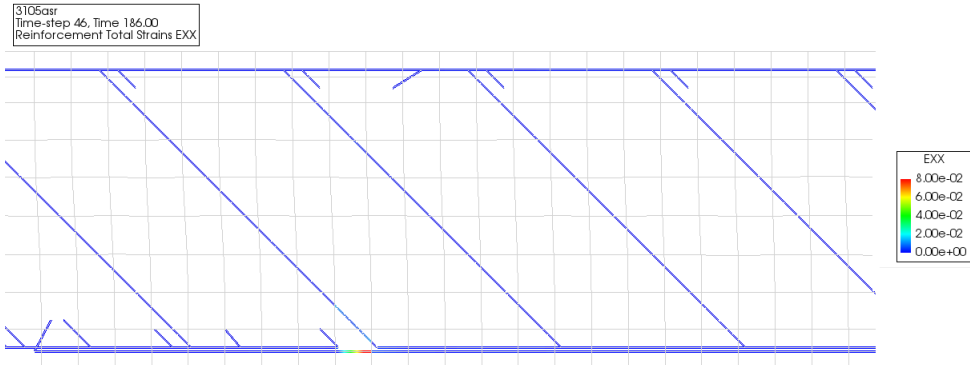


Figure 9.23: DIANA 2D model: Reinforcement strain, ($\epsilon_{s.xx}$), 4.5m from the column in axis 6 at time step 46

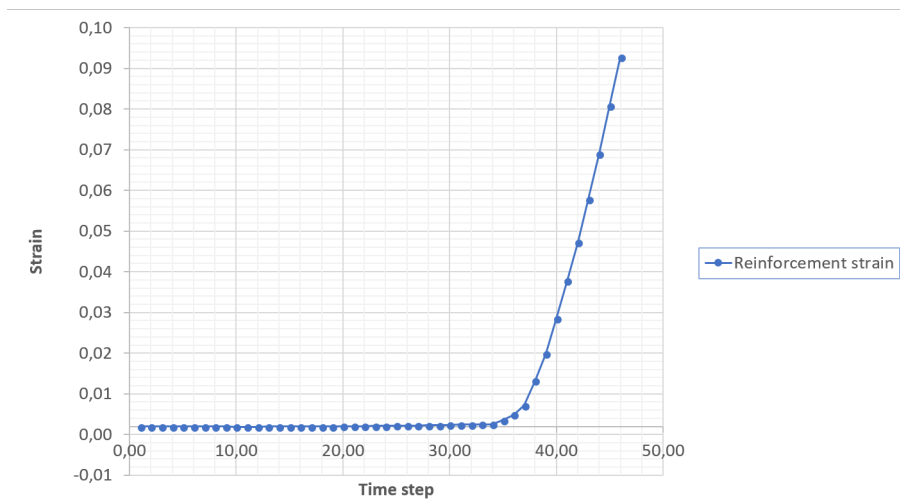


Figure 9.24: DIANA 2D model: Plot reinforcement strain, ($\epsilon_{s.xx}$), zero moment spot

Horizontal crack width, internal span (axis 6-7), time step 42

Small horizontal cracks are appearing where the most utilized reinforcements are coming down with an angle 45 degrees. Horizontal cracks in these areas may be critical for the coherence between the concrete and the main bars.

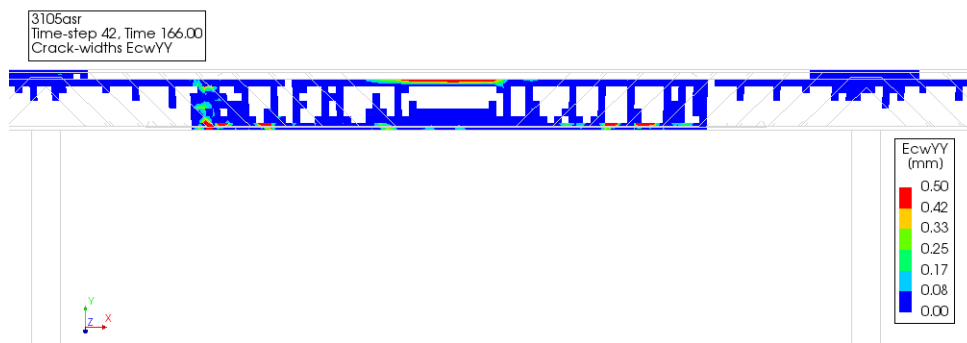


Figure 9.25: DIANA 2D model: Crack width, EcwYY, internal span (axis 6 -7)

Plot of strain state, field section (Section C-C)

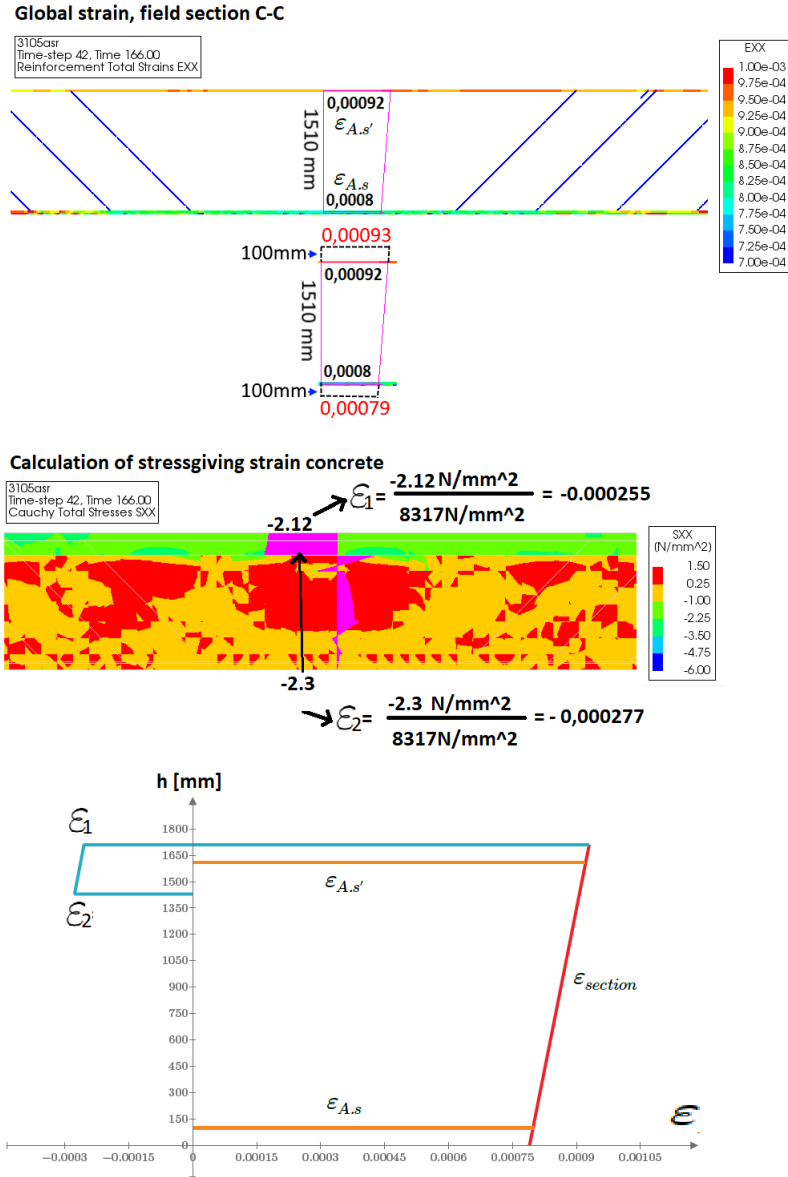


Figure 9.26: DIANA 2D model: Plot section strain, time step 42 (section C-C)

Chapter 10

Inspection of strain state of the T-beam in the longitudinal direction due to internal and external loading

In this chapter the strain state in field section C-C is investigated using the framework given in *ASR- Guidance for constructive analysis* by the Norwegian Public Roads Administration (2016). Complete calculation of the strain state in this section is given in appendix E.

Hand calculations of critical sections of the bridge using this method is a useful tool to control the results from the non- linear analyze in TNO Diana. As the hand calculation method is based on linear elastic behaviour of concrete and reinforcement, it is however only valid as long as these preconditions are fulfilled.

Under normal loading (dead load and external moment from ASR), these conditions are fulfilled in the field- and support- sections.

10.1 Introduction

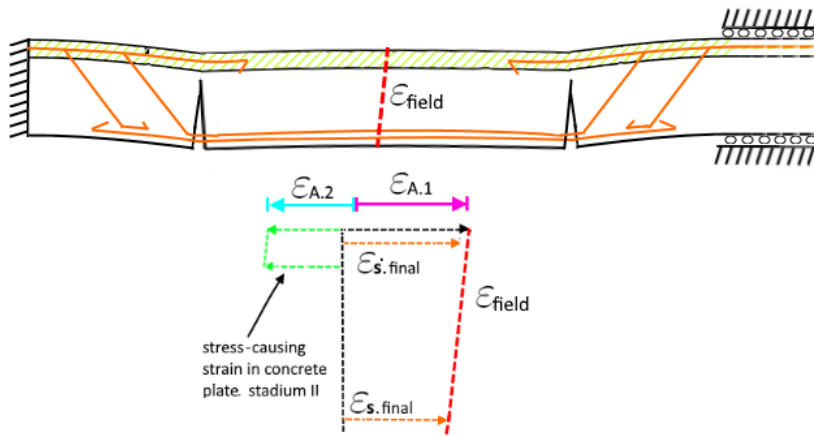


Figure 10.1: Strain field section

As revealed in section 3.3.4, three load models are proposed to cover the internal load effects on the bridge:

- Load model 1: Beam or plate with even (constant) or linear expansion over the cross-section
- Load model 2: beam or plate with more expansion in the upper part of the cross-section. (Example: T-beam with more expansion in the plate than in the web)
- Load model 3: Plate or T-beam with different expansion over the width of the cross-section. (Example: One of the bridge beam- plate T-beams has larger expansion than other T-beams)

As the target of this strain investigation is to evaluate the strain state of the internal T-beams in the longitudinal direction, a combination of load model 1 and 2 have been used. The calculation methods to investigate the combination of internal and external loads from load model 1 and 2 are given in section 3.3.4.

10.2 Control of result from TNO Diana model, Internal span (axis 6-7), field section C-C, time step 42

Step 1

- cracked section assumed (stadium II)
- $NA_{II} = 1277\text{mm}$
- $I_{II} = 5,774 \cdot 10^{15}$
- $E_{cm} = E_{cm} = 8317\text{N/mm}^2$

Step 2

- $\varepsilon_{plate} = 1.18$ (figur 9.13)
- $\varepsilon_{beam} = 0.59$ (figur 9.13)
- Load model 1: $\varepsilon_{A.1} = 0.59$
- Load model 2: $\varepsilon_{A.2} = 0.59$

Calculation of internal loads from load model 1 and 2 given in appendix E.

Step 3

External loads on section; Dead load M_g and external ASR moment M_i . As revealed in section 9.4, both reinforcements, $3\phi 32$ M2 and $3\phi 32$ M3 are yielding in the zero moment sections, as shown in figure 10.2.

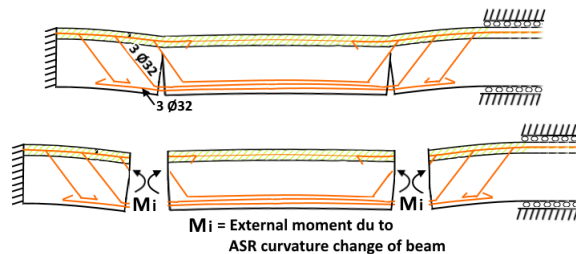


Figure 10.2: Elastic capacity of zero moment sections limiting the increase of field moment from ASR expansion

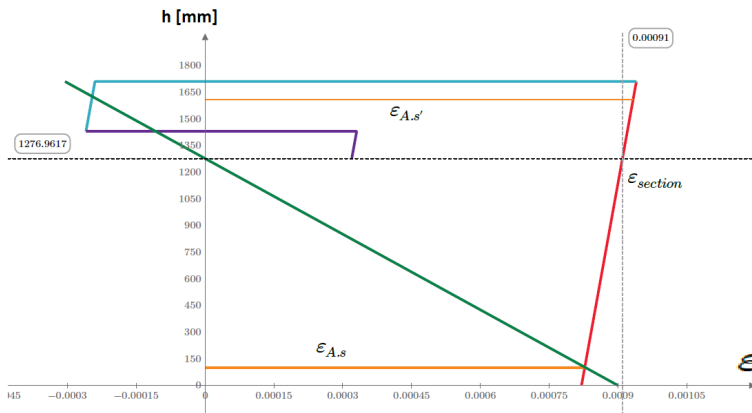
This means that external ASR moment on the bridge, M_i is limited by the capacity at the zero moment spots, with $A_s = 6 \phi 32$ bars (tensile reinforcement). The bar coming down with an angle 45 is assumed to be fully utilized in the x-direction when the crack opens (deformed state).

- $M_g = 2141 \text{ kNm}$
- $M_i = f_{yd} \cdot A_s \cdot (d - \frac{t_{flange}}{2})$ (Simplified method)
- $M_i = 272 \text{ N/mm}^2 \cdot 6\phi32 \cdot (d - \frac{t_{flange}}{2}) = 1929 \text{ kNm}$

Step 4 5

Rest of the steps are given in annex E

Plot strain state



Normal: $M_{norm,ext} = M_g = 2141 \text{ kN} \cdot m + M_i = 1929 \text{ kN} \cdot m$

Red line: Total strain of section

Light blue line: Strain causing stress in concrete plate.

Purple line: Strain causing stress in non cracked part of beam

Orange lines: Reinforcement strains

External load plots, without inner load effect

Green line: $M_{ext} = M_g = 2141 \text{ kN} \cdot m + M_i = 1929 \text{ kN} \cdot m$

Figure 10.3: Strain state

The hand calculated strain state of the field section is close to the strain plot achieved from the TNO Diana model, in the same section (figure 9.26). The green line represents the strain state of the section if the inner load effects were not applied. Comparing the green line to the red, the section has totally changed its curvature due to the internal load effect. The reinforcement strain, on the other hand, remains unchanged.

3D model Elgeseter bridge: Linear static analysis

In addition to the 2D model of the bridge, it was also made a 3D model of Elgeseter bridge in TNO Diana. In contrast to the 2D model, the 3D model was only used to run a structural linear static analysis. To model ASR expansion, incremental temperature load was applied to the superstructure according to figure 11.1.

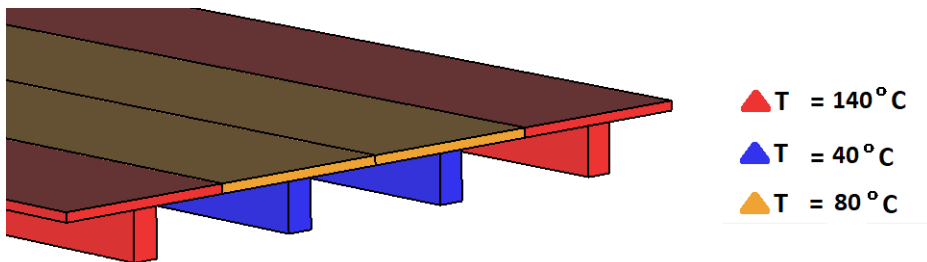


Figure 11.1: DIANA 3D model: Selection of temperature load

11.1 Creating the model

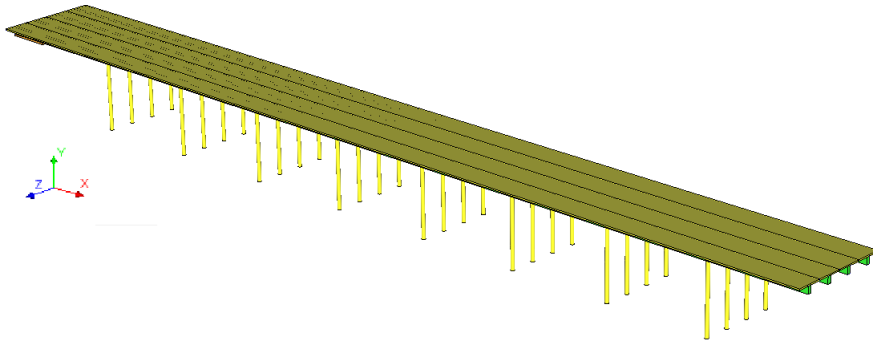


Figure 11.2: DIANA 3D model. X-axis follows longitudinal direction of the bridge

11.1.1 Defining parts

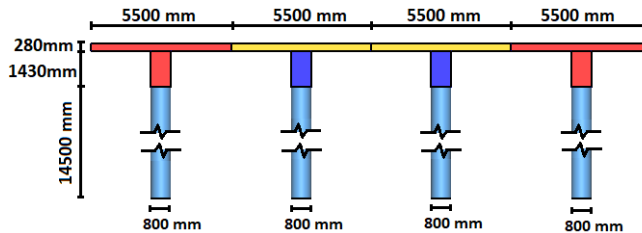


Figure 11.3: DIANA 3D model: Geometry cross- sections

As the aim of the model mainly was to look at the load distribution at the inner spans of the bridge, the same height of columns (14.5m) was defined for all columns.

As the aim of the model was to look at ASR effects in the longitudinal direction, it was decided to neglect all transverse reinforcement. The reinforcement in the inner T-beams is shown in figure 11.4. Except from the fact that all reinforcement in the underlying beams were drawn in the same layer (Not distributed over the width of the beams), the inner beams reinforcement were drawn (approximately) according to the reinforcement drawings on the bridge. According to the bridge drawings, the longitudinal reinforcement in the outer beams are designed slightly different than the inner beams. This was neglected in the model, which means the inner T-beam reinforcement were copied to the outer T-beams.

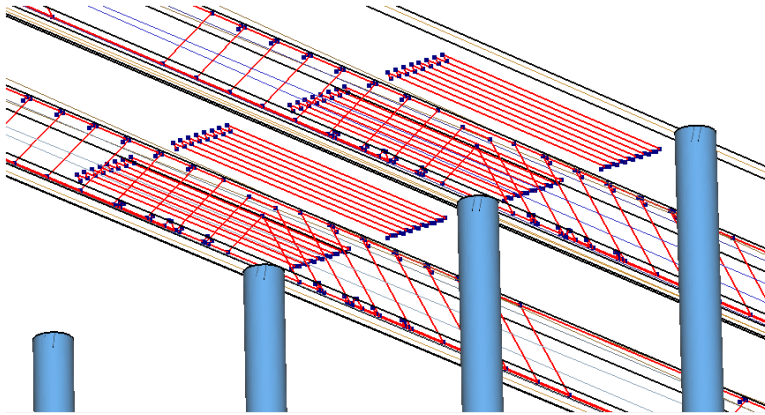


Figure 11.4: DIANA 3D model: Reinforcement in internal T-beams over supports

Defining material properties of parts

The material properties of the column and superstructure concrete were defined with the long-term E-modules according to table 5.1. Reinforcements young's modulus was set to $200\,000\text{ N/mm}^2$.

11.1.2 Structural boundary conditions

Columns and abutment in axis 1 were fixed. Roller support established in axis 10.

11.1.3 Loading

In addition to the global dead load defined by the program for each part, an even distributed load -6.2 kN/m^2 was applied to top surface of the inner plates (chapter 9.2.6, $\frac{-34,2\text{kN/m}}{5,5\text{m}} = -6.2$).

Incremental temperature loading were defined for each part of the superstructure according to figure 11.1.

Three load-combinations were defined:

- Load-combination 1: Only dead load
- Load-combination 2: Only temperature increment (ASR)
- Load-combination 3: $1 \cdot \text{Deadload} + 1 \cdot \text{Temperature increment}$

11.1.4 Meshing

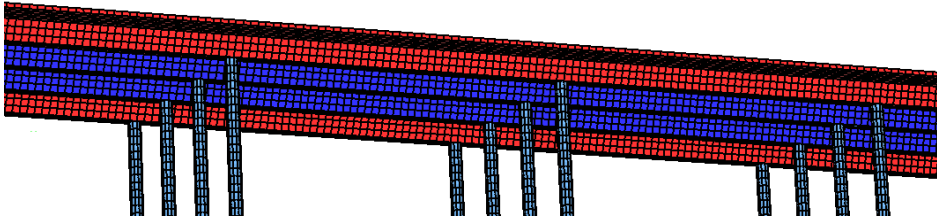


Figure 11.5: DIANA 3D model: Meshing

The structure was meshed with 400mm hexa/quad dominant solid elements. The different elements in the model are shown in figure 11.6. The superstructure mainly consists of CHX60 elements. Reinforcements are embedded to its mother element, as described in chapter 9.2.8.

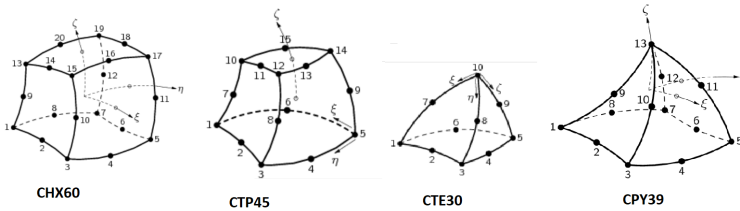


Figure 11.6: DIANA 3D model: Elements

11.2 Defining linear static analysis

Parallel direct sparse solver was defined as the solver for the linear system of equations. The tolerance was set to 10^{-8} .

Output selection:

- Displacement total translation global
- Strain total global
- Stress total Cauchy global

11.3 Results, load combination 2 (Only ASR loading)

11.3.1 Displacement Dtx

Figure 11.7 display the elongation of bridge for load combination 2.

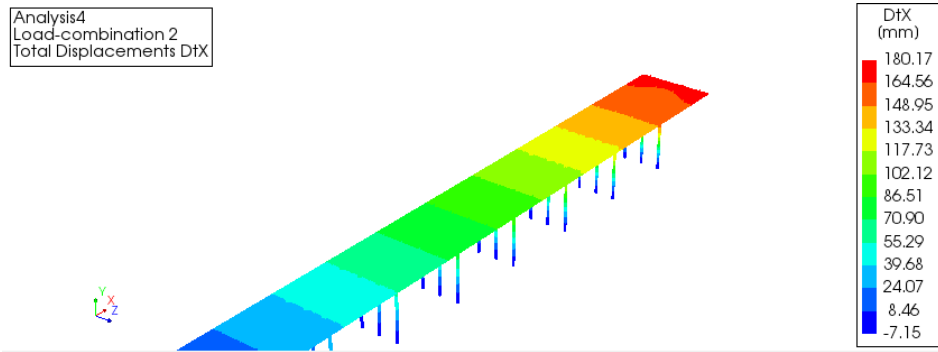


Figure 11.7: DIANA 3D model. Load-combination 2: Displacement Dtx

11.3.2 Strain, EXX

Different amount of longitudinal reinforcements influence the strain state in each section. In order to study this phenomenon, a probe line was defined in the neutral axis (Annex B) of one of the internal T-beams. As shown in figure 11.8, the bridge model has been strained more in the field sections than the support sections. Close to the end axis, the outer beams are not able to distribute strain to the inner T-beams, which results in a different strain state over the width of the bridge cross- section.

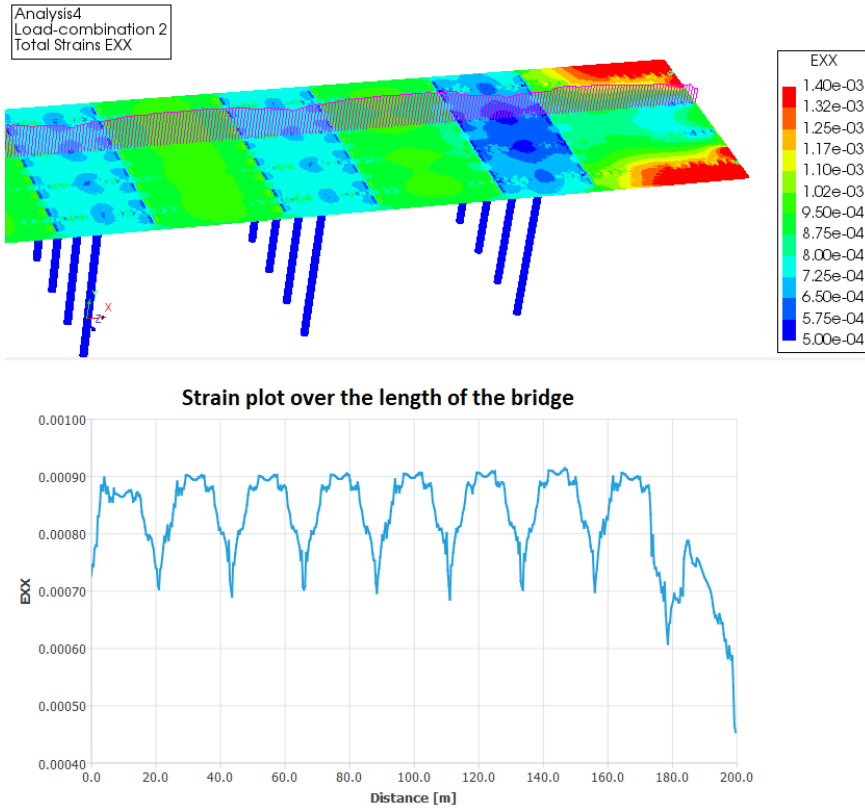


Figure 11.8: DIANA 3D model. Load-combination 2: Strain plot, internal T-beam

11.3.3 Shear stresses, SZX, end axis

The difference in the strain- state over the width of the cross-section has to be taken up as shear forces in the plate. This is shown in figure 11.9.

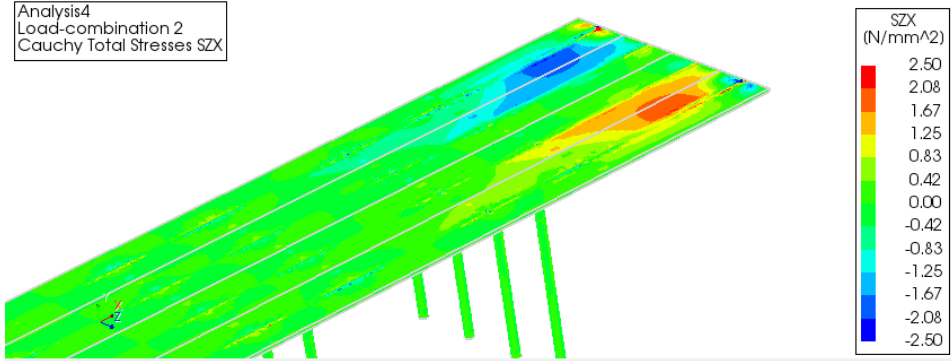


Figure 11.9: DIANA 3D model. Load combination 2: Shear stresses at end span, Cauchy total stresses SZX

11.3.4 Normal stresses, SXX, internal span

As shown in figure 11.10, the outer T-beam-plate has compression stress, and the inner the T-beam-plate has compression stress over the supports and tensile stresses in the field sections. The difference in the stress state in the plate over the supports and in the field sections is the large amount of reinforcement in the plate.

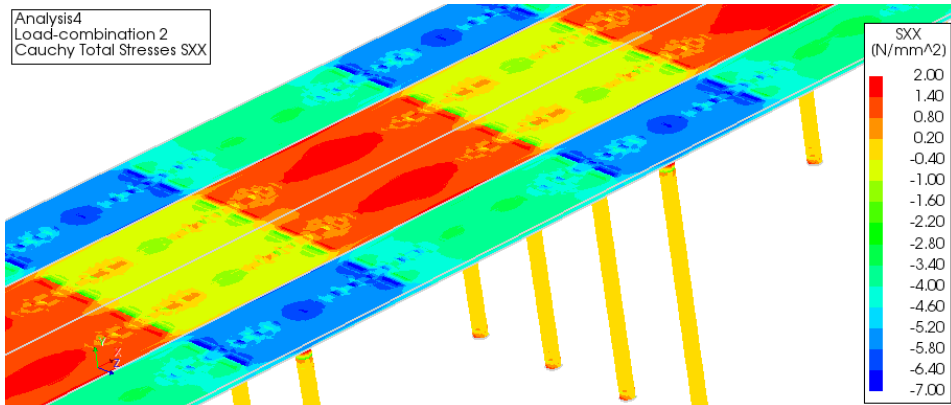


Figure 11.10: DIANA 3D model. Load combination 2: Span between axis 6-7, Cauchy total stresses SXX

Figure 11.11 display the stress at the underside of the superstructure. The central beams are strained and the outer beams are compressed. The largest tensile stresses appear in the original zero moment sections where the amount of reinforcement in the beams are low.

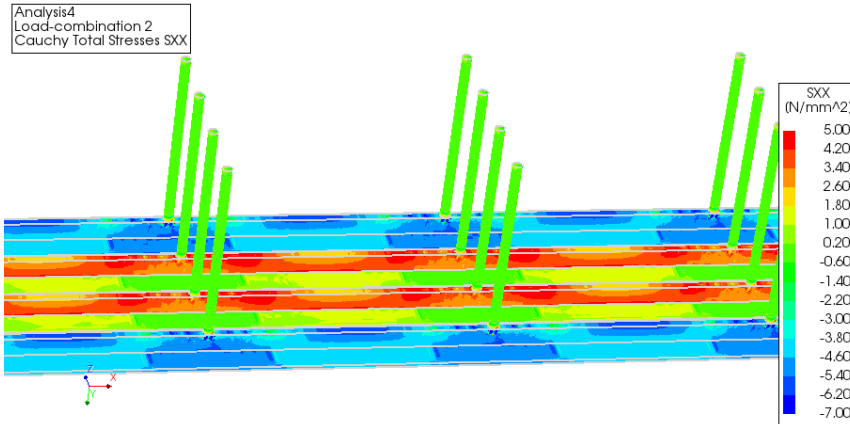


Figure 11.11: DIANA 3D model. Load combination 2: Span between axis 6-7, underside, Cauchy total stresses SXX

11.3.5 Reinforcement stress, SXX, internal span

As shown in figure 11.12, the reinforcement stress has surpassed the design yield stress of at the original zero moment sections.

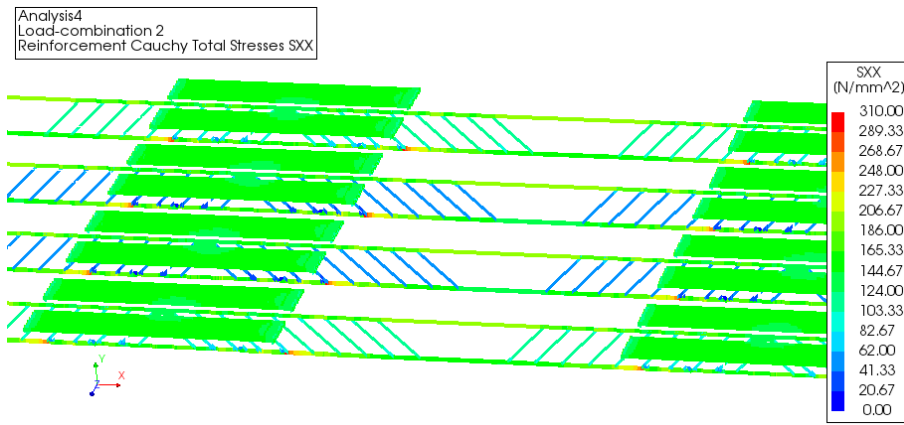


Figure 11.12: DIANA 3D model. Load combination 2: Field between axis 6-7, Cauchy total stresses SXX

11.4 Effective flange width considerations

Understanding how the normal stresses SXX are distributed over the width of the cross-section is important to make good assumptions of the effective flange width. To study this, a probe line was defined over the width of the inner T-beams in axis 6.

11.4.1 Normal stresses, SXX

Load-combination 1: Dead load

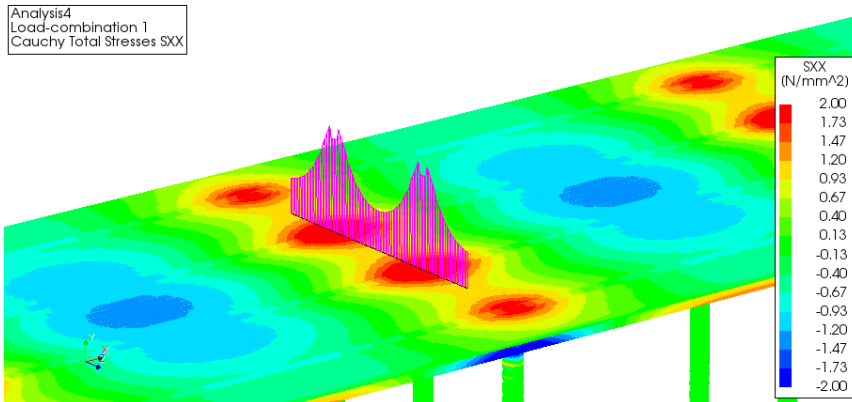


Figure 11.13: DIANA 3D model. Load combination 1: Cauchy total stresses SXX

Load-combination 2: ASR expansion

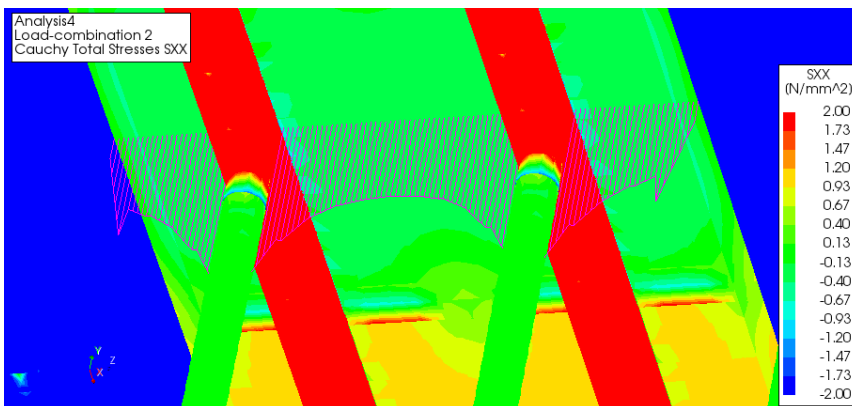


Figure 11.14: DIANA 3D model. Load combination 2: Cauchy total stresses SXX

Load-combination 1-3, plot

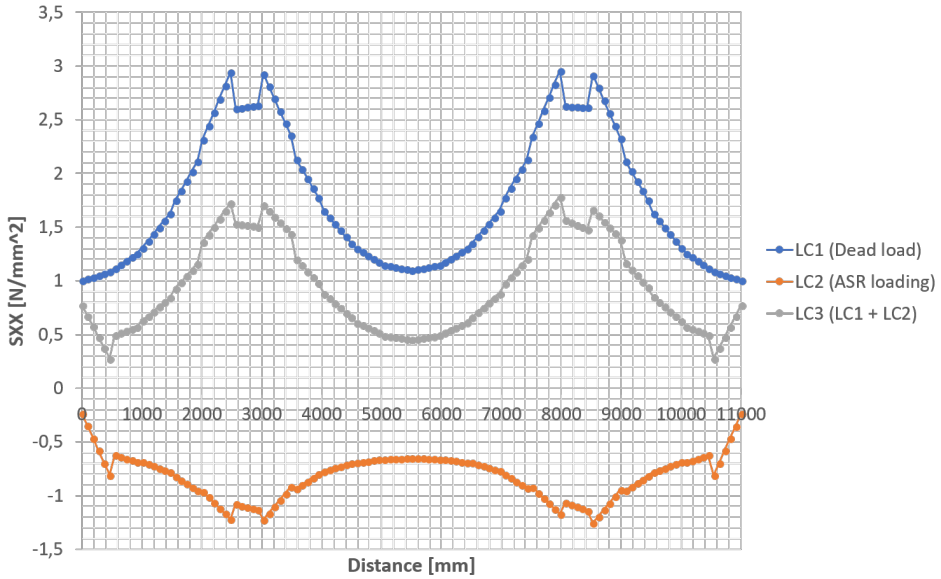


Figure 11.15: DIANA 3D model. Load combination 1-3: Cauchy total stresses SXX

11.4.2 Reinforcement stress, SXX

Load-combination 3: ASR expansion + Dead load

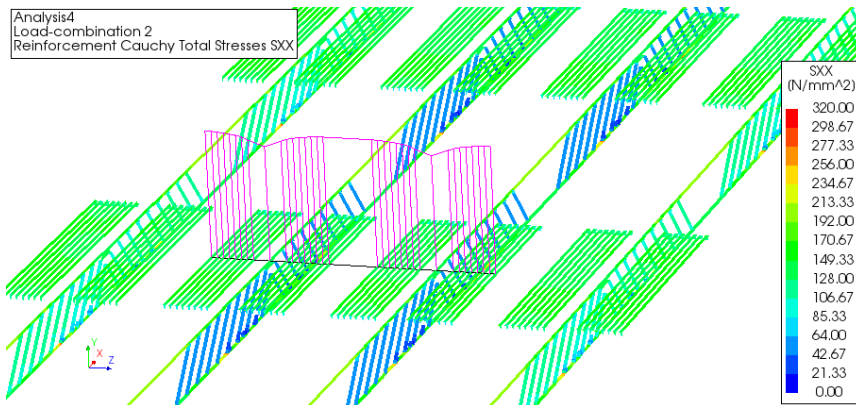
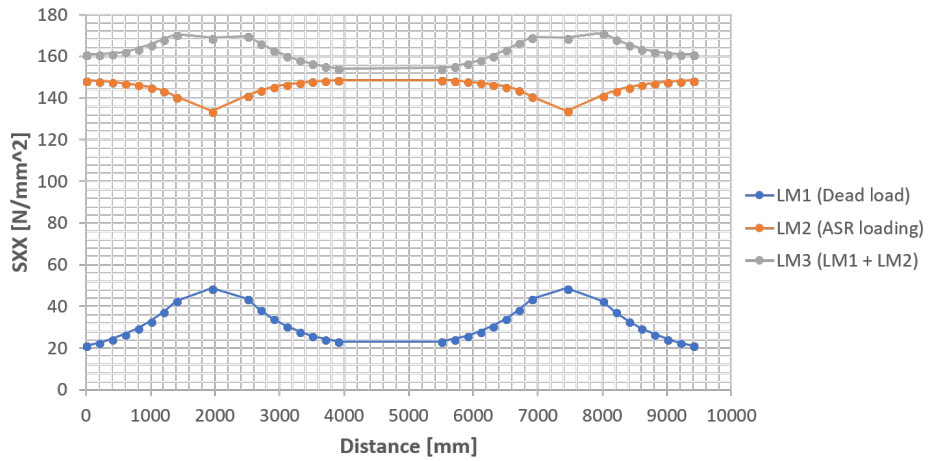


Figure 11.16: DIANA 3D model. Load combination 3: Cauchy total stresses SXX

Load-combination 1-3, plot**Figure 11.17:** DIANA 3D model. Load combination 1-3: Cauchy total stresses SXX

Chapter 12

Discussion

12.1 ULS Elgeseter internal T-beams, longitudinal direction

As revealed in section 8.3, the capacity of all sections was found to be on the safe side when neglecting the deformational load from Alkali - Silika expansion.

Three parameters were found to be important when calculating the additional moment from ASR expansion:

- E-modules of concrete in superstructure and columns
- Total elongation of the bridge
- How the expansion is distributed over the height of the T-beam.

Based on the guidance given by Norwegian Public Roads Administration (2016), it was selected to use the long-term E-modulus, as ASR expansion is a long-term load. As revealed in section 6.5.5, it was also assumed that the bridge has elongated 180mm. Knowing how the expansion is distributed over the height of the cross-section is very difficult to quantify. As revealed in section 2.3.3, the chemical reaction requires high water saturation to form an expanding gel. Knowing that the bridge plate is more exposed to water than the underlying beams, it was assumed that the expansion in the plate is twice as large as in the beams.

Implementing these parameters to the 2D frame analysis in Robot, the additional ASR moment was unfavorable for the field sections and favorable for the supports. From that reason, it was decided to only include the additional ASR moment when assessing the

capacity of the field sections. When including the extra ASR moment, the moment capacities were exceeded in the field section between axis 1-2 (15%), the internal field sections (27%) and the original zero moment sections, 4.5 m from the columns (92%).

Two factors may have overestimated the design moments in the field sections:

- Conservative assumptions when calculating the line load on the T-beam due to dead load (section 6.5)
- Calculating additional moments in the field sections based on linear elasticity

Calculating forces based on linear elasticity and the partial safety factor format may have been too conservative when including the additional moment from alkali-silica reactions in the field sections. As revealed in section 3.3.3, the additional moment from ASR expansion in the field sections is limited by the capacity of the adherent (original) zero moment spots. In Elgeseter bridge, these sections will start to yield, forming plastic hinges before the calculated moments based on linear elasticity are reached in the field sections.

The highest moment in the original zero moment sections was achieved for R412 load combination b. As this load combination includes both the additional moment due to ASR and moment due to thermal actions, it could be questioned how realistic this scenario is. When neglecting the moment due to thermal actions, the moment capacities in these sections would still be exceeded with 30%.

12.2 Finite element modeling of Alkali-Silica reactions

12.2.1 Simple T-beam model (2D) vs. 3D model of the bridge

Different approach to model expansion over the cross-section

Compared to a simple T-beam model (2D) which only offers to apply different expansion (temperature) over the height of the cross-section, the 3D model is also able to apply expansion over the width of the cross-section. This could be a major advantage. The most obvious advantage would be that it is possible to reveal shear stresses appearing over the width of the bridge cross-section, as shown in figure 11.9.

When modeling in 2D, higher temperature- expansion is applied to the top plate of the T-beam than the underlying beam, mainly because it is assumed that the plate has expanded more due to the environmental conditions. By adding more expansion to the plate, it is also, partly possible to cover the load effect from more expansion in the outer beams.

Assuming the outer T-beams on Elgeseter bridge expands more than the inner ones, the inner part of the bridge plate will be strained. Furthermore, the strained inner plate will

try to strain its underlying beams. As this strain is not induced in the neutral axis of the T-beams, it will introduce curvature change over the height of the cross-section, leading to additional moments in the longitudinal direction of the statically undetermined system. The achieved curvature on the inner T-beams could be compared to the curvature effect of adding more expansion to the top of a simple T-beam model. There is, however, a major difference: By adding temperature expansion to the plate of a simple T-beam model, the fact that the internal T-beams in the actual bridge are being strained by the outer T-beams is neglected. Keeping this in mind, the distribution of forces in the simple T-beam model will be different than in the actual bridge. In the field sections, the plate of the simple T-beam model may act similar to the real bridge. Over the supports, the situation is different. As the plate is already strained due to the dead load moment, additional strain of the inner plate due to the expansion of the outer T-beams may exceed the tensile strength at some localization's over the supports, leading the sections over in stadium II (cracked section).

This in contrast to the results of adding an expansion to the plate of a simple T-beam: When the concrete expands, the reinforcement will be strained. To achieve equilibrium, the concrete has to take up the compression- force on the cross- section from the reinforcement. Ultimately, this contributes to additional compression strain of the sections. If the support sections were in stadium II (cracked) after the dead load was applied, additional compression- strain on these sections might lead them back to stadium I (non-cracked). This is well illustrated in figure 9.19 and figure 9.20. At time step 10, when all the dead load is applied, the plate over the column is in a tensile strain state, having a few micro-cracks which mean the section could be considered somewhere in between stadium I and stadium II. As the temperature (more in plate than in beams) is applied gradually to simulate ASR, the small micro cracks appearing over the supports are being closed, leading the sections back into stadium I. Two factors are controlling this in the simple T-beam model:

- Factor 1: Additional moment from ASR reducing the support moments
- Factor 2: Additional compression of the concrete due to strained reinforcement.

In the real bridge, three factors are controlling the crack behavior (due to ASR loading) over the supports. In addition to the two former factors revealed, the tensile strain component (factor 3) due to more expansion in the outer beams will also influence the behavior over the supports.

Comparing the contribution from the three factors on the stress state in the plate above the supports is interesting. In the 3D linear static analysis, the following temperature expansions were applied.

- Outer T-beams: $\varepsilon_1 = 1.4 \text{ ‰}$
- Inner T-beam- plate: $\varepsilon_2 = 0.8 \text{ ‰}$
- Inner T-beam- beams: $\varepsilon_3 = 0.4 \text{ ‰}$

The result of the linear analysis (figure 11.14) revealed that load combination 2 (only ASR loading) contributed with additional compression stress to the top plate. This means that

the bending stress component (factor 1) and the reinforcement compression component (factor 2) are dominating the axial tensile stress component (factor 3) from more expansion in the outer beams.

Comparing the stress state over the supports in the 2D and 3D model, there is, however, a major difference. The plate in the 2D model is in a compressed strained state while the inner plates in the 3D model are in a tensile strain state when dead load and ASR loading is applied.

Even though the 3D model has an advantage compared to the 2D model as it is possible to apply loads over the width of the cross-section, predicting the real behavior of the bridge using linear analysis is not good enough. The linear static analysis distributes the strain (from the expansion of the outer beams) over the inner T-beams, without caring about cracks. In the real structure, it is natural to think that small micro cracks will appear in the weakest parts. This will relax the tensile strain on the adherent parts of the crack. It may also affect the strain state on the whole bridge.

Effective flange width considerations

Another disadvantage when modeling the bridge in 2D is the question of the effective flange width. In the 2D model, the same material thickness was defined to the T - beam, over the whole length of the bridge. This means that the bending stiffness in the 2D model may have been seriously overestimated, especially over the supports.

In order to study this, a probe line was defined over the support in axis 6. Figure 11.15 show the normal stresses SXX (in the direction of the bridge) in the concrete from load combination 1 (only dead load), load combination 2 (ASR loading) and load combination 3 (dead load + ASR loading). Even though the axial compression component from the reinforcement on the concrete has an impact on the stress- plot from load combination 2, it seems like the effective flange width for load combination 3 could be considered in a new context. Even though the effective flange width could be considered larger in load combination 3 than in load combination 1, the 2D model would still overestimate the bending stiffness over the supports.

The 2D model in this thesis is based on the integration scheme given in figure 12.1 a. The effective flange width problem could possibly be solved by modeling the top plate membrane perpendicular to the beam (figure 12.1 b).

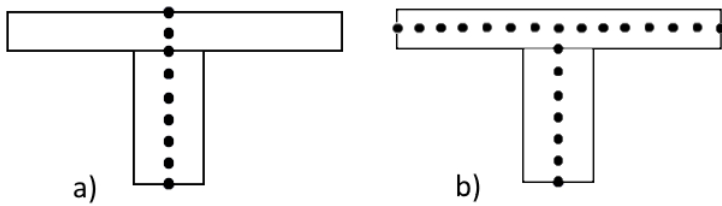


Figure 12.1: Node integration scheme

12.2.2 Capacity of original zero moment spots

Both the 2D and 3D model revealed that the design yield strength of the reinforcement was exceeded in the original zero moment spots, 4.5m from the support columns. Even though the reinforcement stress in the 3D model did not surpass the characteristic strength, it is believed that the 3D model may have underestimated the reinforcement stress in these sections as it was based on linear analysis, not taking into account cracked sections. Looking at the normal stresses (EXX) in figure 11.11, the tensile stresses are much larger than the characteristic tensile stress of the concrete. From that reason, it is believed that the result from the nonlinear analysis of the 2D model is better to predict the behavior of these sections, despite the effective flange width issues in the 2D model.

In the nonlinear 2D analysis, the stress-strain relation was defined according to figure 9.6, so that the maximal reinforcement stress was limited by the design yield stress. At time step 35 when the bridge model had elongated 110mm, the three reinforcement bars ($3 \phi 32M3$) started to yield. As the three reinforcement bars in the layer above ($3 \phi 32M3$) also began to yield, the reinforcement strain was accelerating, as shown in figure 9.24. As the reinforcement are embedded to their mother elements, the yield strain might be overestimated. Knowing that the reinforcement in the bridge was designed with smooth, large diameter reinforcement, it is believed that the strains are more distributed to the adherent parts of the crack opening than the model display. Based on this assumption it is believed that the reinforcement has enough ductile capacity to handle this strain.

As the neutral axis moves up to increase the internal lever arm, the stress increases in the upper part of the flange plate, as shown in figure 9.19. At time step 46, the compression stress has reached 9 Mpa, which is below the maximal compression stress of the concrete. As this is based on the 2D model width full flange width (5500 mm), this result might be underestimated compared to a nonlinear 3D analysis. At time step 46, the bridge has elongated 235mm, and the crack width is approximately 10mm. Comparing this with the crack width documented in the special investigation is necessary to predict the state of these sections in the bridge. The maximal crack width was documented to be up to 6mm in the most critical sections (Aas Jacobsen, 2013). As revealed in section 4.4, it was difficult to draw a conclusion of how much the bridge had elongated. In a worst-case scenario, the

inner T-beams could have elongated up to 200mm. Based on these assumptions, Elgeseter bridge in the given state could be compared to the 2D analysis at time step 43. Looking at figure 9.19, the maximal compression stress at this time step is approximately 7 Mpa, which is below the maximal compression stress of the concrete. Knowing that concrete has some plasticity when the maximal compression stress is reached, it is assumed that these sections are able to withstand, as long as the reinforcement bars in the cracked sections are protected towards aggressive corrosive actions. At the same time, it is important to keep in mind that the results of the 2D model are based on the assumption that the plate has twice as much expansion load compared to the underlying beam. By adding more expansion to the plate compared to the beam, it would induce a larger curvature change of the T-beam and the final result in these sections would look somewhat different.

12.3 Consequences of forming plastic hinges

As the reinforcement is yielding in the original zero moment sections, the stiffness is locally reduced, forming plastic hinges. This will have an impact on the shear and moment distribution on the bridge. As the plastic hinges occur where the moment due to dead load is close to zero, the effect on the dead load distribution is assumed to be almost unchanged. Regarding traffic moment, the situation is different. As these sections will have limited stiffness, the moment will increase in other parts of the bridge, especially over the supports.

12.4 Recommendations of preventive actions on Elgeseter bridge

Knowing that the chemical conditions related to Alkali-Silica reactions require a high water saturation, it is recommended to continue preventive actions to reduce water saturation in the concrete.

Map cracking and cracks appearing due to the structural conditions may increase the penetration of aggressive chlorides. From that reason, it is essential to protect the reinforcement at the crack localizations. At the original zero moment sections where the most significant cracks appear, it is also recommended to protect the reinforcement. At the same time, it is important to keep track on the crack opening development. By using an elastic mortar it is assumed that this could be difficult.

As revealed in section 4.6, carbon fiber strengthening have been implemented at some of the inner beams where the largest vertical cracks appear. Even though this will not reverse the process of reinforcement yielding in the most critical sections, it may relieve

the reinforcement if the bridge expands more. Knowing that the field sections also have to withstand additional moments due to Alkali- expansion, it may also help on these sections.

Chapter 13

Conclusion

Purpose of thesis:

- Literature review about damages to concrete structures and how it affects the structural behavior, extended with a more in-depth review about alkali-silica reactions.
- Structural safety assessment (ULS) of Elgeseter bridge in the longitudinal direction, not taking into account structural damages on the bridge.
- Dive further into the topic regarding Alkali-Silica reactions on Elgeseter bridge. The overall scope was to get an understanding of how Alkali- Silika expansion affects the superstructure of the bridge.

13.1 Literature review about damage to concrete structures

Four damage mechanisms were investigated; Freeze-thaw cycle, sulfate attack, alkali-silica reactions and reinforcement corrosion. The process of degradation of concrete and corrosion of reinforcement are closely connected. The different degradation mechanisms mainly lead to cracks or spalling, which reduces the resistance towards penetration of aggressive substances to the reinforcement. As the concrete depends on the reinforcement to take up tensile stresses, this is the most critical degradation mechanism. Cracks or spalling may also reduce the structural capacity of concrete due to a reduction of effective load-bearing cross- section, reduced bond strength and general loss of interaction between the concrete and the reinforcement bars.

13.1.1 Alkali- silica reactions

One of the effects of alkali-silica reactions is the formation of a swelling gel that expands in contact with water. This could lead to severe elongation of a bridge. Due to different environmental conditions around a bridge, the most exposed surfaces may have higher levels of water saturation, which means the expansion might be different over the height and width of a cross-section. In addition to the elongation, different expansion over the cross-section may lead to curvature changes of the bridge cross-section. For statically undetermined structures, elongation and curvature changes lead to additional moments and forces on a structure. As the engineers responsible for the design of bridges suffering from alkali- reactions were not able to predict this chemical reaction, additional forces due to ASR were not taken into account in the design process of these bridges.

13.2 Structural safety assessment of inner T- beams (ULS), longitudinal direction

13.2.1 Loads

Traffic loads and load combinations were calculated according to Norwegian Public Roads Administration handbook R412. Wind and thermal loading were calculated according to the Eurocodes as these load- actions are not defined in handbook R412. Calculation of additional deformational load due to alkali-silica expansion was conducted assuming the bridge has expanded 180mm, and that the expansion load in the plate is twice as large as in the underlying beams.

13.2.2 Capacity control

The bridge was build in 1951, which means the capacity control had to be assessed according to NS3473 2003: *Design of concrete structures*. The capacity control of the different sections was calculated based on the original drawings of the bridge, not taking into account structural damages or concrete degradation.

The shear and moment capacity was on the safe side when neglecting the deformational load from alkali-silica expansion. The moment due to alkali-silica reactions was found to be unfavorable for the field sections. When taking this additional moment into account, the moment capacities were exceeded in the field section between axis 1-2 (15%), the internal field sections (27%) and in the original zero moment sections, 4.5m from the columns (92%)

13.3 Investigation of alkali- reactions on Elgeseter bridge using FEM- models

Two separate models were made of the bridge in the finite element program DIANA.

- 2D model, longitudinal direction: Nonlinear analysis
- 3D model: Linear static analysis

Adding thermal load was used as the solution strategy to simulate ASR expansion on the bridge models (coefficient of thermal expansion in the reinforcement was set to zero). Comparing the two models, the two most important advantages with the 3D model were the question of the effective flange width and the opportunity to add temperature expansion over the width of the cross-section.

Both models revealed large tensile stresses in the original zero moment sections, 4.5m from the columns. The crack development on the bridge found by the 2D model seemed to be in good correlation with the field investigations on the bridge. With 3D model, it was also possible to detect shear forces appearing in the plate due to different strain over the width of the cross-section at the end span.

Bibliography

Aas Jacobsen, 2013. *Rapport fra spesialinspeksjon 2012*. <https://www.merccell.com/sv-se/m/file/GetFile.ashx?id=43152040&version=1>. [Gathered: April 2, 2018].

Aas Jacobsen, 2015. *Documentation of preventive actions*. <http://docplayer.me/10148008-Elgeseter-bru-elgeseter-bru-elgeseter-bru-bygd-1949-51-beton.html> [Gathered: June 05, 2018].

Ahlberg, S., 2012. Bevara betongen. AB Svensk Byggtjenst, Stockholm, Sweden.

Apostolopoulos, C. A., Demis, S., Papadakis, V. G., 2013. Chloride-induced corrosion of steel reinforcement - mechanical performance and pit depth analysis. *Construction and Building Materials* 38, 139 – 146.

Bertolini, L. B., Elsener, B., Pedferri, P., Redaelli, E., Polder, R., 2013. Corrosion of steel in concrete. Wiley-VCH Verlag GmbH Co. KGaA, Weinheim, Germany.

Blight, G., Alexander, M., 2011. Alkali-Aggregate Reaction and Structural Damage to Concrete. Engineering Assessment, Repair and Management. CRC Press Taylor Francis Group.

BV, T. D., 2011. Diana finite element analysis 9.4. 2. Delft, The Netherlands.

BV, T. D., 2012. Diana finite element analysis 9.4. 4. Delft, The Netherlands.

De Schutter, G., 2013. Damage to Concrete Structures. Taylor Francis Group, LLC, Boca Raton, Florida.

Federation for Structural Concrete, I., 2013. fib Model Code for Concrete Structures 2010. Ernst Sohn GmbH Co. KG.

Norges Standardiseringsforbund, 2003. Ns3473: Design of concrete structures. Design- and detailing rules,.

Norwegian Public Roads Administration, 2014. Hndbok R412: Bruklassifisering.

-
- Norwegian Public Roads Administration, 2016. *ASR Guidance for structural analysis*. https://www.vegvesen.no/_attachment/1464266/binary/1124153?fast_title=Nr+601+Alkalireaksjoner+-+Veiledning+for+konstruktiv+analyse.pdf [Gathered: May 09, 2017].
- Page, C., 2002. Advances in understanding and techniques for controlling reinforcement corrosion. ICC 15th International Corrosion Congress, Granada 22-27 September, Granada, Spain.
- Pigeon, M., Pleau, R., 2010. *Durability of concrete in cold climates*. Taylor Francis group, Abington, Englandy.
- Powers, T., 1945. A working hypothesis for further studies of frost resistance of concretes. *Journal of the American Concrete Institute* 41.
- Sorensen, S., 2015. *Betongkonstruksjoner - Beregning og dimensjonering etter Eurocode 2*, 2nd Edition. Vigmostad Bjarke AS.
- Vegvesen, S., 2015. *Bridge projecting handbook n400*. Norwegian National Road Administration, ISBN, 978–82.

Appendix

A Calculation of wind load

Handbook N400, chapter 5.4.3

Elgeseter bridge is in wind load class I, which means that I will neglect dynamic actions from wind on the bridge.

Wind velocity and velocity pressure

NS- EN 1991-1-4

Geographic parameters:

Trondheim kommune

NA.4(901.1)

$$v_{b,0} := 26 \frac{m}{s}$$

Basic values

NA.4.2(2)P (901.1)

$$c_{alt} := 1 \quad (H < 900 \text{ m})$$

Table NA.4(901.4)

$$c_{dir} := 1$$

Table NA.4(901.5)

$$c_{season} := 1$$

NA.4.2(2) P

$$c_{prob} := 1$$

NA.4.2(2) P

$$v_b := c_{dir} \cdot c_{season} \cdot c_{alt} \cdot c_{prob} \cdot v_{b,0} = 26 \frac{m}{s}$$

Mean wind

Table NA.4.1

$$k_r := 0.17 \quad z_0 := 0.01 \text{ m} \quad z_{min} := 2 \text{ m}$$

Height of drivinglane

$$z := 16.5 \text{ m} \quad \% \text{ Bridge drawings}$$

4.3.2

$$c_{r,z} := k_r \cdot \ln\left(\frac{z}{z_0}\right) = 1.259$$

4.3.1

$$c_0 := 1$$

4.3.1

$$v_{m,z} := c_{r,z} \cdot c_0 \cdot v_b \quad v_{m,z} = 32.746 \frac{m}{s}$$

Wind turbulence

4.4(1)

$$k_1 := 1$$

4.4(1)

$$I_v := \frac{k_1}{c_0 \cdot \ln\left(\frac{z}{z_0}\right)} = 0.135$$

NA.4.5

$$\rho := 1.25 \frac{kg}{m^3}$$

NA.4.5

$$k_p := 3.5$$

NA.4.4

$$v_p := v_{m,z} \cdot \left(1 + 2 \cdot k_p \cdot I_v\right)^{\frac{1}{2}} = 45.667 \frac{m}{s}$$

NA.4.5

$$q_{p,notraffic} := 0.5 \cdot \rho \cdot v_{m,z}^2 \cdot \left(1 + 2 \cdot k_p \cdot I_v\right) = 1303.396 \text{ Pa}$$

Peak velocity pressure

Without traffic: $q_{p.notraffic} = 1.303 \frac{kN}{m^2}$

NA.8.1(4) and N400, chapter 5.4.3.3

- Peak wind velocity at the highest point of driving lane is set to 35m/s

$$v_{p.traffic} := 35 \frac{m}{s}$$

With traffic: $q_{p.traffic} := 0.5 \cdot \rho \cdot v_{p.traffic}^2 = 0.766 \frac{kN}{m^2}$

Wind load on bridge - without traffic load

According to NA.8.3.2(1) can the simplified calculation method be use to find the wind forces if dynamic response analysis is not necessary.

Figur 8.5 $d := 1430 \text{ mm} + 820 \text{ mm}$ (Elgeseter drawings)

Table 8.1 $d_{tot} := d + 0.6 \text{ m} = 2.85 \text{ m} \ll b$

4.5(1) $q_b := \frac{1}{2} \cdot \rho \cdot v_b^2 = 0.423 \frac{kN}{m^2}$

4.5(1) $c_e := \frac{q_{p.notraffic}}{q_b} = 3.085$

Transvere wind force on bridge (x-direction)

8.3.1(1) $c_{fx,0} := 1.3$

8.3.2(1) $C_x := c_e \cdot c_{fx,0} = 4.01$

$A_{ref,x} := 1$ % Even distributed

8.3.2(1) $F_{wx} := \frac{1}{2} \cdot \rho \cdot v_b^2 \cdot C_x \cdot A_{ref,x} = 1.694 \frac{kN}{m^2}$

Fwx is distributed on the reference area: Aref.x described in NS EN 1-4 8.3.1(4) a)

Vertical wind force on bridge deck (z-dir)

According to NA.8.3.3(1), the vertical forcefactor Cf.z on bridgedecks is set to +-0.9

$$c_{f,z} := 0.9$$

$$C_z := c_e \cdot c_{f,z} = 2.776$$

$$A_{ref,z} := 1 \quad \% \text{ Even distributed}$$

$$8.3.2(1) \quad F_{wz} := \frac{1}{2} \cdot \rho \cdot v_b^2 \cdot C_z \cdot A_{ref,z} = 1.173 \frac{kN}{m^2}$$

8.3.3(5) *Exentricity of vertical load is set to b/4 in the x-direction*

Wind load in combination with traffic load

$$4.5(1) \quad c_{e,t} := \frac{q_{p,traffic}}{q_b} = 1.812$$

Wind load in x-dir

$$A_{ref,x} := 1$$

$$8.3.1(1) \quad c_{fx,0} := 1.3$$

$$C_{x,t} := c_{e,t} \cdot c_{fx,0} = 2.356$$

$$8.3.2(1) \quad F_{wx,t} := \frac{1}{2} \cdot \rho \cdot v_b^2 \cdot C_{x,t} \cdot A_{ref,x} = 0.995 \frac{kN}{m^2}$$

Wind load in z-dir

$$A_{ref,z} := 1$$

$$NA \ 8.3.3(1) \quad c_{f,z} := 0.9$$

$$C_{z,t} := c_{e,t} \cdot c_{f,z} = 1.631$$

$$8.3.2(1) \quad F_{wz,t} := \frac{1}{2} \cdot \rho \cdot v_b^2 \cdot C_{z,t} \cdot A_{ref,z} = 0.689 \frac{kN}{m^2}$$

8.3.3(5) : *Exentricity of vertical load is set to b/4 in the x-direction*

Controll according to NA 8.1.4(4)

Controlling that the wind velocity with simultaneously acting traffic load is smaller than the wind velocity without simultaneously acting traffic load.

$$V_{b.0.traf} < V_{b.0}$$

$$v_{p.traf} := 35 \frac{m}{s}$$

$$v_s := \frac{v_{p.traf}}{\sqrt[2]{1 + 2 \cdot k_p \cdot I_v}} = 25.097 \frac{m}{s}$$

$$v_{b.traf} := \frac{v_s}{c_{r.z} \cdot c_0} = 19.927 \frac{m}{s}$$

$$v_{b.0.traf} := \frac{v_{b.traf}}{c_{dir} \cdot c_{season} \cdot c_{alt} \cdot c_{prob}} = 19.927 \frac{m}{s}$$

Kontroll := if $v_{b.0.traf} < v_{b.0}$
 || "OK!"
 else
 || "NOT OK!! "

Kontroll = "OK!"

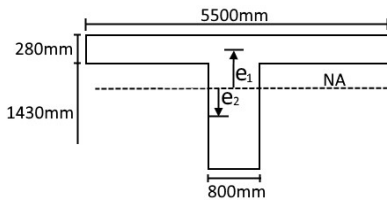
B Calculation of second moment of area, Stadium I

Geomtery

$$A_{plate} := 280 \text{ mm} \cdot 5500 \text{ mm}$$

$$A_{beam} := 1430 \text{ mm} \cdot 800 \text{ mm}$$

$$h := 1710 \text{ mm}$$



$$e_1 := h - NA - \frac{280 \text{ mm}}{2} = 364.4 \text{ mm}$$

$$e_2 := NA - \frac{1430 \text{ mm}}{2} = 490.6 \text{ mm}$$

Calculation of neutral axis, stadium I

$$NA := \frac{\left(A_{plate} \cdot \left(h - 280 \frac{\text{mm}}{2} \right) + A_{beam} \cdot \frac{1430 \text{ mm}}{2} \right)}{A_{plate} + A_{beam}}$$

$$NA = 1205.6 \text{ mm}$$

Calculation of Second moment of area, Iy

$$I_{y,web} := \frac{1}{12} \cdot 800 \text{ mm} \cdot (1430 \text{ mm})^3$$

$$I_{y,flange} := \frac{1}{12} \cdot (5500 \text{ mm}) \cdot (280 \text{ mm})^3$$

$$I_{y,1} := A_{beam} \cdot e_2^2$$

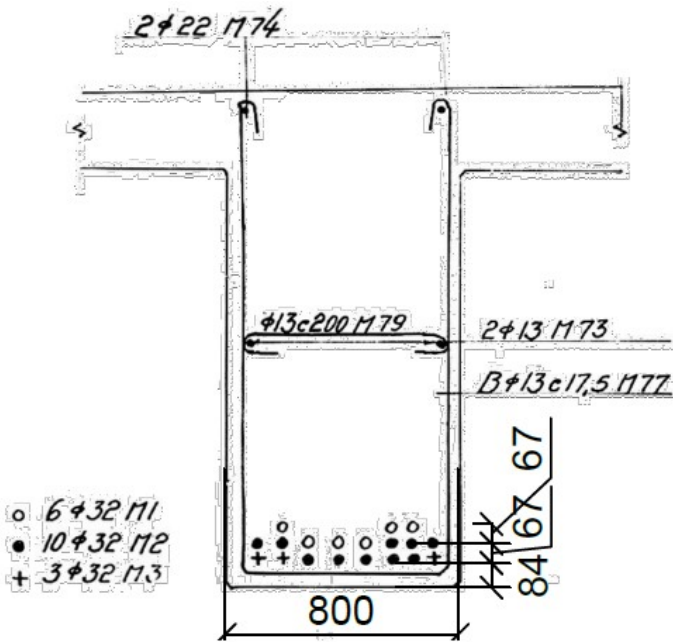
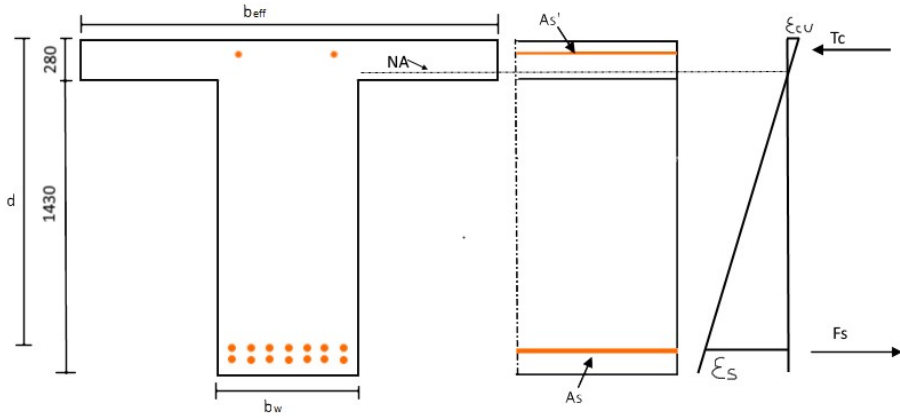
$$I_{y,2} := A_{plate} \cdot e_1^2$$

$$I_y := I_{y,1} + I_{y,2} + I_{y,web} + I_{y,flange}$$

$$I_y = (6.84848 \cdot 10^{11}) \text{ mm}^4$$

C Moment capacity calculations

C.1 Section A-A



Reinforcement:

$$\varepsilon_{su} := 0.01$$

$$\text{St. 52 } f_{yd,\phi32} := 272 \frac{N}{mm^2}$$

$$E_{sk} := 200000 \frac{N}{mm^2}$$

$$A_{\phi32} := \pi \cdot \left(\frac{32 \text{ mm}}{2} \right)^2$$

$$n_{\phi32} := 3 + 10 + 6 = 19$$

$$A_s := n_{\phi32} \cdot A_{\phi32} = 15280.7 \text{ mm}^2$$

$$d_{0,1} := 84 \text{ mm}$$

$$d_{0,2} := 84 \text{ mm} + 67 \text{ mm}$$

$$d_{0,3} := 84 \text{ mm} + 67 \text{ mm} \cdot 2$$

Concrete

$$f_{cd} := 12 \frac{N}{mm^2}$$

$$\varepsilon_{cu} := 0.0035$$

Geometry:

$$h := 1710 \text{ mm}$$

$$b_{eff} := 3775 \text{ mm}$$

$$t_{flange} := 280 \text{ mm}$$

Equation (4.31) in Sørensen (2015),
Betongkonstruksjoner. 2. edition

Calculating d

$$d_0 := \frac{(8 \cdot d_{0,1} + 8 \cdot d_{0,2} + 3 \cdot d_{0,3})}{n_{\phi32}}$$

$$d_0 = 133.4 \text{ mm}$$

$$d := h - d_0 = 1576.632 \text{ mm}$$

Moment capacity, method 1

Assuming under reinforced section:

$$\alpha := \frac{f_{yd,\phi32} \cdot A_s}{0.8 \cdot f_{cd} \cdot b_{eff} \cdot d} = 0.0727$$

$$M_{Rd,1} := 0.8 \cdot \alpha \cdot (1 - (0.4 \cdot \alpha)) \cdot f_{cd} \cdot b_{eff} \cdot d^2$$

Control reinforcement strain:

$$\varepsilon_s := \frac{(1 - \alpha)}{\alpha} \cdot \varepsilon_{cu} = 0.045$$

$$M_{Rd} := \begin{cases} \text{if } \varepsilon_s < \varepsilon_{su} & \text{=} \text{"NOT OK!"} \\ \parallel M_{Rd,1} \\ \text{else} \\ \parallel \text{"NOT OK!"} \end{cases}$$

Reinforcement strain by method 1 too large.
This effect is typical for reinforced T-sections,
described by (Sørensen, 2015) in
Betongkonstruksjoner 2, chapter 4.2.4, page
52, fig 4.11.

Moment capacity, method 2

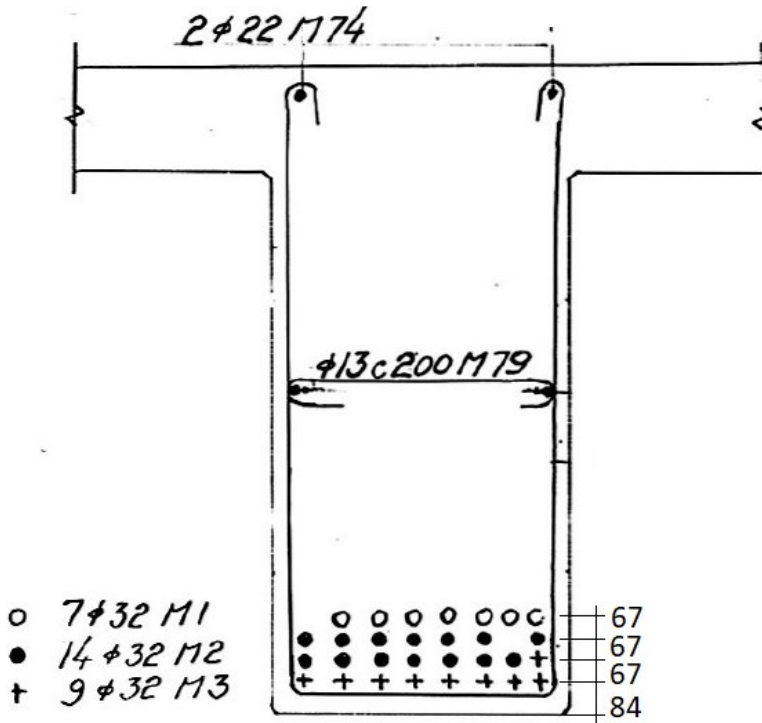
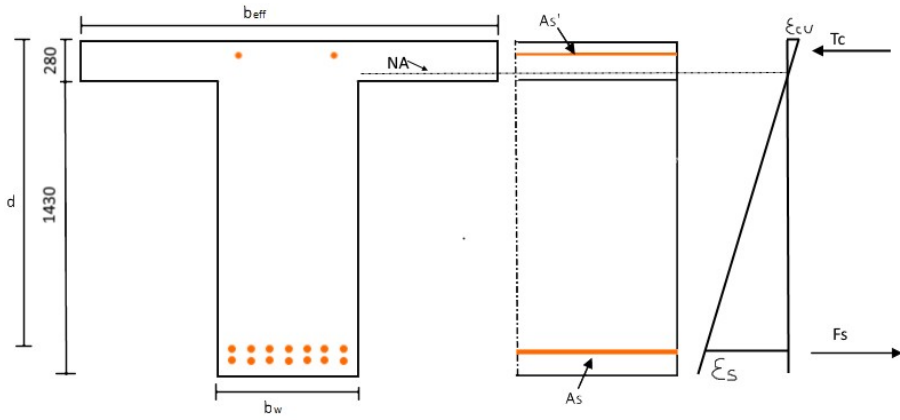
$$M_{Rd,2} := f_{yd,\phi32} \cdot A_s \cdot \left(d - \frac{t_{flange}}{2} \right)$$

Control concrete compression stress:

$$\sigma_{cd} := \frac{M_{Rd,2}}{t_{flange} \cdot b_{eff} \cdot \left(d - \frac{t_{flange}}{2} \right)} = 3.932 \frac{N}{mm^2}$$

$$M_{Rd,2} := \begin{cases} \text{if } \sigma_{cd} < f_{cd} & \text{=} M_{Rd,2} = 5971 \text{ kN} \cdot \text{m} \\ \parallel M_{Rd,2} \\ \text{else} \\ \parallel \text{"NOT OK!"} \end{cases}$$

C.2 Section B-B



Reinforcement:

$$\varepsilon_{su} := 0.01$$

$$\text{St. 52 } f_{yd,\phi32} := 272 \frac{N}{mm^2}$$

$$E_{sk} := 200000 \frac{N}{mm^2}$$

$$A_{\phi32} := \pi \cdot \left(\frac{32 \text{ mm}}{2} \right)^2$$

$$n_{\phi32} := 9 + 14 + 7 = 30$$

$$A_s := n_{\phi32} \cdot A_{\phi32} = 24127.4 \text{ mm}^2$$

$$d_{0,1} := 84 \text{ mm}$$

$$d_{0,2} := 84 \text{ mm} + 67 \text{ mm}$$

$$d_{0,3} := 84 \text{ mm} + 67 \text{ mm} \cdot 2$$

$$d_{0,4} := 84 \text{ mm} + 67 \text{ mm} \cdot 3$$

Concrete

$$f_{cd} := 12 \frac{N}{mm^2}$$

$$\varepsilon_{cu} := 0.0035$$

Geometry:

$$h := 1710 \text{ mm}$$

$$b_{eff} := 4412.5 \text{ mm}$$

$$t_{flange} := 280 \text{ mm}$$

Equation (4.31) in Sørensen (2015),
Betongkonstruksjoner. 2. edition

Calculating d

$$d_0 := \frac{(8 \cdot d_{0,1} + 8 \cdot d_{0,2} + 7 \cdot d_{0,3} + 6 \cdot d_{0,4})}{n_{\phi32}}$$

$$d_0 = 170.5 \text{ mm}$$

$$d := h - d_0 = 1539.467 \text{ mm}$$

Moment capacity, method 1

Assuming under reinforced section:

$$\alpha := \frac{f_{yd,\phi32} \cdot A_s}{0.8 \cdot f_{cd} \cdot b_{eff} \cdot d} = 0.1006$$

$$M_{Rd,1} := 0.8 \cdot \alpha \cdot (1 - (0.4 \cdot \alpha)) \cdot f_{cd} \cdot b_{eff} \cdot d^2$$

Control reinforcement strain:

$$\varepsilon_s := \frac{(1 - \alpha)}{\alpha} \cdot \varepsilon_{cu} = 0.031$$

$$M_{Rd} := \begin{cases} \text{if } \varepsilon_s < \varepsilon_{su} & \text{=} \text{"NOT OK!"} \\ \quad \parallel M_{Rd,1} & \\ \text{else} & \\ \quad \parallel \text{"NOT OK!"} & \end{cases}$$

Reinforcement strain by method 1 too large.
This effect is typical for reinforced T-sections,
described by (Sørensen, 2015) in
Betongkonstruksjoner 2, chapter 4.2.4, page
52, fig 4.11.

Moment capacity, method 2

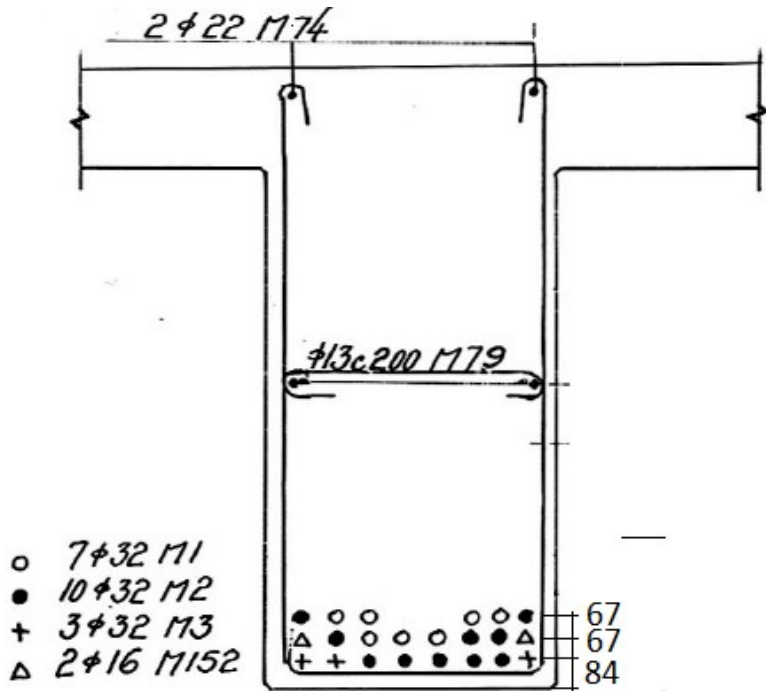
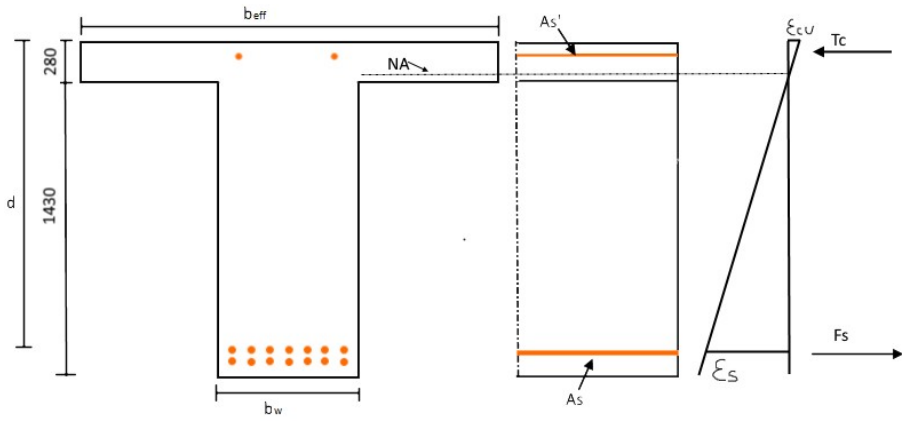
$$M_{Rd,2} := f_{yd,\phi32} \cdot A_s \cdot \left(d - \frac{t_{flange}}{2} \right)$$

Control concrete compression stress:

$$\sigma_{cd} := \frac{M_{Rd,2}}{t_{flange} \cdot b_{eff} \cdot \left(d - \frac{t_{flange}}{2} \right)} = 5.312 \frac{N}{mm^2}$$

$$M_{Rd} := \begin{cases} \text{if } \sigma_{cd} < f_{cd} & M_{Rd} = 9184 \text{ kN} \cdot \text{m} \\ \quad \parallel M_{Rd,2} & \\ \text{else} & \\ \quad \parallel \text{"NOT OK!"} & \end{cases}$$

C.3 Section C-C



Reinforcement:

$$\varepsilon_{su} := 0.01$$

$$\text{St. 52} \quad f_{yd,\phi32} := 272 \frac{N}{mm^2}$$

$$\text{St. 37} \quad f_{yd,\phi16} := 184 \frac{N}{mm^2}$$

$$E_{sk} := 200000 \frac{N}{mm^2}$$

$$A_{\phi32} := \pi \cdot \left(\frac{32 \text{ mm}}{2} \right)^2$$

$$A_{\phi16} := \pi \cdot \left(\frac{16 \text{ mm}}{2} \right)^2$$

$$n_{\phi32} := 3 + 10 + 7 = 20$$

$$n_{\phi16} := 2 = 2$$

$$A_{s,\phi32} := n_{\phi32} \cdot A_{\phi32}$$

$$A_{s,\phi32} = 16085 \text{ mm}^2$$

$$A_{s,\phi16} := n_{\phi16} \cdot A_{\phi16}$$

$$A_{s,\phi16} = 402.1 \text{ mm}^2$$

$$d_{0,1} := 84 \text{ mm}$$

$$d_{0,2} := 84 \text{ mm} + 67 \text{ mm}$$

$$d_{0,3} := 84 \text{ mm} + 67 \text{ mm} \cdot 2$$

Concrete

$$f_{cd} := 12 \frac{N}{mm^2}$$

$$\varepsilon_{cu} := 0.0035$$

Geometry:

$$h := 1710 \text{ mm}$$

$$b_{eff} := 3950 \text{ mm}$$

$$t_{flange} := 280 \text{ mm}$$

Equation (4.31) in Sørensen (2015), Betongkonstruksjoner. 2. edition

Calculating d

$$d_{0,\phi32} := 8 \cdot d_{0,1} + 6 \cdot d_{0,2} + 6 \cdot d_{0,3}$$

$$d_{0,\phi16} := d_{0,2}$$

$$d_0 := \frac{A_{\phi32} \cdot f_{yd,\phi32} \cdot d_{0,\phi32} + A_{\phi16} \cdot f_{yd,\phi16} \cdot 2 \cdot d_{0,\phi16}}{A_{s,\phi32} \cdot f_{yd,\phi32} + A_{s,\phi16} \cdot f_{yd,\phi16}}$$

$$d_0 = 144.4 \text{ mm}$$

$$d := h - d_0 = 1565.6 \text{ mm}$$

Moment capacity, method 1

Assuming under reinforced section:

$$\alpha := \frac{(f_{yd,\phi32} \cdot A_{s,\phi32} + f_{yd,\phi16} \cdot A_{s,\phi16})}{0.8 \cdot f_{cd} \cdot b_{eff} \cdot d} = 0.0749$$

$$M_{Rd} := 0.8 \cdot \alpha \cdot (1 - (0.4 \cdot \alpha)) \cdot f_{cd} \cdot b_{eff} \cdot d^2$$

Control reinforcement strain:

$$\varepsilon_s := \frac{(1 - \alpha)}{\alpha} \cdot \varepsilon_{cu} = 0$$

$$M_{Rd,1} := \begin{cases} \text{if } \varepsilon_s < \varepsilon_{su} & \text{=} \text{"NOT OK!"} \\ \parallel M_{Rd} & \\ \text{else} & \\ \parallel \text{"NOT OK!"} & \end{cases}$$

Reinforcement strain by method 1 too large. This effect is typical for reinforced T-sections, described by (Sørensen, 2015) in Betongkonstruksjoner 2, chapter 4.2.4, page 52, fig 4.11.

Moment capacity, method 2

$$M_{Rd,2} := (f_{yd,\phi32} \cdot A_{s,\phi32} + f_{yd,\phi16} \cdot A_{s,\phi16}) \cdot \left(d - \frac{t_{flange}}{2} \right)$$

Control concrete compression stress:

$$\sigma_{cd} := \frac{M_{Rd,2}}{t_{flange} \cdot b_{eff} \cdot \left(d - \frac{t_{flange}}{2} \right)} = 4.02 \frac{N}{mm^2}$$

$$M_{Rd} := \begin{cases} \text{if } \sigma_{cd} < f_{cd} & \text{=} M_{Rd} = 6343 \text{ kN} \cdot \text{m} \\ \parallel M_{Rd,2} & \\ \text{else} & \\ \parallel \text{"NOT OK!"} & \end{cases}$$

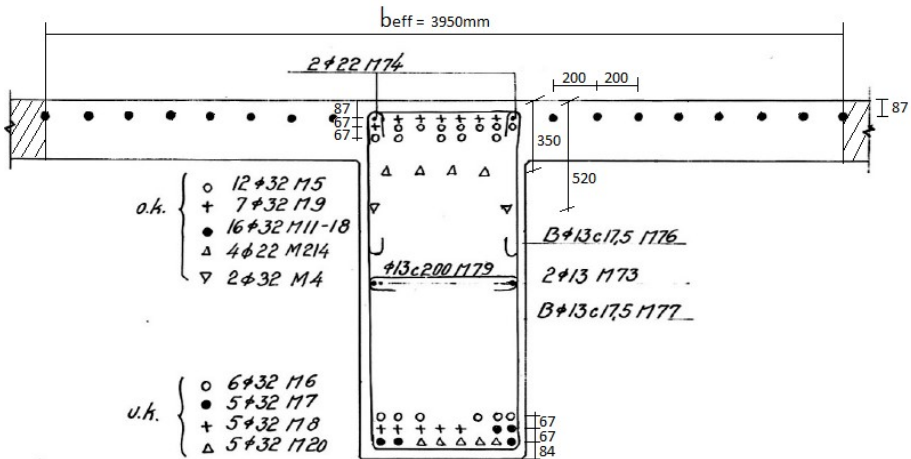
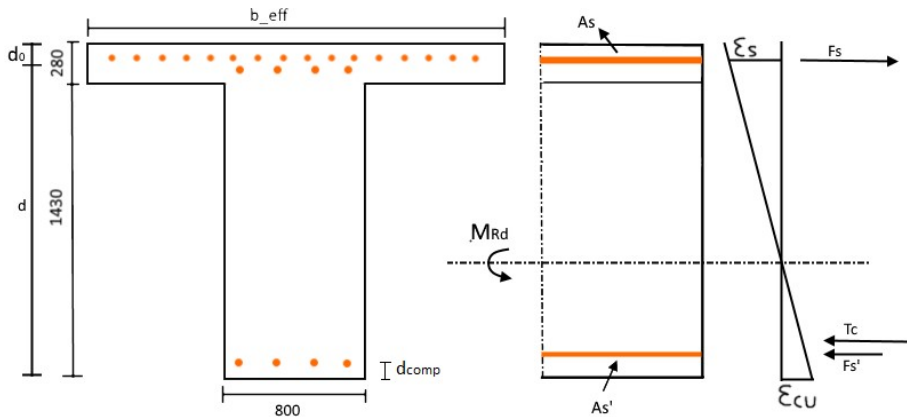
C.4 Section D-D

Sørensen (2015), *Betongkonstruksjoner*. 2. edition, chapter 4.2.4 (page. 53)

- If the flange is on the tensile side, the cross section is calculated as rectangular with the width equal to the the web- width, b_w . All of the main bars within the effective flange width b_{eff} are included as the effective tensile reinforcement.

NS 3437 2003 chapter 9.5

- If the flange is on the tensile side, all the tensile reinforcment inside the effective flange width of the adherent compression flange is included.



Reinforcement

$$\varepsilon_{su} := 0.01$$

$$\text{St. 52} \quad f_{yd,\phi32} := 272 \frac{N}{mm^2}$$

$$\text{St. 37} \quad f_{yd,\phi22} := 184 \frac{N}{mm^2}$$

$$E_{sk} := 200000 \frac{N}{mm^2}$$

$$A_{\phi32} := \pi \cdot \left(\frac{32 \text{ mm}}{2} \right)^2$$

$$A_{\phi22} := \pi \cdot \left(\frac{22 \text{ mm}}{2} \right)^2$$

Tensile reinf:

$$n_{\phi32} := 22 + 8 + 5 + 2 = 37$$

$$n_{\phi22} := 6$$

$$A_{s,\phi32} := A_{\phi32} \cdot n_{\phi32} = 29757 \text{ mm}^2$$

$$A_{s,\phi22} := A_{\phi22} \cdot n_{\phi22} = 2281 \text{ mm}^2$$

$$d_{0,1} := 87 \text{ mm}$$

$$d_{0,2} := 87 \text{ mm} + 67 \text{ mm}$$

$$d_{0,3} := 87 \text{ mm} + 67 \text{ mm} \cdot 2$$

$$d_{0,4} := 350 \text{ mm}$$

$$d_{0,5} := 520 \text{ mm}$$

Comp reinf:

$$n'_{\phi32} := 8 + 7 + 6$$

$$d_{comp,1} := 84 \text{ mm}$$

$$d_{comp,2} := 84 \text{ mm} + 67 \text{ mm}$$

$$d_{comp,3} := 84 \text{ mm} + 67 \text{ mm} \cdot 2$$

$$A'_s := n'_{\phi32} \cdot A_{\phi32} = 16889 \text{ mm}^2$$

Concrete

$$f_{cd} := 12 \frac{N}{mm^2}$$

Geometry:

$$h := 1710 \text{ mm}$$

$$b_w := 800 \text{ mm}$$

$$t := 280 \text{ mm}$$

Calculating d

$$d_0 n_{\phi32} := 22 \cdot d_{0,1} + 8 \cdot d_{0,2} + 5 \cdot d_{0,3} + 2 \cdot d_{0,5}$$

$$d_0 n_{\phi22} := 4 \cdot d_{0,4} + 2 \cdot d_{0,1}$$

$$d_0 := \frac{(A_{\phi32} \cdot f_{yd,\phi32} \cdot d_0 n_{\phi32} + A_{\phi22} \cdot f_{yd,\phi22} \cdot d_0 n_{\phi22})}{n_{\phi32} \cdot f_{yd,\phi32} \cdot A_{\phi32} + n_{\phi22} \cdot f_{yd,\phi22} \cdot A_{\phi22}}$$

$$d_0 = 148.882 \text{ mm}$$

$$d := h - d_0 = (1.561 \cdot 10^3) \text{ mm}$$

Calculating h'

$$d_{comp} := \frac{(8 \cdot d_{comp,1} + 7 \cdot d_{comp,2} + 6 \cdot d_{comp,3})}{8 + 7 + 6}$$

$$d_{comp} = 144.619 \text{ mm}$$

$$h' := d - d_{comp} = 1416.5 \text{ mm}$$

Tensile reinforcement to balance compression reinforcement:

$$A_{s,bal} := A'_s = 16889.202 \text{ mm}^2$$

Assuming under-reinforced section

Equation 4.18 Sørensen

$$\alpha := \frac{(f_{yd,\phi32} \cdot n_{\phi32} \cdot A_{\phi32} + f_{yd,\phi22} \cdot n_{\phi22} \cdot A_{\phi22} - A_{s,bal} \cdot f_{yd,\phi32})}{0.8 \cdot f_{cd} \cdot b_w \cdot d}$$

$$\alpha = 0.327$$

$$M_{Rd,concrete.zone} := 0.8 \cdot \alpha \cdot (1 - (0.4 \cdot \alpha)) \cdot f_{cd} \cdot b_w \cdot d^2$$

$$M_{Rd,concrete.zone} = 5318.963 \text{ kN} \cdot \text{m}$$

Equation 4.30 Sørensen

$$\Delta M_{Rd} := A_{s,bal} \cdot f_{yd,\phi32} \cdot h'$$

$$\Delta M_{Rd} = 6507.2 \text{ kN} \cdot \text{m}$$

Total moment capacity

$$M_{Rd} := M_{Rd,concrete.zone} + \Delta M_{Rd} = 11826 \text{ kN} \cdot \text{m}$$

Tensile reinforcement strain control

$$\varepsilon_s := \frac{(1 - \alpha)}{\alpha} \cdot 0.0035 = 0.0072$$

$$\text{Control}_1 := \begin{cases} \text{if } \varepsilon_s < \varepsilon_{su} \\ \quad \parallel \text{ "OK!"} \\ \quad \text{else} \\ \quad \parallel \text{ "NOT OK!!"} \end{cases}$$

$$\text{Control}_1 = \text{"OK!"}$$

Compression yielding control

$$\varepsilon_{yd} := \frac{f_{yd,\phi32}}{E_{sk}} = 0.00136$$

$$\varepsilon_s' := \frac{(\alpha \cdot d - d_{comp})}{\alpha \cdot d} \cdot 0.0035 = 0.0025$$

$$\text{Control}_2 := \begin{cases} \text{if } \varepsilon_s' > \varepsilon_{yd} \\ \quad \parallel \text{ "OK!"} \\ \quad \text{else} \\ \quad \parallel \text{ "NOT OK!!"} \end{cases}$$

$$\text{Control}_2 = \text{"OK!"}$$

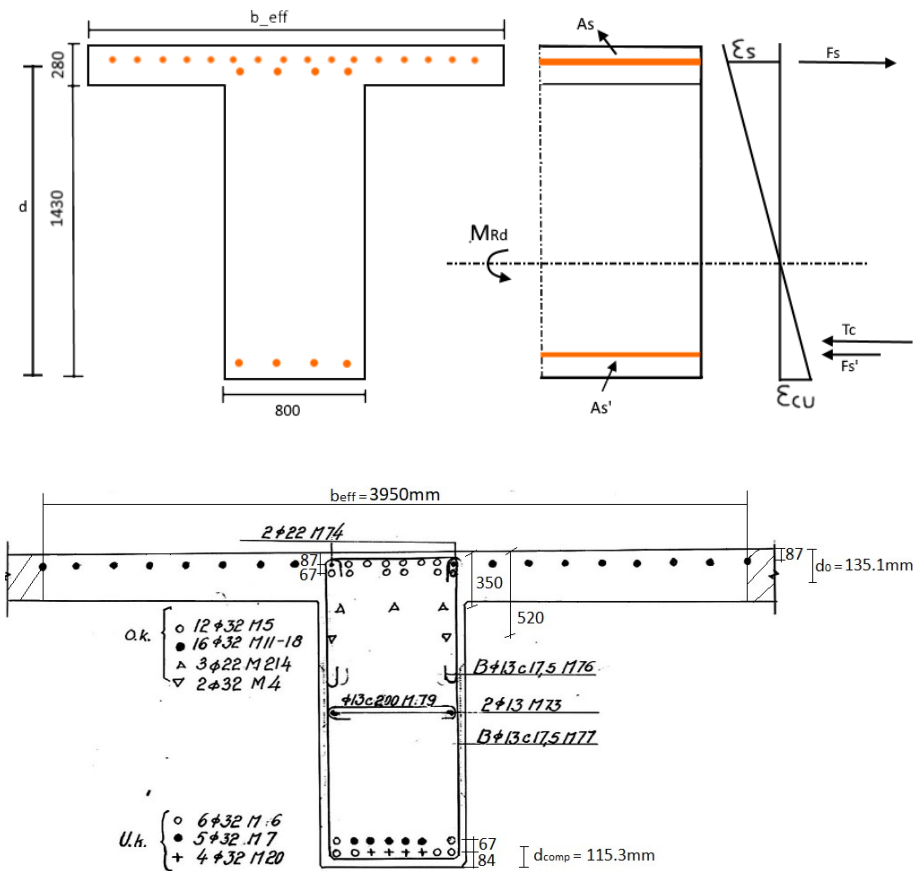
C.5 Section E-E

Sørensen (2015), *Betongkonstruksjoner*. 2. edition, chapter 4.2.4 (page. 53)

- If the flange is on the tensile side, the cross section is calculated as rectangular with the width equal to the the web- width, b_w . All of the main bars within the effective flange width b_{eff} are included as the effective tensile reinforcement.

NS 3437 2003 chapter 9.5

- If the flange is on the tensile side, all the tensile reinforcement inside the effective flange width of the adherent compression flange are included.



Reinforcement

$$\varepsilon_{su} := 0.01$$

$$\text{St. 52} \quad f_{yd,\phi32} := 272 \frac{N}{mm^2}$$

$$\text{St. 37} \quad f_{yd,\phi22} := 184 \frac{N}{mm^2}$$

$$E_{sk} := 200000 \frac{N}{mm^2}$$

$$A_{\phi32} := \pi \cdot \left(\frac{32 \text{ mm}}{2} \right)^2$$

$$A_{\phi22} := \pi \cdot \left(\frac{22 \text{ mm}}{2} \right)^2$$

Tensile reinf:

$$n_{\phi32} := 22 + 6 + 2 = 30$$

$$n_{\phi22} := 5$$

$$A_{s,\phi32} := A_{\phi32} \cdot n_{\phi32} = 24127.4 \text{ mm}^2$$

$$A_{s,\phi22} := A_{\phi22} \cdot n_{\phi22} = 1900.7 \text{ mm}^2$$

$$d_{0,1} := 87 \text{ mm}$$

$$d_{0,2} := 87 \text{ mm} + 67 \text{ mm}$$

$$d_{0,3} := 350 \text{ mm}$$

$$d_{0,4} := 520 \text{ mm}$$

Comp reinf:

$$n'_{\phi32} := 8 + 7$$

$$d_{comp,1} := 84 \text{ mm}$$

$$d_{comp,2} := 84 \text{ mm} + 67 \text{ mm}$$

$$A'_s := n'_{\phi32} \cdot A_{\phi32} = 12063.7 \text{ mm}^2$$

Concrete

$$f_{cd} := 12 \frac{N}{mm^2}$$

Geometry:

$$h := 1710 \text{ mm}$$

$$b_w := 800 \text{ mm}$$

$$t := 280 \text{ mm}$$

Calculating lever arm, d

$$d_0 n_{\phi32} := 22 \cdot d_{0,1} + 6 \cdot d_{0,2} + 2 \cdot d_{0,4}$$

$$d_0 n_{\phi22} := 3 \cdot d_{0,3} + 2 \cdot d_{0,1}$$

$$d_0 := \frac{(A_{\phi32} \cdot f_{yd,\phi32} \cdot d_0 n_{\phi32} + A_{\phi22} \cdot f_{yd,\phi22} \cdot d_0 n_{\phi22})}{n_{\phi32} \cdot f_{yd,\phi32} \cdot A_{\phi32} + n_{\phi22} \cdot f_{yd,\phi22} \cdot A_{\phi22}}$$

$$d_0 = 135.112 \text{ mm}$$

$$d := h - d_0 = (1.575 \cdot 10^3) \text{ mm}$$

Calculating h'

$$d_{comp} := \frac{(8 \cdot d_{comp,1} + 7 \cdot d_{comp,2})}{8 + 7}$$

$$d_{comp} = 115.267 \text{ mm}$$

$$h' := d - d_{comp} = 1459.6 \text{ mm}$$

Tensile reinforcement to balance compression reinforcement:

$$A_{s,bal} := A'_s = 12063.716 \text{ mm}^2$$

Assuming under-reinforced section

Equation 4.18 Sørensen

$$\alpha := \frac{(f_{yd,\phi32} \cdot n_{\phi32} \cdot A_{\phi32} + f_{yd,\phi22} \cdot n_{\phi22} \cdot A_{\phi22} - A_{s,bal} \cdot f_{yd,\phi32})}{0.8 \cdot f_{cd} \cdot b_w \cdot d}$$

$$\alpha = 0.3002$$

$$M_{Rd,concrete.zone} := 0.8 \cdot \alpha \cdot (1 - (0.4 \cdot \alpha)) \cdot f_{cd} \cdot b_w \cdot d^2$$

$$M_{Rd,concrete.zone} = 5031.807 \text{ kN} \cdot \text{m}$$

Equation 4.30 Sørensen

$$\Delta M_{Rd} := A_{s,bal} \cdot f_{yd,\phi32} \cdot h'$$

$$\Delta M_{Rd} = 4789.501 \text{ kN} \cdot \text{m}$$

Total moment capacity

$$M_{Rd} := M_{Rd,concrete.zone} + \Delta M_{Rd} = 9821 \text{ kN} \cdot \text{m}$$

Tensile reinforcement strain control

$$\varepsilon_s := \frac{(1 - \alpha)}{\alpha} \cdot 0.0035 = 0.0082$$

$$Control_1 := \begin{cases} \text{if } \varepsilon_s < \varepsilon_{su} \\ \quad \text{“OK!”} \\ \text{else} \\ \quad \text{“NOT OK!”} \end{cases}$$

$$Control_1 = \text{“OK!”}$$

$$\varepsilon_{yd} := \frac{f_{yd,\phi32}}{E_{sk}} = 0.00136$$

Compression yielding control

$$\varepsilon_s' := \frac{(\alpha \cdot d - d_{comp})}{\alpha \cdot d} \cdot 0.0035 = 0.0026$$

$$Control_2 := \begin{cases} \text{if } \varepsilon_s' > \varepsilon_{yd} \\ \quad \text{“OK!”} \\ \text{else} \\ \quad \text{“NOT OK!”} \end{cases}$$

$$Control_2 = \text{“OK!”}$$

**D Verification of moments and shear forces from Robot
with hand calculations**

D.1 Dead load

Formulas for bending moment and shear forces are based on Byggforsk formulas.

Dead load line load:

$$q_g := 101.3 \frac{\text{kN}}{\text{m}}$$

Length internal spans

$$L_{int} := 22.5 \text{ m}$$

Length first span: (1-2)

$$L_{first} := 21.25 \text{ m}$$

Length last span (9-10)

$$L_{last} := 21.25 \text{ m}$$

Moment:

Internal field sections (2-3 to 8-9):

$$M_{g,field} := \frac{q_g \cdot L_{int}^2}{24} = 2137 \text{ kN} \cdot \text{m}$$

First field section (1-2)

$$M_{g,field.1.2} := \frac{q_g \cdot L_{first}^2}{24} = 1906 \text{ kN} \cdot \text{m}$$

Last field section (9-10)

$$M_{g,field.9.10} := \frac{9 \cdot q_g \cdot L_{last}^2}{128} = 3216 \text{ kN} \cdot \text{m}$$

Internal supports (3-8):

$$M_{g,supports} := \frac{-q_g \cdot L_{int}^2}{12} = -4274 \text{ kN} \cdot \text{m}$$

Shear

Internal supports (2-8)

$$V_{g,int} := \frac{q_g \cdot L_{int}}{2} = 1140 \text{ kN}$$

First support (axis 1)

$$V_{g.1} := \frac{q_g \cdot L_{first}}{2} = 1076 \text{ kN}$$

Support axis 9

$$V_{g.9} := \frac{5 \cdot q_g \cdot L_{last}}{8} = 1345 \text{ kN}$$

D.2 Thermal load

Vertical temperature difference components

Height cross- section:

$$h := 1710 \text{ mm}$$

Thermal expansion coeff:

$$\alpha_T := \frac{10^{-5}}{C}$$

Vertical heat difference comp:

$$T_{heat} := 12.75 \text{ C}$$

Verical cold difference comp

$$T_{cold} := -8 \text{ C}$$

Second moment of area,

Stadium 2, internal T-beam:

$$I_y := 6.84848 \cdot 10^{11} \text{ mm}^4$$

E-modulus concrete
superstructure:

$$E_{c.25} := 24952 \frac{N}{\text{mm}^2}$$

Bending stiffness stadium 2:

$$EI_{2.T.beam} := I_y \cdot E_{c.25}$$

$$EI_{2.T.beam} = (1.709 \cdot 10^{16}) \text{ N} \cdot \text{mm}^2$$

Internal field sections (2-3 to 8-9):

Vertical heat difference component:

- (Top side warmer)

Curvature due to vertical heat
component:

$$\kappa_{T.heat} := \frac{\alpha_T \cdot T_{heat}}{h} = 0.000075 \frac{1}{m}$$

$$M_{T.heat} := EI_{2.T.beam} \cdot \kappa_{T.heat}$$

$$M_{T.heat} = 1274 \text{ kN} \cdot \text{m}$$

Vertical cold difference component:

- (Top side colder)

Curvature due to vertical cold
component:

$$\kappa_{T.cold} := \frac{\alpha_T \cdot T_{cold}}{h} = -0.000047 \frac{1}{m}$$

$$M_{T.cold} := EI_{2.T.beam} \cdot \kappa_{T.cold}$$

$$M_{T.cold} = -799 \text{ kN} \cdot \text{m}$$

Even temperature expansion component

Thermal expansion coeff:

$$\alpha_T := \frac{10^{-5}}{C}$$

Even temperature expansion

$$T_{exp} := 23 \text{ } C$$

Diameter columns:

$$D := 800 \text{ } mm$$

Second moment of area, column Stadium 2:

$$I_{y.column} := \frac{\pi}{64} \cdot D^4 = (2.011 \cdot 10^{10}) \text{ } mm^4$$

E-modulus columns (Longtime)

$$E_{c.long.30} := 8317 \frac{N}{mm^2}$$

Bending stiffness stadium 2:

$$EI_{2.column7} := I_{y.column} \cdot E_{c.long.30}$$
$$EI_{2.column7} = (1.672 \cdot 10^{14}) \text{ } N \cdot mm^2$$

Length internal spans superstructure

$$L_{int} := 22.5 \text{ } m$$

Length first span superstructure: (1-2)

$$L_{first} := 21.25 \text{ } m$$

Length internal columns:

$$L_{int.columns} := 14.5 \text{ } m$$

Control column 7

Length to column 7:

$$L := L_{first} + 5 \cdot L_{int} = 134 \text{ } m$$

Elongation at column 7

$$\Delta L_7 := L \cdot \alpha_T \cdot T_{exp} = 31 \text{ } mm$$

Moment from support in axis 7

$$M_7 := \frac{6 \cdot EI_{2.column7}}{L_{int.columns}^2} \cdot \Delta L_7$$

$$M_7 = 147 \text{ } kN \cdot m$$

D.3 Alkali- Silica expansion load

Vertical ASR difference component (more expansion in top plate)

Height cross- section:

$$h := 1710 \text{ mm}$$

Thermal expansion coeff:

$$\alpha_T := \frac{10^{-5}}{C}$$

Curvature:

$$\kappa_{ASR} := \frac{0.000468}{m}$$

Second moment of area,

Stadium 2, internal T-beam:

$$I_y := 6.84848 \cdot 10^{11} \text{ mm}^4$$

E-modulus concrete
superstructure (longtime)

$$E_{c.25} := \frac{24952}{3} \frac{N}{\text{mm}^2}$$

Bending stiffness stadium 2:

$$EI_{2.T.beam} := I_y \cdot E_{c.25}$$
$$EI_{2.T.beam} = (5.696 \cdot 10^{15}) \text{ N} \cdot \text{mm}^2$$

Internal field sections (2-3 to 8-9):

$$M_{T.heat} := EI_{2.T.beam} \cdot \kappa_{ASR}$$

$$M_{T.heat} = 2666 \text{ kN} \cdot \text{m}$$

Even ASR expansion component

Length of bridge:

$$L_{bridge} := 200 \text{ m}$$

Elongation of bridge (axis 10)

$$\Delta L_{bridge} := 180 \text{ mm}$$

Diameter columns:

$$D := 800 \text{ mm}$$

Second moment of area, column Stadium 2:

$$I_{y.column} := \frac{\pi}{64} \cdot D^4 = (2.011 \cdot 10^{10}) \text{ mm}^4$$

E-modulus columns (Longtime)

$$E_{c.long.30} := 8317 \frac{\text{N}}{\text{mm}^2}$$

Bending stiffness stadium 2:

$$EI_2 := I_{y.column} \cdot E_{c.long.30}$$
$$EI_2 = (1.672 \cdot 10^{14}) \text{ N} \cdot \text{mm}^2$$

Length internal spans superstructure

$$L_{int} := 22.5 \text{ m}$$

Length first span superstructure: (1-2)

$$L_{first} := 21.25 \text{ m}$$

Length internal columns:

$$L_{int.columns} := 14.5 \text{ m}$$

Control column 7

Length to column 7:

$$L_7 := L_{first} + 5 \cdot L_{int} = 134 \text{ m}$$

Elongation at column 7

$$\Delta L_7 := \frac{L_7}{L_{bridge}} \cdot \Delta L_{bridge} = 120 \text{ mm}$$

Moment from support in axis 7

$$M_7 := \frac{6 \cdot EI_2}{L_{int.columns}^2} \cdot \Delta L_7$$

$$M_7 = 574 \text{ kN} \cdot \text{m}$$

E Control of strain state in field section C-C at time step 42 from DIANA 2D model with hand calculations

Step 1

Betongkonstruksjoner 2
(Sørensen, 2015), chapter
5.2.7

Cross section geometry:

$$h := 1710 \text{ mm}$$

$$b := 800 \text{ mm}$$

$$b_f := 5500 \text{ mm} - b$$

$$d_0 := 100 \text{ mm}$$

$$d := h - d_0 = 1610 \text{ mm}$$

$$t_{plate} := 280 \text{ mm}$$

$$d' := 100 \text{ mm}$$

Reinforcement

$$E_s := 200000 \frac{\text{N}}{\text{mm}^2}$$

$$A_s := 16482 \text{ mm}^2$$

$$A_s' := 2 \cdot \pi \cdot \left(\frac{22}{2} \text{ mm} \right)^2$$

$$A_s' = 760.265 \text{ mm}^2$$

Concrete

$$E_{cm} := 8317 \frac{\text{N}}{\text{mm}^2}$$

Finding neutral axis, (stadium 2)

$$\rho := \frac{A_s}{b \cdot d}$$

$$\mu' := \frac{(\eta - 1)}{\eta} \cdot \frac{A_s'}{b \cdot d}$$

$$\eta := \frac{E_s}{E_{cm}}$$

$$f := \frac{(t_{plate} \cdot b_f)}{b \cdot d}$$

$$A := \eta \cdot (\rho + \mu') + f$$

$$B := \eta \cdot \mu' \cdot \left(1 - \frac{d'}{d} \right) + f \cdot \left(1 - \frac{t_{plate}}{2 \cdot d} \right)$$

$$\alpha := \sqrt[2]{A^2 + 2 \cdot A - 2 \cdot B - A} = 0.269$$

$$NA := h - \alpha \cdot d = 1277 \text{ mm}$$

Bending stiffness, (EI)_{II} (stadium 2)

$$\xi := 1 + \frac{b_f}{b} \cdot \left(\frac{t_{plate}}{\alpha \cdot d} \right)^3 - 3 \cdot \frac{b_f}{b} \cdot \left(\frac{t_{plate}}{\alpha \cdot d} \right)^2 + 3 \cdot \frac{b_f}{b} \cdot \left(\frac{t_{plate}}{\alpha \cdot d} \right)$$

$$I_{\beta\beta} := \xi \cdot \frac{(b \cdot (\alpha \cdot d)^3)}{3} = (1.433 \cdot 10^{11}) \text{ mm}^4$$

$$I_s := A_s \cdot (1 - \alpha)^2 \cdot d^2 = (2.283 \cdot 10^{10}) \text{ mm}^4$$

$$I_s' := A_s' \cdot (\alpha \cdot d - d')^2 - \frac{E_{cm}}{E_s} \cdot A_s' \cdot (\alpha \cdot d - d')^2$$

$$I_s' = (8.082 \cdot 10^7) \text{ mm}^4$$

$$EI_{II} := E_{cm} \cdot I_{\beta\beta} + E_s \cdot (I_s + I_s') = (5.774 \cdot 10^{15}) \text{ N} \cdot \text{mm}^2$$

Step 2

Parameters Load model 1

$$\varepsilon_{A1} := -0.00059$$

$$e_s := (1 - \alpha) \cdot d = 1177 \text{ mm}$$

$$e_{s'} := (\alpha \cdot d - d') = 333 \text{ mm}$$

Parameters Load model 1

$$\varepsilon_{A2} := 0.00059$$

$$e_{plate} := \left(\alpha \cdot d - \frac{t_{plate}}{2} \right) = 293 \text{ mm}$$

Internal load model 1 (A1)

$$F_{s,A1} := E_s \cdot A_s \cdot \varepsilon_{A1} = -1944.9 \text{ kN}$$

$$F'_{s,A1} := E_s \cdot A'_s \cdot \varepsilon_{A1} = -89.7 \text{ kN}$$

$$N_{A1} := F_{s,A1} + F'_{s,A1} = -2034.6 \text{ kN}$$

$$M_{A1} := F_{s,A1} \cdot e_s - F'_{s,A1} \cdot e_{s'} = -2259.2 \text{ kN} \cdot \text{m}$$

Internal load model 2 (A2)

$$F_{c,A2} := 5500 \text{ mm} \cdot t_{plate} \cdot E_{cm} \cdot \varepsilon_{A2} = 7556.8 \text{ kN}$$

$$N_{A2} := F_{c,A2} = 7556.8 \text{ kN}$$

$$M_{A2} := -F_{c,A2} \cdot e_{plate} = -2214.4 \text{ kN} \cdot \text{m}$$

Step 3

Moment from external loads:

Dead load moment

$$M_g := 2141 \text{ kN} \cdot \text{m}$$

External ASR moment

$$M_i := (1929) \text{ kN} \cdot \text{m}$$

Normal

$$M_{norm.ext} := M_g + M_i$$

Normal: (withouth load factors)

$$M_{normal} := M_{A1} + M_{A2} + M_{norm.ext} = -403.6 \text{ kN} \cdot \text{m}$$

$$N_{normal} := N_{A1} + N_{A2} = 5522.2 \text{ kN}$$

Index notation

$$M := M_{normal}$$

$$N := N_{normal}$$

Step 4

Moment bending strain

$$M = -403.6 \text{ kN} \cdot \text{m}$$

$$K := \frac{M}{EI_{II}}$$

$$K = -0.00007 \frac{1}{\text{m}}$$

$$\varepsilon_{c.M} := -K \cdot \alpha \cdot d$$

$$\varepsilon_{s'.M} := -K \cdot (\alpha \cdot d - d')$$

$$\varepsilon_{s.M} := K \cdot (1 - \alpha) \cdot d$$

$$\varepsilon_{h_0.M} := K \cdot NA \quad \% \text{ h}=0$$

$$\varepsilon_{f.M} := -K \cdot (\alpha \cdot d - t_{plate})$$

$$\varepsilon_{c.avg.M} := \frac{(\varepsilon_{c.M} + \varepsilon_{f.M})}{2}$$

Moment control parameters: (Not including non cracked beam contribution)

$$e_s = 1177 \text{ mm}$$

$$e_{s'} = 333 \text{ mm}$$

$$e_{plate} = 293 \text{ mm}$$

Axial strain

Normal force

$$N = 5522.2 \text{ kN}$$

Area plate

$$A_{plate} := t_{plate} \cdot (b_f + b)$$

Area non cracked beam %

$$A_{cz.b} := b \cdot (\alpha \cdot d - t_{plate})$$

Strain

$$\varepsilon_N := \frac{N}{(A_{s'} + A_s) \cdot E_s + (A_{plate} + A_{cz.b}) \cdot E_{cm}}$$

$$\varepsilon_N = 0.00032$$

Forces due to Moment, M

Concrete compression zone

$$F_{c.M.plate} := \varepsilon_{c.avg.M} \cdot E_{cm} \cdot (b + b_f) \cdot t_{plate}$$

$$F_{c.M.beam} := \frac{\varepsilon_{f.M}}{2} \cdot E_{cm} \cdot b \cdot (\alpha \cdot d - t_{plate})$$

$$F_{c.M} := F_{c.M.plate} + F_{c.M.beam}$$

$$F_{c.M} = 267.8 \text{ kN}$$

Tensile reinforcement

$$F_{s.M} := A_s \cdot E_s \cdot \varepsilon_{s.M} = -271.2 \text{ kN}$$

Compression reinforcement

$$F_{s'.M} := A_{s'} \cdot E_s \cdot \varepsilon_{s'.M} = 3.54 \text{ kN}$$

Moment control: OK!

$$M_{control} := F_{s.M} \cdot e_s - F_{c.M.plate} \cdot e_{plate} - F_{s'.M} \cdot e_{s'}$$

$$M_{control} = -397.251 \text{ kN} \cdot \text{m}$$

Forces due to Axial force, N

Tensile reinforcement

$$F_{s.N} := A_s \cdot E_s \cdot \varepsilon_N = 1053.8 \text{ kN}$$

Comp reinforcement

$$F_{s'.N} := A_{s'} \cdot E_s \cdot \varepsilon_N = 48.6 \text{ kN}$$

Concrete compression zone

$$F_{c.N} := E_{cm} \cdot \varepsilon_N \cdot (A_{plate} + A_{cz.b})$$

$$F_{c.N} = 4419.9 \text{ kN}$$

Axial force control OK!

$$N_{control} := F_{s.N} + F_{s'.N} + F_{c.N}$$

$$N_{control} = 5522.2 \text{ kN}$$

Step 5

Normal

$$M_{section.normal} := M_{norm.ext} = 4070 \text{ kN} \cdot \text{m}$$

Solution: Apply internal forces (strains) from Load model 1 (A1) and Load model 2 (A2) with opposite direction to the fictitious section forces to achieve equilibrium with external forces and moment.

Parameters Load model 1

$$\varepsilon_{A1} = -0.00059$$

$$F_{s.A1} = -1944.876 \text{ kN}$$

$$F'_{s.A1} = -89.711 \text{ kN}$$

Parameters Load model 2

$$\varepsilon_{A2} = 0.00059$$

$$F_{c.A2} = 7556.8 \text{ kN}$$

Forces

$$F_{s.end} := F_{s.N} + F_{s.M} - F_{s.A1} = 2727.4 \text{ kN}$$

$$F_{c.end} := F_{c.N} + F_{c.M} - F_{c.A2} = -2869.1 \text{ kN}$$

$$F'_{s.end} := F'_{s.N} + F'_{s.M} - F'_{s.A1} = 141.858 \text{ kN}$$

$$N_{control2} := F_{s.end} + F_{c.end} + F'_{s.end} = 0.1472 \text{ kN OK!}$$

Total stress- causing strain: concrete

Plate

$$\varepsilon_{c.global} := \varepsilon_N + \varepsilon_{c.M} - \varepsilon_{A1} = 9.399 \cdot 10^{-4}$$

$$\varepsilon_{c.stress.strain} := \varepsilon_N + \varepsilon_{c.M} - \varepsilon_{A2} = -0.00024$$

$$\varepsilon_{f.stress.strain.plate} := \varepsilon_N + \varepsilon_{f.M} - \varepsilon_{A2} = -0.00026$$

Plot parameters [Colorplot : blue](#)

$$\varepsilon_{plate.stress.causing.strain.normal} := \begin{bmatrix} \varepsilon_{c.global} \\ \varepsilon_{c.stress.strain} \\ \varepsilon_{f.stress.strain.plate} \end{bmatrix}$$

$$h_{c.stress.strain.plate} := \begin{bmatrix} h \\ h \\ h - t_{plate} \end{bmatrix} = \begin{bmatrix} 1710 \\ 1710 \\ 1430 \end{bmatrix} \text{ mm}$$

Original non cracked part of beam

$$\varepsilon_{f.stress.strain.beam} := \varepsilon_N + \varepsilon_{f.M} = 0.00033$$

$$\varepsilon_{NA.stress.strain} := \varepsilon_N = 0.00032$$

Plot parameters: _____ Colorplot: purple

$$\varepsilon_{beam.stress.causing.strain.normal} := \begin{bmatrix} \varepsilon_{f.stress.strain.plate} \\ \varepsilon_{f.stress.strain.beam} \\ \varepsilon_{NA.stress.strain} \end{bmatrix}$$

$$h_{c.stress.strain.noncrackedbeam} := \begin{bmatrix} h - t_{plate} \\ h - t_{plate} \\ NA \end{bmatrix} = \begin{bmatrix} 1430 \\ 1430 \\ 1277 \end{bmatrix} \text{ mm}$$

Total section strains: Global

Reinforcement:

$$\varepsilon_{s.final} := \varepsilon_N + \varepsilon_{s.M} - \varepsilon_{A1} = 0.00083$$

$$\varepsilon_{s'.final} := \varepsilon_N + \varepsilon_{s'.M} - \varepsilon_{A1} = 9.329 \cdot 10^{-4}$$

Section plot _____ Colorplot: Orange

$$\varepsilon_{s.final.normal} := \begin{bmatrix} 0 \\ \varepsilon_{s.final} \end{bmatrix}$$

$$\varepsilon_{s'.final.normal} := \begin{bmatrix} 0 \\ \varepsilon_{s'.final} \end{bmatrix} = \begin{bmatrix} 0 \\ 0.00093 \end{bmatrix}$$

$$h_{s.final} := \begin{bmatrix} d_0 \\ d_0 \end{bmatrix} = \begin{bmatrix} 100 \\ 100 \end{bmatrix} \text{ mm}$$

$$h_{s'.final} := \begin{bmatrix} h - d' \\ h - d' \end{bmatrix} = \begin{bmatrix} 1610 \\ 1610 \end{bmatrix} \text{ mm}$$

Concrete:

$$\varepsilon_{c.global} := \varepsilon_N + \varepsilon_{c.M} - \varepsilon_{A1} = 0.00094$$

$$\varepsilon_{NA.global} := \varepsilon_N - \varepsilon_{A1} = 0.00091$$

$$\varepsilon_{h_0.global} := \varepsilon_N + \varepsilon_{h_0.M} - \varepsilon_{A1} = 0.00082$$

Section Plot _____ Colorplot: Red

$$\varepsilon_{section.global.normal} := \begin{bmatrix} \varepsilon_{c.global} \\ \varepsilon_{h_0.global} \end{bmatrix}$$
$$h_{section.global} := \begin{bmatrix} h \\ 0 \text{ mm} \end{bmatrix} = \begin{bmatrix} 1.71 \cdot 10^3 \\ 0 \end{bmatrix} \text{ mm}$$

Bending strain external loads, withouth internal load effect

% To compare the internal load effect

Bending strain from only dead load moment M_g and ASR moment M_i

$$M_g + M_i = 4070 \text{ kN} \cdot \text{m} \qquad EI_{II} = (5.774 \cdot 10^{15}) \text{ N} \cdot \text{mm}^2$$

$$K_{g,i} := \frac{M_g + M_i}{EI_{II}} = 0.0000007 \frac{1}{\text{mm}}$$

$$\varepsilon_{c.Mg,i} := -K_{g,i} \cdot \alpha \cdot d = -0.00031$$

$$\varepsilon_{h_0.Mg,i} := K_{g,i} \cdot NA = 0.0009$$

Plot parameters Colorplot: Green

$$\varepsilon_{g,i} := \begin{bmatrix} \varepsilon_{c.Mg,i} \\ \varepsilon_{h_0.Mg,i} \end{bmatrix} = \begin{bmatrix} -0.00031 \\ 0.0009 \end{bmatrix}$$

$$h_{g,i} := \begin{bmatrix} h \\ 0 \end{bmatrix} \text{ mm}$$

Plot:

Normal: $M_{norm.ext} = M_g = 2141 \text{ kN}\cdot\text{m} + M_i = 1929 \text{ kN}\cdot\text{m}$

Red line: Total strain of section

Light blue line: Strain causing stress in concrete plate.

Purple line: Strain causing stress in non cracked part of beam

Orange lines: Reinforcement strains

External load plots, withouth inner load effect

Green line: $M_{ext} = M_g = 2141 \text{ kN}\cdot\text{m} + M_i = 1929 \text{ kN}\cdot\text{m}$

